Three Dimensional Flow Visualization of the Adverse Pressure Gradient Turbulent Boundary Layer

by

Michael Blake Melnick

A dissertation submitted to the Graduate Faculty of
Auburn University
in partial fulfillment of the
requirements for the Degree of
Doctor of Philosophy

Auburn, Alabama
May 10, 2015

Keywords: turbulence, fluid dynamics, boundary layer, adverse pressure gradient, coherent structures

Approved by

Brian Thurow, Chair, Associate Professor of Aerospace Engineering
Roy Hartfield, Professor Aerospace Engineering
Joe Majdalani, Department Head, Aerospace Engineering
Jay M. Khodadadi, Alumni Professor of Mechanical Engineering

Abstract

An adverse pressure gradient (APG) turbulent boundary layer is investigated using a three dimensional scanning flow visualization technique. This dissertation includes an introduction to the structures and past research of the zero pressure gradient (ZPG) and APG turbulent boundary layer, as well as a description of three experiments to investigate the turbulent boundary layer.

The first experiment of this work uses simultaneous 2-D particle image velocimetry (PIV) to complement 3-D flow visualization measurements in a turbulent boundary layer to compare the boundary layer edge. Building off of the first experiment, a separate experiment was performed to compare 2-D velocity with 2-D flow visualization. The edge of the boundary layer identified from flow visualization generally matches the edge determined from velocity and vorticity. The correlation between velocity deficit and smoke intensity indicated a moderate to strong relationship between the two. In many cases, velocity fields estimated from smoke intensity were similar to the actual velocity fields. While not suitable for estimating the velocity given an intensity field, the correlations validate the use of flow visualization techniques for determining the edge and large-scale shape of a turbulent boundary layer, specifically when quantitative velocity measurements are not possible.

The third experiment described in this dissertation consists of using a scanning 3-D flow visualization technique to compare the large scale features in a ZPG and APG boundary layer. In general, structures in a ZPG boundary layer are larger and spaced farther apart compared to the APG cases. Flow features identified through conditional averaging extend higher into the freestream flow for the APG cases and are more distinct and separated from the wall than in the ZPG case. The difference in the three cases is more pronounced with increasing wall-normal height.

Acknowledgments

I would like to thank my advisor, Dr. Brian Thurow, for his help and guidance in this research. I appreciate his valuable expertise in many different areas of aerospace engineering and his passion for helping his graduate students.

I would like to thank my colleagues in the Advanced Fluid Diagnostics Laboratory. From previous students such as Kyle Lynch, Harris Haynes, and Bryan Brock to current students Abhishek Bichal, Tim Fahringer, and Kyle Johnson, their help in running experiments, building ramps, and processing data was crucial for the completion of this dissertation.

I would like to thank my wife, Micah, for her love and support of my educational endeavors. Also, my son, Anderson, has provided fun-filled days and nights. Our baby, Maggie, is such a sweet gift of love. It is for my family that I worked so hard on my dissertation.

I would also like to thank my parents for their love and support of my education from kindergarten through graduate school.

Table of Contents

List of Figures

List of Tables

Chapter 1

Introduction

The investigation of three-dimensional coherent motions in a turbulent boundary layer is the focus of a considerable amount of research today. Although researchers have a general understanding of the structures contained in a turbulent boundary layer, the distinguishing characteristics of these motions and their complex 3-D interactions are not fully explained, particularly in an adverse pressure gradient (APG) flow. Understanding the nature of these motions in an APG turbulent boundary layer is important in many areas of fluid dynamics as researchers seek to better model, predict, and control wall bounded flows. Some cases of adverse pressure gradients include diffusers, the trailing edge of airfoils, and turbine blades. The efficiency of many of these devices is commonly determined by the adverse pressure gradient. In most real world flows, boundary layer separation is avoided due to large total pressure losses, loss of control, and loss of lift. The prediction of separation, however, can be extremely difficult and unreliable. Experimental investigation of the coherent structures in a turbulent boundary layer under an adverse pressure gradient could be beneficial for both practical and theoretical applications.

Flow visualization studies have been critical thus far in developing an accurate picture of the zero pressure gradient (ZPG) turbulent boundary layer structure, and more flow visualization studies of the large-scale and very-large-scale 3-D motions could provide further insight into these structures. However, the qualitative and sometimes ambiguous nature of the flow visualization of a seeded boundary layer is a limiting factor in many experiments. The ability of flow visualization studies to accurately extract information from the flow could be further investigated.

The focus of this dissertation is examining the 3-D size and shape of large scale motions in the APG turbulent boundary layer compared to the ZPG turbulent boundary layer. Three separate experiments were performed to determine the ability of the flow visualization technique to identify features of the flow and to compare the ZPG turbulent boundary layer with the APG turbulent boundary layer.

Chapter 2 of this dissertation provides a background of relevant literature which led to the picture today about the structures in the ZPG and APG turbulent boundary layer. Also, the evolution of measurement techniques from flow visualization to 2-D and 3-D quantitative measurements is discussed. Chapter 3 examines the experimental and mathematical tools used to investigate the turbulent boundary layer structures such as proper orthogonal decomposition (POD), linear stochastic estimation (LSE), fast Fourier transforms (FFT), and conditional averaging.

Chapter 4 details an experiment complementing 3-D flow visualization with a simultaneous 2-D velocity measurement in a ZPG turbulent boundary layer. This is a first attempt at enhancing a scanning flow visualization technique with more quantitative measurements. The ability of the flow visualization to accurately identify large scale features in the boundary layer is demonstrated in this experiment. The simultaneous experiment in Chapter 4 led to two separate experiments reported in Chapter 5 and 6.

Chapter 5 describes a 2-D experimental trial performed to further delve into the relationship between flow visualization and velocity in the turbulent boundary layer. This experiment uses the same 2-D images for both flow visualization (image intensity) and particle image velocimetry (PIV) to explore the ability of flow visualization to accurately highlight the boundary layer edge and the large scale motions in the flow.

Chapter 6 details a 3-D flow visualization trial of a zero pressure gradient turbulent boundary layer and two different adverse pressure gradient boundary layers. Visual observation, power spectral densities, and conditional averaging are used to compare and contrast the size, shape, and characteristics of the 3-D large scale features of the ZPG turbulent

boundary layer with those in the APG turbulent boundary layer. Chapter 7 concludes the dissertation with a summary and discussion of the relevant contributions of this work to the field of fluid dynamics.

Chapter 2

Background

2.1 Turbulent Boundary Layers

Since turbulent flow was first noticed in a pipe and detailed by Osborne Reynolds in 1883, the problem of turbulence has been a source of much investigation in the field of fluid dynamics [1]. Its three dimensionality and complex spectrum of structures have kept many aspects of the turbulent boundary layer unclear to this day. In the 1950's and 1960's researchers began realizing that the motions in the turbulent boundary layer were not random fluctuations of the mean flow. The flow consisted of irregular but repetitive patterns. One such pattern was the discovery of low speed streaks by Kline et al. in 1967. Using a flow visualization technique, they found organized motion within the laminar sublayer of the turbulent boundary layer. These motions led to low speed streaks in the near wall region of the flow. These low speed streaks were spaced 100 wall units in the spanwise direction (for a wide range of Reynolds numbers) and about 600 to 1000 wall units in the streamwise direction [2]. Further away from the wall, the low speed streaks are not present, but replacing them are complex structures with scale increasing with increasing distance from the wall.

Early on, researchers were discovering that fluid from the sublayer could be transported to the outer layer and many times very rapidly [3]. These ejections would create intense velocity fluctuations in the outer region. This interaction between inner and outer layers of the boundary layer has become a very important aspect of investigation in the structures in the flow. Abrupt eruptions near a low-speed streak are referred to as the bursting process [2]. The near wall fluid erupts well into the outer layer of the flow. Following this ejection, high-speed fluid "sweeps" into the wall layer. A passing vortex causes a pressure fluctuation which causes the bursting event. The bursting process is an interaction between the wall

layer and outer layer during only a time period brief compared to the quiescent period, but it generates a majority of the Reynolds stress [4, 5]. These interactions are a key component in the formation and preservation of turbulence.

Beyond the outer region of the turbulent boundary layer, the flow does not gradually blend into the freestream, instead, Corrsin and Kistler showed a sharp and distinct boundary layer edge which separated the rotational flow from the irrotational freestream [6]. This irregular boundary layer edge explained the intermittency in the hot-wire measurements of velocity fluctuations in the boundary layer that was not in the freestream flow. Corrsin found very similar results of a distinct boundary layer edge in a round jet, a plane wake, and a turbulent boundary layer. Fiedler and Head used smoke injected flow visualization to show the boundary layer edge in the turbulent flow [7]. This boundary layer edge outlined turbulent bulges. Kovasznay et al. used conditionally averaged hot-wire measurements in a wind tunnel to calculate that these bulges were about 1.5 to 2 boundary layer thicknesses (δ) in the streamwise and 1δ to 1.5δ in the spanwise dimensions [8]. These bulges act as obstacles to the freestream flow creating entrainment. Townsend was the first to recognize the importance of these large-scale motions to the total energy of the flow [9]. Turbulent bulges have very steep leading fronts and more gradual sloped backs. The downstream back of a bulge is separated by the front of an adjacent bulge by a sharp crevice in the potential flow [10]. It was not until later that the structures which lie inside the turbulent bulge would be defined, and even today some of those are unknown.

Another major discovery of the turbulent boundary layer is the idea of a horseshoe type vortex first proposed by Theodorsen as the building block of turbulence [11]. Townsend similarly proposed "tilted vortices" near the wall being the dominant structures in the turbulent boundary layer [12]. In retrospect, it can be shown that the feet of Theodorsens horseshoe vortices were possibly the structure Townsend was detailing in the wall region. Through flow visualization, Head and Bandyopadhyay provided the first notable experimental evidence of

these hairpin vortices [13]. The simple hairpin vortex is rarely symmetric, but is often a fragment of the horseshoe or one legged [14]. The complex dynamics of these three-dimensional vortices in a high shear mean flow complicate the turbulent flow field.

As hairpin vortices grow further away from the wall (into regions of decreased shear), the local vorticity diminishes, the hairpins expand in the spanwise dimension and become larger. By using simultaneous hot-wire and flow visualization of a turbulent boundary layer in a wind tunnel, Falco showed that in low Reynolds number flows, the turbulent bulges are composed of these smaller-scale vortical structures. The turbulent bulges can span the entire boundary layer thickness. Falco gives a model of the flow in the outer region of the turbulent boundary layer which incorporates the large scale motions, their eddies, and their interactions [15]. Perry, Henbest, and Chong give a very good conceptual model of this hierarchy of vortices [16] following the lead of Townsend's attached eddy hypothesis [17]. The attached eddy hypothesis assumed that the turbulent boundary layer consisted of similarly shaped eddies at a range of length scales proportional to their distance away from the wall. The model was refined to include different types of eddies (Types A, B and C) and detached eddies as well - which only contribute minor modifications to the Reynolds stress.

Much of the past research on a turbulent boundary layer has looked at some near wall features such as low-speed streaks in the sublayer. The near wall region and its turbulence production have been the source of investigation due to its high shear and more controlled environment compared to the outer region. However, more recently, effort has been devoted to looking at the structures in the outer region of the turbulent boundary layer - in particular studying the role of hairpin vortex packets. Less is known about the structure of the outer layer as opposed to the buffer layer because it has a wider range of scales making observation more difficult and because it is a region of larger Reynolds number making direct numerical simulation more difficult [18]. It has also been shown that larger scale structures emerge more prominently in the outer region of the turbulent boundary layer in flows with higher Reynolds number and in adverse pressure gradient flows [19]. In addition, it has been shown

that the large scale motions in the outer region do impact the near wall flow [20]. The lack of the research in previous literature leads to the need in a more thorough investigation of the flow structures in the outer region.

The organization and interaction of these hairpin vortices has been a much debated aspect of the turbulent boundary layer. Some have argued that the hairpins are randomly spaced throughout the boundary layer with no organization [13, 21]. Smith et al. proposed a mechanism for a primary hairpin vortex to generate new hairpin vortices in-line in the streamwise direction both upstream and downstream [5]. Some of the work by Adrian has shown hairpin vortices in the logarithmic layer and in the wake region of turbulent boundary layers. They have shown that aligned hairpins in the flow create regions of low momentum [18]. These aligned vortices create hairpin vortex packets in the flow. These low-speed structures and hairpin vortex packets have been shown to create a majority of the Reynolds stress in the outer layer [22]. In fact, Marusic [23], in 2001, calculated that the hairpin vortex packet model generated more accurate turbulence statistics than the random hairpin model by Perry, Henbest, and Chong in 1986 [16] compared to experimental Reynolds stress measurements.

The streamline spacing between the aligned primary and secondary vortices is governed by small scales but the distance between two primary vortices is governed by large scales. The streamwise vortex spacing in a packet relates to the frequency of strong ejection (Q2) events. It is known that multiple Q2 events can occur within a single burst event as shown by Bogard and Tiederman [24]. A burst event is associated with the passage of a hairpin head in a packet as shown by Adrian et al [25]. Therefore, if the spacing of the hairpin vortices increases, the frequency of Q2 events will decrease.

The average widths of large-scale structures, such as low momentum regions, are closely associated with the size of the hairpin vortices in the outer layer. Adrian's work on a turbulent boundary layer in a wind tunnel [25] used conditionally averaged particle image velocimetry fields to show that that hairpin vortices are the structures associated with the

production of turbulence in the outer layer. Hairpin vortices occurred in streaks and were aligned in packets that flow with small dispersion and grow at an inclination angle increasing with distance away from the wall. The mean angle of the alignment of vortices is 12° from streamwise. These packets are typically spaced several hundred viscous length scales apart in the streamwise direction. They showed that with increasing Reynolds number the number of hairpins in a packet increases as well [25].

Recently, it has been shown that turbulent bulges may be linked by very large-scale motions. The very large-scale motions can be on the order of 5 to 10 boundary layer thicknesses in the streamwise direction or larger. They result from the coherent alignment of large-scale motions in turbulent bulges or packets of hairpin vortices. One turbulent bulge can be associated with one hairpin packet, but more commonly, a bulge can consist of several packets at various stages of growth. According to Tomkins [26], the very large scale motions are a consequence of the spatial coherence between bulges or between hairpin packets. The low momentum flow in the lower part of each packet aligns with the flows in other packets to form a much larger structure. Thus very large-scale motions are not a new type of eddy; they are simply the coherence of smaller structures. The very large-scale motions are longest in the lower half of the boundary layer. The long streamwise dimensions of the motions are a consequence of bulges aligning coherently so that low momentum flow from the lower half of one bulge is passed onto the next and so forth over a span of many bulges. According to Kim and Adrian, a consequence of this alignment is that numerical simulations of wall turbulence may need to be altered to account for these very large-scale motions [10]. Measurements have indicated that these "super structures" account for a significant percentage of the turbulent kinetic energy and Reynolds shear stress, and they appear to modulate the amplitudes of the smaller scale motions in the near wall region of the flow [23]. This highlights the importance of more investigation into these structures and their dynamics. When these super structures do not align perfectly in the streamwise direction, (which is often the case), the very large scale motions will meander in the spanwise direction [27]. This

can complicate the observations from two-dimensional measurements and highlight the need for more three-dimensional measurement techniques. Marusic et al. provides an excellent review of turbulent boundary layer structures including these very large scale motions [28].

Researchers have shown little information about the global spanwise arrangement of large scale coherent structures or hairpin vortex packets. Delo and Smits, investigating a low Reynolds number (Re_θ=701), ZPG turbulent boundary layer, observed a relatively small number of structures, but the structures varied greatly in size and shape and were felt to be representative of turbulent boundary layers in general. They clearly saw large-scale structures in the x-z (streamwise-spanwise) plane aligned along diagonals +/- 50 degrees from streamwise [20]. The spacing along the lines varied, but was approximately 1δ in the outer portion of the boundary layer. This spanwise orientation had not been documented extensively prior to their experiment. They also found that ejections appeared to be spatially organized and linked to the passage of the large scale motions. Elsinga et al. used tomographic-PIV and found large scale hairpins with a length of 0.4δ in the spanwise dimension that were spaced 1.5δ in the streamwise direction in the ZPG turbulent boundary layer [29]. Looking in the outer region of the boundary layer, (in their case, y = $.15\delta$ to $.89\delta$), the hairpins had a preferential alignment in the spanwise direction of 45 degrees from streamwise. They commented that this is an indication of the spanwise-streamwise orientation of coherent structures in the turbulent boundary layer. They also found regions of low speed motion over 3.5δ in the streamwise direction similar to very large scale motions [29].

2.1.1 Adverse Pressure Gradient

One of the most important areas of boundary layer research is that of a turbulent boundary layer on the verge of separation. Numerous real world applications can suffer from the effects of a separating boundary layer including helicopter blades, turbines, ships, and aircraft. A great amount of research has focused on zero pressure gradient turbulent boundary layer flows, but the investigation of APG flows is very limited, due to its complexity.

Turbulent boundary layers with an APG have been considered to be some of the most difficult flows to predict using turbulent models [30].

Some features of the coherent motions in the APG turbulent boundary layer are generally accepted. Previous researchers have noted that the large scale motions in the APG turbulent boundary layer were larger and erupted more violently than the structures in the ZPG boundary layer [31, 32]. In an adverse pressure gradient, the velocity profile develops a larger wake region and the turbulent kinetic energy decreases in the near wall region [33]. Nagano also researched the slight differences in the instantaneous velocity signals and distribution of turbulence intensities in ZPG and APG flows. The frequency of Q2 events (ejections) is reduced and Q4 events (sweeps) last longer in the adverse pressure gradient flow [34]. The coherent motions in the outer region of the APG flow are altered due to the increase in the contributions of the sweep motions [35]. Krogstad and Skare showed that there is an outer peak in the Reynolds shear stress in the outer layer due to an adverse pressure gradient. They also showed an outer peak in the production of turbulent kinetic energy due to this peak in Reynolds shear stress. There is a reduction in the anisotrophy in the near wall region due to the reflection of the turbulent motion back to the outer layer.

Tulapurkara et al. measured increased turbulent kinetic energy for an APG turbulent boundary compared to that of a ZPG turbulent boundary layer over a flat plate [36]. Alving and Fernholz described the increase in the mean shear away from the wall and decrease in the shear near the wall region in the APG flow compared to the ZPG flow. They also noted that the peak in Reynolds stress moved further from the wall, to roughly half of the boundary layer height [37].

Clauser was the first to define an equilibrium boundary layer parameter to analyze and compare pressure gradient flows [38]. His pressure gradient parameter is defined as:

$$\beta = \left(\frac{\delta*}{\tau_w}\right)\left(\frac{dP_\infty}{dx}\right) \tag{2.1}$$

The wall shear stress is defined as τ, and the displacement thickness is δ. If β is a constant value the boundary layer is said to be in equilibrium under the pressure gradient. Bradshaw found that with increasing pressure gradient and increasing β, the maximum shear stress increases [39].

While there is some information about the mean flow and turbulent statistics, less is known about the coherent structures in the adverse pressure gradient turbulent boundary layer. Krogstad and Skare found by using two point velocity correlations that the correlation length in the streamwise direction of the streamlines velocity decreases under a strong adverse pressure gradient. They found that the inclination angles of the correlations did not change under the adverse pressure gradient [40]. However, Lee and Sung found that the inclination angle of the heads of the hairpins for the adverse pressure gradient was 18^{o} compared to 13^{o} for the zero pressure gradient turbulent boundary layer [41].

Marusic and Perry [42] applied the attached eddy hypothesis to adverse pressure gradient flows and made the assumption that each eddy is not dependent on the pressure gradient. However they failed to reproduce the turbulence statistics of the adverse pressure gradient turbulent boundary layer and concluded that the impact of the average pressure gradient on the individual eddies must be taken into account.

Another discrepancy in the knowledge of APG flows is related to the spanwise spacing of near wall streaks in the APG turbulent boundary layer. Finnicum and Hanratty found that streak spacing in the near wall region is not affected by the pressure gradient [43], but Lee and Sung found that the streamwise spacing of the near wall streaks increases from 100 viscous wall units in the zero pressure gradient case to up to 400 viscous wall units in the adverse pressure gradient case [41]. This emphasizes the fact that there is a need for more experimental research into the adverse pressure gradient turbulent boundary layer-specifically, a very strong APG or one on the verge of separation.

The separation of the turbulent boundary layer is a difficult process to predict, and can be vague due to its inconsistencies. For example, a separating boundary layer rarely occurs

at one location, rather, there is a separating region of the flow. Simpson describes the flow as incipient detachment (ID) when the flow is reversed 1% of the time, intermittent transitory detachment (ITD) when the flow is reversed 20% of the time, and transitory detachment when the flow is reversed 50% of the time [44]. Fully detached flow occurs when the wall shear stress is zero. The locations of incipient detachment, intermittent transitory detachment, transitory detachment, and fully detached flow will vary and shift for many relevant flows.

2.2 Flow Visualization Studies

Flow visualization studies, such as seeding smoke into the boundary layer, have served an important role in determining details of the underlying structure of a turbulent boundary layer. The flow visualization trials of Praturi and Brodkey [45] in 1978, and Head and Bandyopadhyay [13] in 1981, to more recent flow visualization trials of Smits and Delo [46] in 2002, among others, have led to very important discoveries of the structures in a turbulent boundary layer. In fact, much of the current understanding of the turbulent boundary layer has flow visualization experiments at its roots which will often lead to more detailed investigation. For example, inspired by the smoke visualization of a turbulent boundary layer by Head and Bandyopadhyay which depicted hairpin vortices inclined at 45 degrees from horizontal, Hutchins et al. performed cross-plane stereo-PIV inclined at 45 degrees to successfully detect these hairpins vortices [47].

There are benefits and drawbacks to using flow visualization for research in turbulent flows. Traditional flow visualization techniques are limited due to uncertainties, specifically in the seeding process. Goldstein and Smits argue that since the smoke is transported by turbulence, the smoke will mark the edge between the vortical boundary layer and the non-turbulent free stream flow [40]. Previous works have qualitatively supported this assumption [48], but quantitative support of this assumption is lacking. Hussain said that "flow visualization presents excessive information but very little hard data, and anemometers give some hard data but very limited flow physics [49]." Head and Bandyopadhyay noted that the

transfer of vorticity on a molecular scale takes place faster than the transfer of fluid, so there may be a small region beyond the smoke filled area which contains vorticity [13]. They say that smoke gives a "very fair" indication of the concentrations of vorticity, but smoke should not automatically imply vorticity because vortices of opposite signs may coalesce and cancel out in a particular region. This presents the possibility that "history of turbulence" effects can decouple the relationship between the smoke and the turbulent motions that it is marking such that observations based on seeding the boundary layer can potentially be misleading.

The potential ambiguity of flow visualization studies has led some researchers to supplement flow visualization data with more quantitative measurements. For example, Falco investigated the turbulent boundary flow on the bottom of a wind tunnel wall seeded with oil fog to fill the turbulent boundary layer. They also used simultaneous hot wire measurements to investigate the typical eddies and large scale motions in the flow [15]. Talmon et al. used hydrogen bubbles to visualize the flow in a water tunnel and complemented that with simultaneous Laser Doppler anemometry to detect the bursts in the wall region of a turbulent boundary layer flow [50]. More investigation is necessary to determine the capabilities of the scanning flow visualization technique in experimentally investigating the turbulent boundary layer.

Westerweel used combined planar laser induced fluoresence and particle image velocimetry to investigate the ability for a passive scalar (such as smoke or dye) to mark the boundary edge [51]. For a free turbulent jet, they measured finite Reynolds stresses at the turbulent - non-turbulent interface indicating levels of velocity fluctuations outside the region marked by the passive scalar. Bisset et al. found similar results from the direct numerical simulation of a turbulent wake behind a parallel plate [52]. The objective detection of the edge of the turbulent - non-turbulent interface has been an intriguing aspect of the turbulent boundary layer research, and most relevant to the work described in this dissertation is the technique described by Prasad and Sreenivasan [53]. For a turbulent boundary layer seeded by smoke

or dye, the boundary layer edge can be detected by calculating the inflection point of the plot of the average (dye or smoke) intensity of pixels above a set threshold. This method works well for an objective way to find the boundary layer edge in flow visualization experiments.

With more confidence that the smoke intensity accurately marks the features in the boundary layer, flow visualization techniques can be used for experimental investigation when more precise, quantitative measurements are not possible. One instance where quantitative measurements are prohibitive is 3-D flow visualization using a high speed scanning technique, as is described in this work. PIV measurements require high resolution image pairs for detection of particles in the flow for displacement correlation to calculate a velocity field. In contrast, many flow visualization techniques can be performed with lower resolution images and without the need for double pulsing the camera or laser, making it sometimes more accessible for a range of fluid dynamics experiments. Overall, flow visualization techniques may give up quantitative information for benefits in looking at larger fields of view, easier set-up/calibration, and sometimes less expensive equipment.

Flow visualization research has been crucial in developing the picture we have today of the turbulent boundary layer. The three important 3-D flow visualization studies of Goldstein and Smits [40] in 1994, Delo and Smits [20] in 1997, and Delo, Kelso, and Smits [54] in 2004 have been beneficial in giving insight to the coherent structures of the zero pressure gradient turbulent boundary layer. Goldstein and Smits, in 1997, performed a 3-D flow visualization of a turbulent boundary layer in the Princeton Gas Dynamics Laboratory subsonic wind tunnel facility. In this experiment, the boundary layer flow was tripped turbulent, and injected with smoke to seed the boundary layer. An upstream injection location seeded the full boundary layer, and a downstream injection location seeded the structures near the wall close to the measurement location. A laser sheet and scanning mirror enabled 2-D images to be captured across the volume at a rate much higher than the convection velocities of the fluid, allowing for a quasi-instantaneous 3-D snapshot of the flow. They imaged 96 volumes of the flow (every 0.2 seconds of a 1.92 second duration).

The volumes each measured 58mm (0.42δ) in the streamwise direction, 37mm (0.30δ) in the wall-normal direction, and 82mm (0.59δ) in the spanwise direction. In the limited number of sequences analyzed, they saw horseshoe vortex parts, such as legs and tails. In one instance, they saw a nearly-intact horseshoe vortex rising from the wall. Using visualization and correlation techniques, they found low-speed streaks between 10 to 80 wall units in length, with a spanwise separation of between 60 to 130 wall units. They found ejections no wider than 10 wall units with a streamwise length of over 80 wall units. The coherent structures in the log-layer were between 100 to 200 wall units in the spanwise direction and over 100 wall units in the streamwise direction. The convection velocities of the small and large scale coherent structures were measured to be approximately 50% of the local mean velocity. Correlations showed the ejections usually occurred roughly 90 to 140 wall units after a log-layer coherent structure passed, not direction beneath one.

The 1997 study of Delo and Smits uses a rotating drum to scan 2-D laser sheets across the flow to form a nearly instantaneous 3-D flow visualization volume using two dye injection locations to visualize fluid motions in the inner and outer portion of the zero pressure gradient turbulent bounday layer. Their study of the low-speed flow in a water tunnel (Reynolds number based on momentum thickness of 701) showed evidence of structures aligned at 50 degrees from the streamwise direction. In looking at 1600 consecutive volumes, each composed of 20 images, they saw a variety of large scale structures with an average spacing along the 50 degree diagonals of 1δ. They caution the reader of the importance of three-dimensional measurements, and explain that looking at the same data in 2-D can make the appearance of a more complex picture of the boundary layer than in reality. The two dimensional slices may cut a single structure into may pieces and the resulting picture will overestimate the variety of structures in the flow.

Delo et al. present a more in-depth look at the 3-D flow visualization volumes of the flow on the flat plate in the water tunnel facility [54]. They investigate the flow visualization volumes pointing out examples of possible horseshoe vortices, mushroom cross-sections, large

scale motions, streamwise and spanwise alignments, and a variety of large-scale coherent structures. They demonstrate that 2-D cross sections of the 3-D flow compare well with previous 2-D measurements of turbulent boundary layers. They reiterate the alignment of large scale structures at 50 degrees from the streamwise direction approximately spaced by 1δ. They show agglomerations of large scale motions measuring upwards of 5δ in length, though, if viewed in 2-D, these structures would have seemed smaller. They suggest that a phenomena other than simple vortex merging is occurring, creating the large-scale diagonal organization of the structures. The ejections of near-wall fluid appeared to be spatially organized and associated with the motion of the large scale agglomerations in the outer region of the flow. One last observation from the 3-D flow visualization was the strong ejections of the near-wall fluid into the outer portion ($>0.7\delta$) of the boundary layer over a very short streamwise distance, indicating that the outer layer structures are not passive artifacts of upstream motions.

In comparison with these previous 3-D flow visualization studies, the cameras used for experiments described in this dissertation are capable of producing higher resolution images, and can be operated at a higher frame rate. In addition, this flow visualization technique can investigate a larger volume. But more importantly, this trial investigates the 3-D turbulent boundary layer under an adverse pressure gradient. There is little to no information about the 3-D shape, orientation and organization of large scale motions in an adverse pressure gradient turbulent boundary layer.

2.3 3-D Measurement Techniques

There are inherent problems with using 2-D measurements to investigate highly three-dimensional turbulent boundary layer structures. Naturally, the size, spacing, and orientation of structures in the third dimension are missing. Perhaps more importantly, the size and spacing of structures in the dimensions being investigated may also be inaccurate. An image that does not incorporate the spanwise dimension can present a more complex picture

of the flow than actually exists. Smits and Delo showed that sampling the image in 2-D can distort one structure with a spanwise offset into several pieces which could appear not to be connected. This will overestimate the variety of structures present in the flow and can neglect important interactions in the spanwise direction [46].

Dennis and Nickels used Taylor's frozen flow hypothesis in conjunction with time-resolved, stereoscopic PIV to acquire velocity measurements in a quasi-instantaneous three dimensional spatial field [55, 56]. Taylor's hypothesis, which assumes structures' shapes are not appreciably changed across the projected distance, can be applied for some flows, but can potentially fail for larger fields of view. Dennis and Nickels found that Taylor's hypothesis can be applied for distances up to 6δ in a turbulent boundary layer. Using 3-D correlations and conditional averaging, they found strong evidence of hairpin vortex packets. Their paper details the capabilities of their quasi-instantaneous 3-D technique for large structures [56] in a ZPG boundary layer but does not address APG turbulent boundary layers. In looking at a moderate Reynolds number (Re = 4700) flow in a water tunnel, they found evidence for symmetric hairpin vortices grouped in packets from the ensemble average of conditional events. However, they did not find such evidence in instantaneous events - only on average.

There are many 3-D velocity measurement techniques that have emerged in the last decade. Holographic and tomographic PIV, to name a few, have been valuable in giving insights into 3-D structures in the turbulent boundary layer. A recent review of a few of these three-dimensional, three-component (3D-3C) techniques such as holographic PIV, scanning PIV, 3-D particle tracking, and tomographic PIV is given by works such as Elsinga and Ganapathisubramani and Westerweel et al. [57, 58]. The field of view for most 3-D PIV measurements (aside from plenoptic PIV) is limited due to the need to image small particles and associated limitations in laser energy, camera resolution and other factors. However, flow visualization - scalar intensity images that result when relatively dense smoke is introduced into the boundary layer - can be performed at a lower resolution and without the need for the double pulsing of a laser, providing for a greater flexibility in the experimental setup thus

allowing larger fields of view than generally possible with other techniques. These 3-D, 3-C techniques are improving rapidly and some researchers have used them to investigate much larger volumes such as the work of Brucker et al. in using a 3-D scanning PIV technique [59].

2.4 Knowledge Gaps

In a review of the relevant literature there are a few areas of fluid dynamics and flow visualization techniques which need further investigation. First, the ability of the flow visualization of a seeded turbulent boundary layer to identify the large scale features at the boundary layer edge needs more research. The connection between the flow visualization measurements and velocity or vorticity measurements has not been shown previously for a turbulent boundary layer. Using a correlation to estimate a velocity field from a flow visualization image has not been detailed in literature previously.

Research in the adverse pressure gradient is lacking. Specifically, a description of the large scale motions in an adverse pressure gradient compared to the zero pressure gradient is not found in the literature review. A few researchers have shown a preferential alignment of 45 or 50 degrees from streamwise for the large scale motions in a ZPG turbulent boundary layer, but a description of the alignment in an APG turbulent boundary layer is missing.

With more confidence that the smoke intensity accurately marks the features in the boundary layer, flow visualization techniques still have the potential to be used for experimental investigations where more precise, quantitative measurements are not possible. In this work, the long-term objective is to study the 3-D structure and organization of large-scale structures in turbulent boundary layers under varying adverse pressure gradient conditions. Due to the physical dimensions of the boundary layer in the subsonic wind tunnel (boundary layer thickness order of 50 mm) and desire to study the very large scale motions in three

dimensions, PIV is not presently a viable technique for the current application. Rather, classical 3-D flow visualization techniques could be beneficial in the detection and investigation of these structures.

Chapter 3

Data Analysis Methods

3.1 Introduction

This chapter presents a discussion of relevant mathematical techniques used in the experiments described in this paper. The proper orthogonal decomposition (POD), linear stochastic estimation (LSE), power spectral density, and conditional averaging are used to investigate the turbulent boundary layer in the experiments described in chapters 4, 5, and 6.

3.2 Proper Orthogonal Decomposition

The proper orthogonal decomposition extracts a basis for modal decomposition from a group of signals. POD was first introduced in terms of turbulence in 1967 by Lumley, providing a way to extract coherent structures from the flow [60]. POD is also useful in low-dimensional modeling, using only the most basic modes to describe the flow. Lumley proposed the POD to identify large scale structures in the turbulent flow and suggested that the lowest order mode represented the large-scale structure. In 1977, Sirovich developed the method of snapshots which uses a correlation of instantaneous velocity fields of the flow. This method, which is used in the present experiment, reduces the order of the eigenvalue problem to the number of the snapshots, instead of the number of data points [61].

The modes are derived by first correlating the fluctuations of all images to get a covariance matrix, C.

$$C = \begin{bmatrix} u_1 \cdot u_1 & \cdots & u_1 \cdot u_n \\ \vdots & \ddots & \vdots \\ u_n \cdot u_1 & \cdots & u_n \cdot u_n \end{bmatrix} \tag{3.1}$$

Here, u' is the fluctuating velocity (or fluctuating smoke intensity, i', for flow visualization), and n is the number of images in the dataset. The eigenvectors, α, and eigenvalues, λ, of the covariance matrix are calculated, and it can be mathematically proven that the largest eigenvalues correspond to the modes with the highest levels of turbulent kinetic energy (u'^2) or intensity variance (i'^2).

The first mode, Y_1, is calculated by summing the product of the eigenvector with the largest corresponding eigenvalue and the fluctuating velocity fields, u.

$$Y_m = \sum_{t=1}^{n} \alpha_{im} u_i \tag{3.2}$$

All subsequent modes are calculated similarly using the next largest eigenvalue. The energy, or the relative importance, or frequency of each mode is related to the magnitude of the eigenvalue.

3.3 Linear Stochastic Estimation

Linear stochastic estimation is the approximation of a random variable in terms of some other, known, variable(s). Estimating the velocity field given surface pressure measurements has been widely used application of LSE. The estimate of u given a known event variable, E, is

$$\hat{u}_i = linear\ estimate\ of\ \langle u_i | E \rangle = \sum_{j=1}^{M} L_{ij} E_j \tag{3.3}$$

where M is the chosen number of events and L is the estimation coefficients. The estimation coefficients are chosen such that the mean square error is a minimum, and the orthogonality principle states that the difference, $\langle u_i|E\rangle - \sum_j L_{ij}E_j$, is statistically orthogonal to the data, therefore,

$$\langle \big[\langle \hat{u}_i|E\rangle - \sum_j L_{ij}E_j\big] E_k\rangle = 0 \tag{3.4}$$

Manipulating this equation leads to the Yule-Walker equations, which is an M x M system of linear algebraic equations.

$$\sum_{j=1}^{M}\langle E_j E_{jk}\rangle L_{ij} = \langle E_k \hat{u}_i\rangle, \qquad j,k = 1,,M. \tag{3.5}$$

The estimation coefficients L_{ij} are simply the correlation coefficients between event data (E) and the quantity being estimated, u_i'.

3.4 Power Spectral Density

To objectively evaluate the size of a structure, the power spectral density (PSD) can be calculated. Using the Fast Fourier Transform, images can be converted from the spatial domain to the frequency domain. Mathematically, a 2D M x N image can be converted to a frequency image by

$$F(a,b) = \sum_{x=0}^{M-1}\sum_{z=0}^{N-1} f(x,z)e^{-i2\pi\left(\frac{ax}{M}+\frac{bz}{N}\right)} \tag{3.6}$$

In Equation 3.6, the spatial domain is defined in f(x,y) and the frequency domain is F(a,b). The basis function is the exponential term. The frequency domain is composed of sine and cosine waves with increasing frequency. For example, F(0,0) is the constant, average value of the image. As a and b increase, the frequency increases, corresponding to smaller wavelengths. The values at each frequency relate to the relative importance of the structures

with that frequency. The values of the Fourier domain can be summed across either direction (here, the z (spanwise) direction or the x (streamwise) direction) to get a measure of the structures with a certain wavelength in the streamwise (or spanwise) directoin, independent of its wavelength in the other direction.

In turbulence, the most common use of power spectral density is that of investigating the PSD of the velocity fluctuations in a turbulent region. The information in the PSD allows for the objective classification of the different scales or sizes of features in the flow. Typically, the normalized spectral density is plotted as a function of the wavenumber (or frequency). The decrease in the energy of the structures in the flow from the velocity fluctuation as frequency increases (structure size decreases) is well known and is approximately on the order of a line of wavenumber, κ, to the -5/3 power. In this paper, though, the power spectrum of the velocity fluctuations are not being investigated, rather, it is the power spectrum of the intensity of the images, which can still be used to determine the size of structures in the flow visualization data.

3.5 Conditional Averaging

Conditional sampling has been used as an experimental technique to investigate and isolate certain regions of the flow which exhibit the same characteristic behavior. Conditional averaging can be used in flow visualization to extract quantitative information from customarily qualitative data. Vortex structures embedded in turbulence can be seen in flow visualization data and conditional averaging has proven helpful in targeting just their occurrences in the flow field. The turbulent-non turbulent interface has also been the subject of many conditional averaging investigations. In addition, periodic or quasi-periodic flows have been the subject of many conditional averaging analysis [62].

Conditional averaging isolates occurrences which meet certain criteria and takes the average of the flow surrounding them. The function which defines whether the averaging will or will not occur is the most important aspect of the conditional averaging process. The

threshold of the function also is a major consideration, as different thresholds have shown to produce drastically different results from the same flow data [62].

In this paper, for example, for a two dimensional streamwise-spanwise slice of the turbulent boundary layer, instances in which there is an "island" of the turbulent boundary layer (seeded with smoke) surrounded by the freestream flow (unseeded), a detection scheme in MATLAB will tag the center of that "island" or structure. Each of these structures that lie in a certain region of the image and whose area lies in a certain range will be selected to include in the conditional average. The center of each the structures can then be shifted to be the new center of the image, and the volume around that structure can be averaged to learn more about the flow around each structure. The average of these volumes can then be investigated and compared to uncover the differences in the structures which are due to the different conditions (i.e. pressure gradient) of the flow.

Chapter 4

Simultaneous 3-D Flow Visualization with 2-D PIV to Observe a Turbulent Boundary Layer

4.1 Introduction

Many areas of fluid dynamics stand to benefit from an improved understanding of the structures of a turbulent boundary layer. While traditional flow visualization techniques, such as the seeding of smoke into the boundary layer, have provided a wealth of information, they have ultimately been limited due to the uncertainty associated with the smoke seeding process. In recognition of the very three-dimensional nature of turbulent flows, a 3-D flow visualization technique has been developed by scanning a high repetition rate laser sheet that is robust and can be applied to high Reynolds number boundary layers. In comparison to other recent developments in 3-D imaging (e.g. tomographic PIV, holographic PIV), the current technique is not sensitive to particle seeding conditions and can be applied to larger flow volumes. Preliminary results illustrate the power of this technique to visualize 3-D flow structures in a unique fashion. As such; in future chapters this technique will be used to explore the 3-D characteristics of turbulent boundary layers under an adverse pressure gradient. The scanning technique, in its current form, is limited to qualitative flow visualization and is thus plagued by the same concerns that plagued earlier flow visualization works. Therefore, before moving forward, it is important to explore the relationship between the current 3-D visualizations and more developed techniques, such as PIV.

The work presented in this chapter uses simultaneous 3-D flow visualization with 2-D PIV to investigate a turbulent boundary layer. Using a 3-D scanning technique, 3-D images with 220 x 148 x 43 pixel resolution with a total scan time of 136 microseconds are recorded, enabling the reconstruction of nearly instantaneous 3-D views of turbulent

boundary layers. Simultaneously, 2-D PIV is captured in the middle of the volume to better investigate the flow. By comparing the 3-D flow visualization with the 2-D PIV at the same instant and at the same point in the flow, the 3-D structures being observed are able to be further investigated. Proper orthogonal decomposition is used to calculate the modes (building blocks) of the flow visualization and velocity fields. Using the correlation between the modes, the relationship between smoke intensity and velocity is explored.

4.2 Experimental Arrangement

The Advanced Flow Diagnostics Laboratory at Auburn University has developed a new 3-D imaging technique on a turbulent boundary layer. Before implementing this imaging to an adverse pressure gradient or separating flow, in this chapter the technique is applied to a simple turbulent boundary layer to make observations and assess the capabilities of the flow visualization method.

4.2.1 Facility and Particle Seeding

All experiments described in this work were conducted in the Auburn University subsonic wind tunnel. Experiments in this chapter focused on visualizing the boundary layer formed on the bottom wall of the wind tunnel. The flow on the wall was tripped to a turbulent flow by 60 grit sand paper 2.5 cm width in the streamwise direction. Downstream 30 cm of the sandpaper, smoke was introduced through a slit in a port at the bottom of the wind tunnel. The smoke travels along the bottom of the tunnel 132 cm downstream to the measurement location as shown in Figure 4.1. The average boundary layer thickness at this location is 5.6 cm for this trial.

The smoke machine used for this experiment is a ViCount Compact 1300 oil-based smoke generator that produces particles 0.2-0.3 micrometers in size. The smoke fills a reservoir below the tunnel and then is pulled into the wind tunnel via a 10 cm slit that is 3.2 mm in the streamwise direction. The smoke flows along the bottom of the wind tunnel and seeds

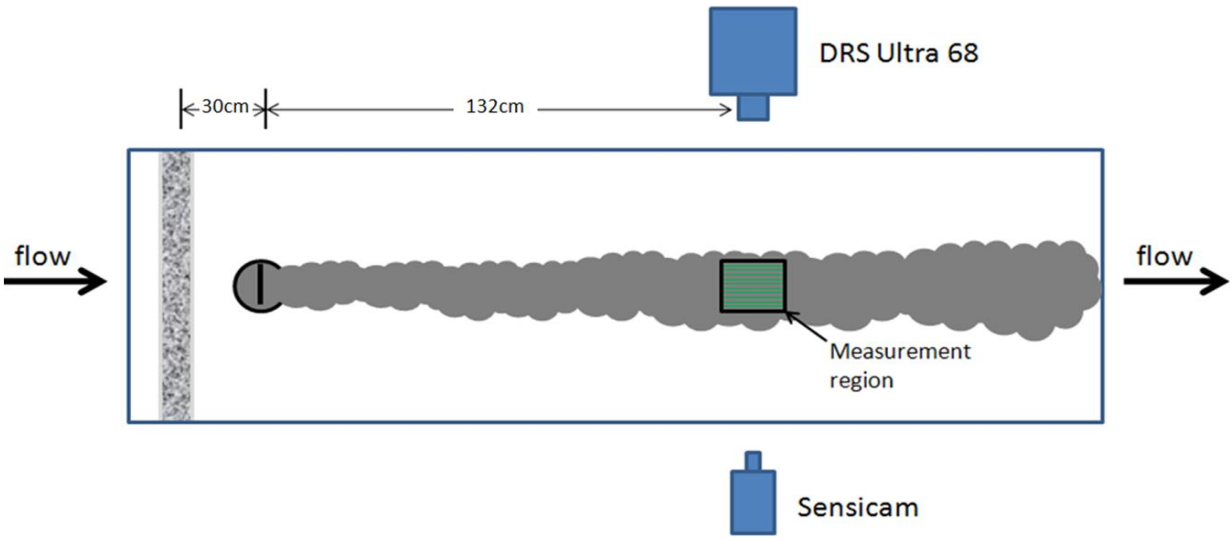

Figure 4.1: Overhead view of experimental setup

the boundary layer. The open circuit wind tunnel allows the room to fill up with smoke so as to seed the freestream flow at a much lower density than the seeded boundary layer. This was important so that PIV could be taken on the whole flow field while still filling the boundary layer for flow visualization. For this experiment, pitot probe measurements of the boundary layer thickness were performed with and without smoke and no differences were noted. (It should be noted that the assumption that the slit does not affect the boundary layer is not accurate, and a true test to determine its effect is shown in Chapter 5 by testing the boundary layer with the slit covered and uncovered.)

4.2.2 2-D Particle Image Velocimetry

A camera and laser were positionted to capture PIV measurements in a plane through the center of the measurement volume. A New Wave Research Solo III PIV laser at a wavelength of 532 nm was used for the PIV measurements. It provides 50 mJ of energy per pulse with a duration of 3-5 nsec. The laser was directed from the top of the tunnel down to illuminate a plane of the flow. The camera for the PIV trials is a Cooke Corp. Sensicam QE Doubleshutter 12 bit CCD camera. The time delay between frames was set to 25 microseconds. Each PIV image was 1376 by 1040 pixels. The field of view was 1.6δ by

1.3δ., where δ is the boundary layer thickness. The window size for the interrogation areas for the PIV measurements was 32 by 32 pixels with a step size of 16 pixels. A multi-pass technique was used with symmetric phase only filter (SPOF) for velocity calculations. SPOF is a technique used in cases of image data that contain sharp contrasts in image intensity such as at the boundary layer edge in this experiment. The SPOF decreases the possibility of discontinuities at the boundaries due to seeding concentration differences [63].

Special attention was paid to the seeding of the boundary layer and the freestream flow, where a proper balance in their relative intensities is necessary for the PIV algorithms to work properly. It should be noted that modern PIV algorithms are fairly robust with respect to the dynamic range associated with the particle image. Instances in which there was too much smoke in the boundary layer were discarded because the PIV processing could not detect particles and thus would not calculate the velocity in that portion of the flow. Instances in which there was not enough smoke in the boundary layer were also discarded due to poor intensity for the flow visualization images. A robust post-processing technique was used to replace missing and spurious vectors and to smooth the data [64].

4.2.3 3-D Flow Visualization

In this work, the term flow visualization images is used to represent the intensity images that result when smoke is introduced into the boundary layer through a slit, as is done in a traditional fashion. Three-dimensional flow visualization is accomplished by scanning a high-repetition rate laser light sheet through the desired flow field and acquiring 2-D images of the flow throughout the scan. The resulting sequence of 2-D images can then be reconstructed to form a 3-D image of the flow field. The unique aspect of this 3-D technique is its high speed capabilities which are made possible using a third generation pulse burst laser system with a galvanometric scanning mirror and a high framing rate CCD camera.

The main piece of instrumentation used in this technique is a home-built pulse burst laser system that is capable of producing laser pulses at repetition rates in excess of 1 MHz

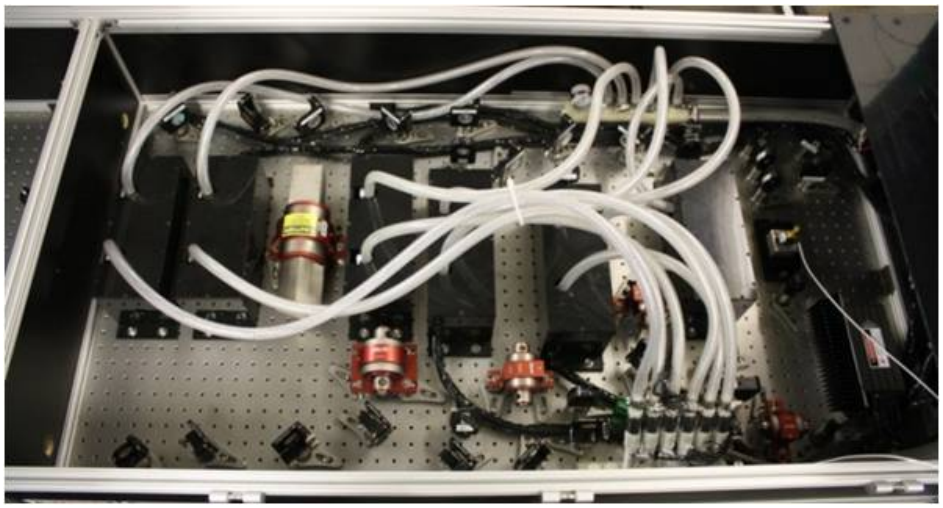

Figure 4.2: Photograph of pulse burst laser

over a 1 msec long window. In the experiments described in this paper the laser energy was approximately 15 mJ/pulse. For 3-D flow visualization, a burst of 68 laser pulses is produced at 500 kHz (camera limited) repetition rate and deflected off of a 6 mm aperture galvanometric scanning mirror. A long focal length spherical lens and a cylindrical lens located in front of the scanning mirror are used to form an approximately 1 mm thick laser sheet whose position is determined by the momentary angle of the scanning mirror.

For this experiment, the laser was directed from the bottom of the wind tunnel up through the flow to illuminate planes for image reconstruction. The mirror scans the planes from front to back in a nearly instantaneous fashion. Images are acquired for each successive laser pulse using a DRS Hadland Ultra68 intensified camera. The Ultra68 is capable of acquiring 68 images with 220 x 220 pixel resolution at framing rates up 500,000 frames per second. Thus, a sequence of 68 images can be acquired in 136 microseconds. For the speed in this experiment (22.4 m/s), the maximum displacement of the flow from the first image to the last image is less than 2.5 mm.

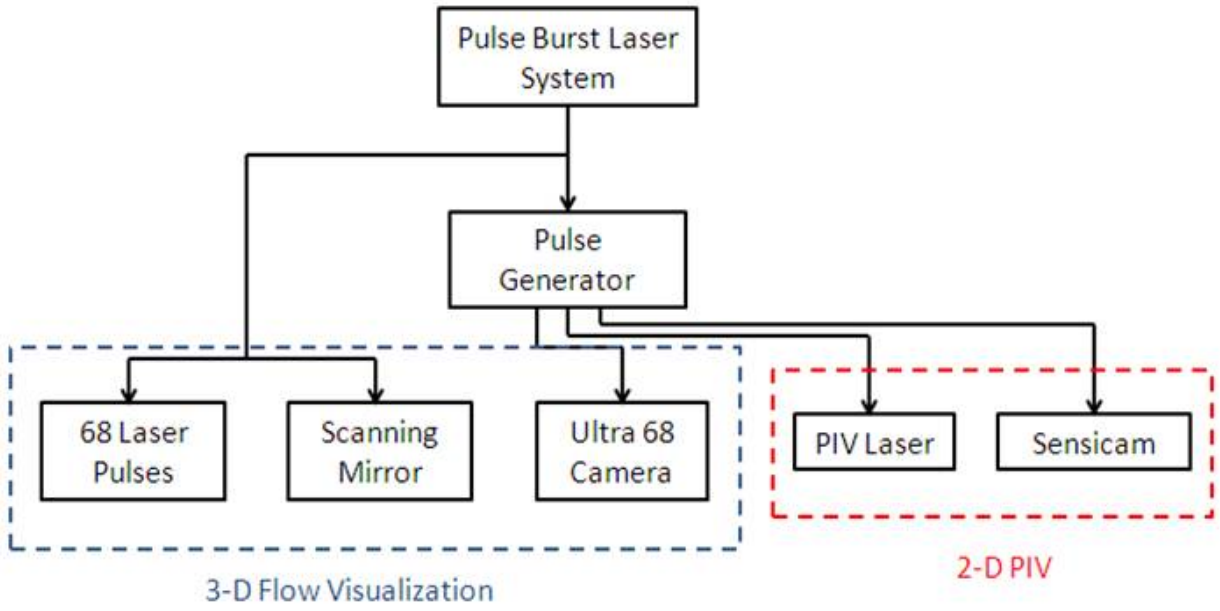

Figure 4.3: Synchronization of flow visualization and PIV

4.2.4 Synchronization

One major difficulty in this experiment lies in the synchronization of the 3-D flow visualization and the PIV. The trial was designed so as to capture the PIV immediately after the 3-D flow visualization images were captured. Figure 4.3 illustrates the timing of the system. The pulse burst laser system continuously sends a 2Hz signal to the scanning mirror and the 68 laser pulses. The pulse generator must be manually armed each time a sequence is desired to be captured. After armed, the pulse generator outputs a one-time signal to the flow visualization camera, PIV laser, and PIV camera. The delays for each signal from the pulse generator can be adjusted to ensure that the cameras and lasers are firing at the appropriate times. Detection of the firing of the cameras and lasers was monitored on an oscilloscope to ensure appropriate synchronization. The first PIV image was acquired 2 microseconds after the last slice of the 3-D image, therefore the overall structure of the flow had a negligible displacement between last frame of the 3-D flow visualization sequence and the first frame of the PIV.

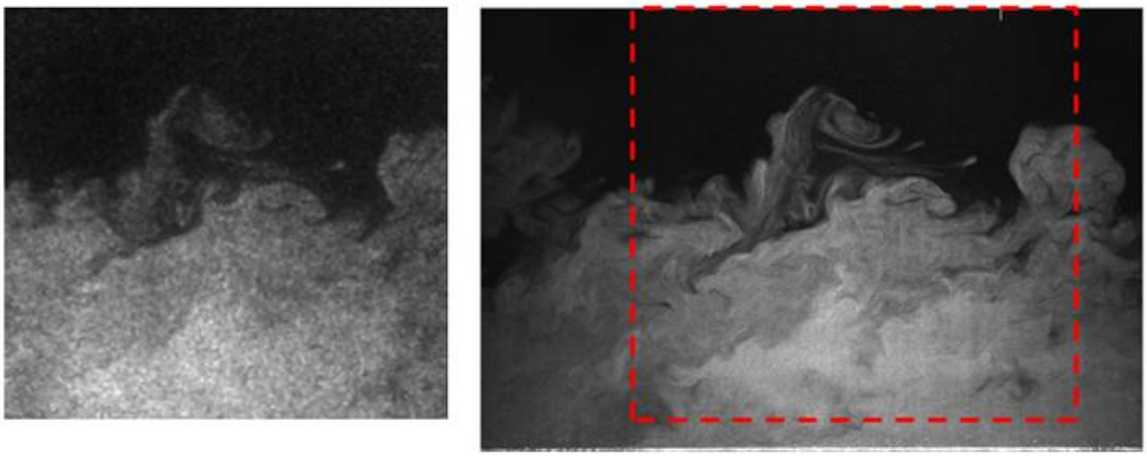

Figure 4.4: Middle slice of flow visualization image (left) compared with image for use in PIV (right)

Figure 4.4 shows the middle slice of the flow visualization sequence and the image used for PIV calculation. One can note the similarity of the flow indicating that these images were taken at nearly the same instant in time, which verifies the proper timing of the system. Figure 4.4a is slice 32 out of the 68 slices for the 3-D flow visualization image which corresponds with the image for use in PIV measurements in Figure 4.4b. A noticeable difference in the images is the resolution as the flow visualization images are 220 by 220 pixels whereas the PIV images are 1376 by 1040 pixels. Although it is not apparent in the images, the particle density is sufficiently high in the free stream for reliable determination of the local velocity.

4.3 Experimental Results

In all, 218 sequences were successfully captured in which the flow seeding was appropriate. Each sequence was composed of 68 images to reconstruct a 3-D flow visualization image and 2 images at the center of the measurement volume to use for PIV.

4.3.1 Boundary Layer Validation

Because the particle seeding is inhomogeneous throughout the measurement volume, it is important to show that the velocity measurements made using PIV are consistent with other measurements. The turbulent boundary layer statistics are compared with those of classical turbulent boundary layers. The following boundary layer statistics were calculated using PIV on the set of 218 pairs of images.

Table 4.1: Boundary layer parameters

U (m/s)	δ (mm)	δ^* (mm)	θ (mm)	u_τ (m/s)
22.4	56.4	3.99	2.84	0.83

Because it was difficult to measure very close to the wall (due to laser reflections from the wall), the friction velocity was calculated using the method described by Kendall fitting the data close to the wall with the Spalding profile [65]. As seen in Figure 4.5a, the boundary layer profile follows the 1/7th power law as expected for a turbulent boundary layer flow. Also in Figure 4.5b, the few points in the log layer do agree with the log law of the wall for turbulent boundary layers. The agreement between the PIV data and a canonical turbulent boundary layer velocity profile provide validation that the PIV algorithms employed here are robust enough to handle the inhomogeneous smoke seeding necessary for these experiments. Thus, both flow visualization and PIV images are acquired under the present seeding conditions.

4.3.2 3-D Flow Visualization

One main aspect of this research was to capture the 3-D structures in the turbulent boundary layer with the current 3-D flow visualization technique. Previous work with the technique has proved capable of visualizing the turbulent boundary layer, however, this experiment allowed the room to fill up with smoke so as to seed the freestream flow. The mean intensity of the smoke in the freestream flow was subtracted from the flow visualization

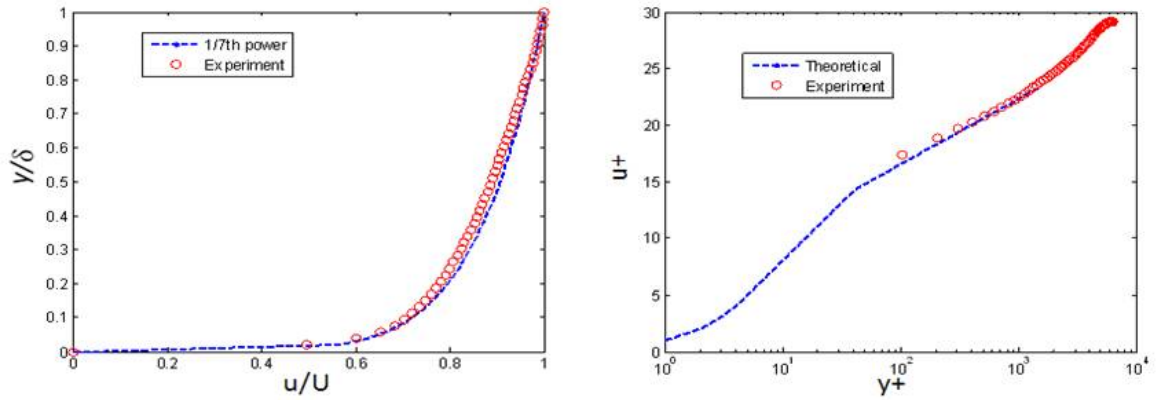

Figure 4.5: Graphs of boundary layer profile (left) and the log law of the wall (right)

images prior to 3-D image reconstruction. For 3-D reconstruction, each sequence of 68 images is converted to a compatible format for use in Tecplot. Using this software, the visualization can be rotated, dissected into slices, fit with multiple iso-surfaces, and manipulated to better investigate structures. The most common approach for visualization is to fit a surface through a constant value of intensity in the image (i.e. an iso-surface). By judicious choice of the intensity value, one can view different layers within the boundary layer. Generally, an intensity corresponding to the edge of the boundary layer is chosen such that the outer structure of the boundary layer can be observed. This is illustrated in Figure 4.6, which shows the outer 3-D structure at three moments in time. For viewing the internal structure, virtual fly-throughs can be performed the data. Unfortunately, this type of analysis is difficult to present in paper format.

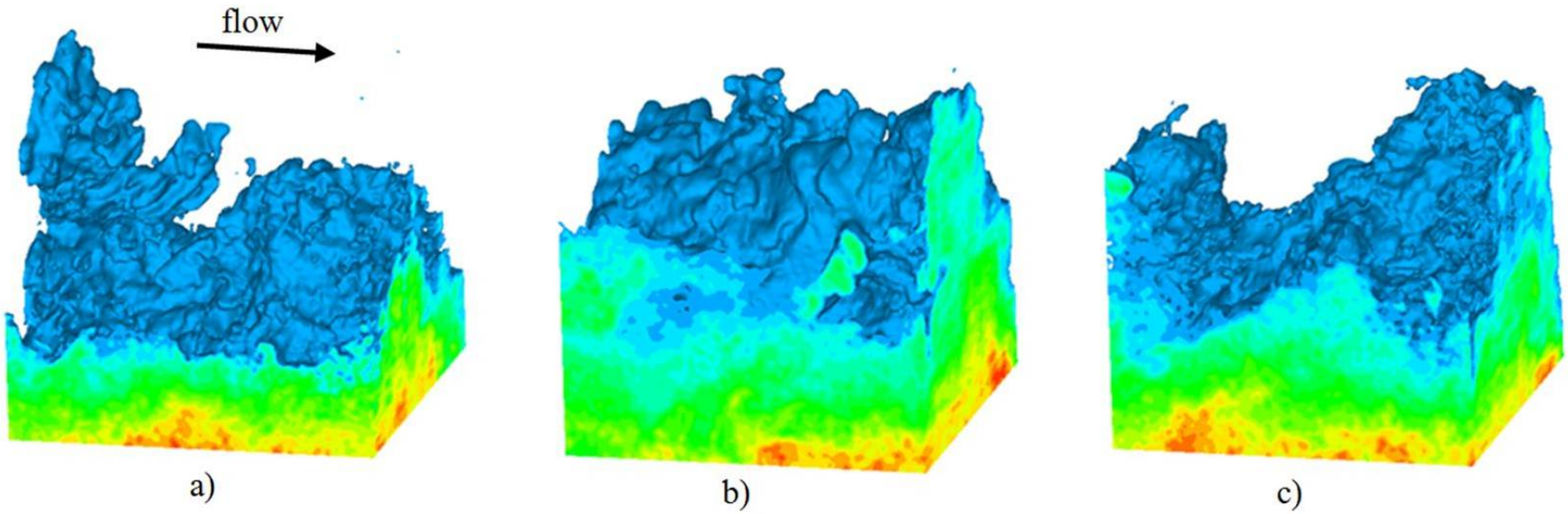

Figure 4.6: 3-D flow visualization images at 3 different instances

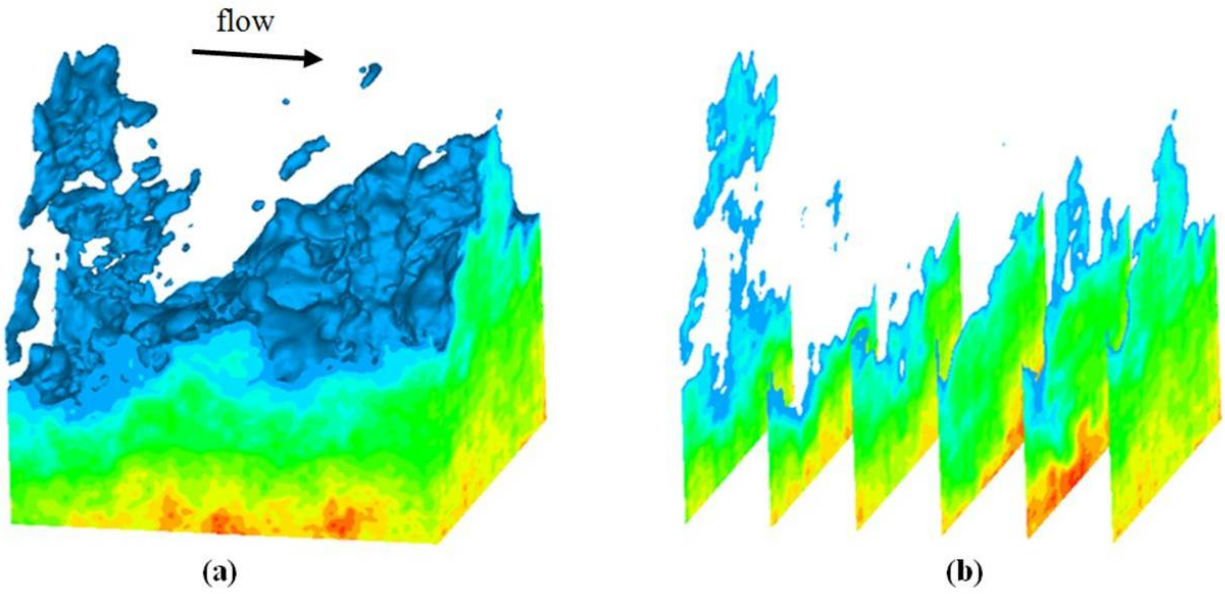

Figure 4.7: 3-D flow visualization image (a) decomposed into slices for easier investigation of structures (b).

A wide variety of shapes and structures were observed in the 3-D images obtained. In many instances, one can see large scale sweeping motions with size on the order of one boundary layer thickness or greater inclined at approximately 45 degrees to the flow. This is apparent in Figure 4.6c where the bulge observed at the front of the imaging volume extends across the span of the volume. Figure 4.6b, on the other hand, shows a more uniformly distributed boundary layer thickness composed of several smaller structures. In this case, there is a narrow spire of fluid that can be seen on the forward endcap. Figure 4.6a appears to show an eruption of fluid on the upstream portion of the image while downstream is marked by a mild hill.

In addition, because the images are reconstructed in computer software, the inner details of the flow can also be observed. Figure 4.7 shows a 3-D flow visualization being deconstructed to look at individual slices of the flow. In this case, the details of how the boundary layer thickness varies along with an eruption of fluid in the upstream portion of the volume are clearly seen. One can see the advantages of 3-D flow visualization in studying the turbulent boundary layer. Further discussion and analysis of these images; however, is

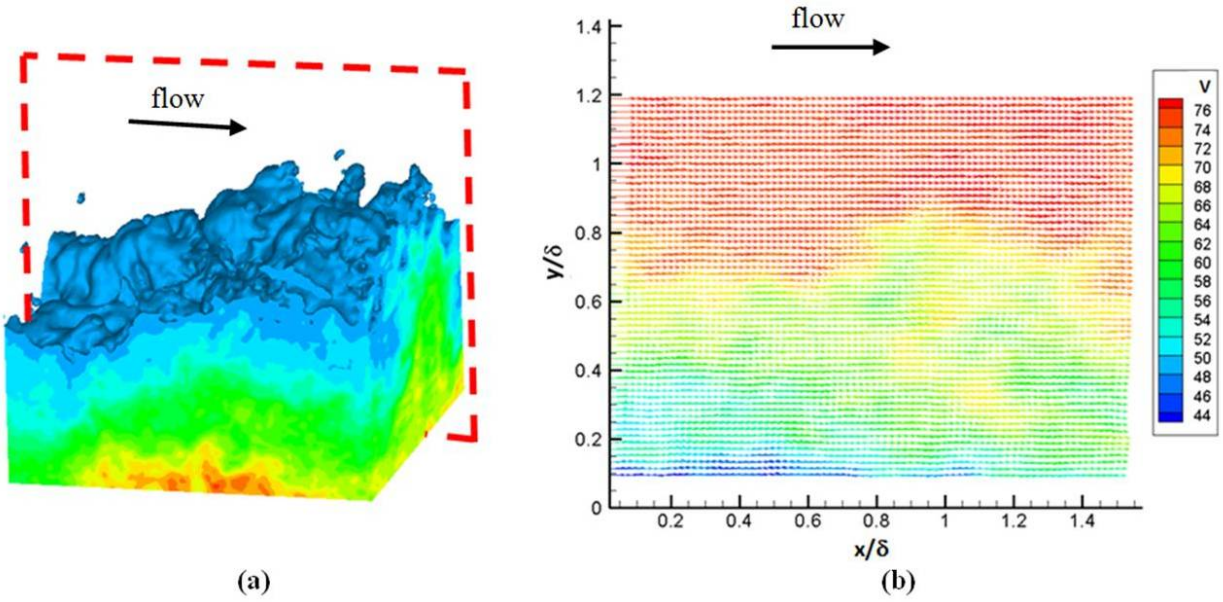

Figure 4.8: 3-D flow visualization image (a) and corresponding 2-D velocity field (b)

difficult due the ambiguous nature in which the smoke is actually visualizing the boundary layer. Better understanding the connection between the underlying velocity field and the smoke based 3-D flow visualization is the primary objective of this effort.

4.3.3 Comparison of 3-D images with 2-D PIV

The new aspect of this trial is the simultaneous PIV measurement taken at the center of the 3-D image. For each of the 218 3-D realizations, a simultaneous snapshot of the velocity (and vorticity) field is acquired to complement the flow visualization data. The velocity measurements provide a quantitative look at the flow. Figure 4.8 illustrates the complementary flow visualization and PIV data captured for each realization.

One area of concern is the determination of the edge of the boundary layer. With flow visualization it is assumed that the smoke stays in the boundary layer and does not diffuse into the freestream flow. In flow visualization, therefore, the edge of the smoke is picked to be the edge of the boundary layer; however, it is not clear if the underlying turbulence structure that convected the smoke to this location in the first place remains intact between the smoke injection point and the measurement volume. The simultaneous acquisition of velocity and

intensity data, however, allows one to directly compare the edge of the boundary layer as determined in flow visualization and velocity fields.

Figure 4.9 illustrates the comparison of the flow visualization data with the PIV data. It displays three different sequences at three different instants in time. Figure 4.9a displays the 3-D representation of the boundary layer formed using the 68 slice image sequence. In figure 4.9b, the flow visualization slice in the middle of the sequence is extracted. A thick line is used to trace the edge of the boundary layer, which is determined (in this case) by selecting an intensity value that distinguishes the seeded fluid from the much lower intensity free stream values.

It should be noted that the choice of intensity for marking the boundary layer's edge is somewhat arbitrary and only used here for illustrative purposes. Figure 4.9c shows the velocity field measures at the same 2-D location with the edge of the boundary layer (as determined from the flow visualization image) marked. A general observation is that there is fairly good agreement between the velocity and the flow visualization edge. The boundary layer edges are not exact, but are similar with these three sequences (and the other sequences as well).

Figure 4.9d presents the associated vorticity field with the flow visualization boundary layer edge laid on top of it. Observation of the vorticity is a convenient way to separate the rotational fluid within the turbulent boundary layer from the irrotational fluid in the free stream. In these images, a threshold is set so that only vorticity values above the noise floor are displayed. As seen in part d of figure 4.9, the edge of the boundary layer from flow visualization corresponds with the contrast between vortical flow and non-vortical flow. Again, the edge may not be exactly the same, but in general, the boundary layer edge from flow visualization matches the data from the velocity and vorticity fields. This enhances the certainty in defining the boundary layer edge as the edge between seeded flow and non-seeded flow.

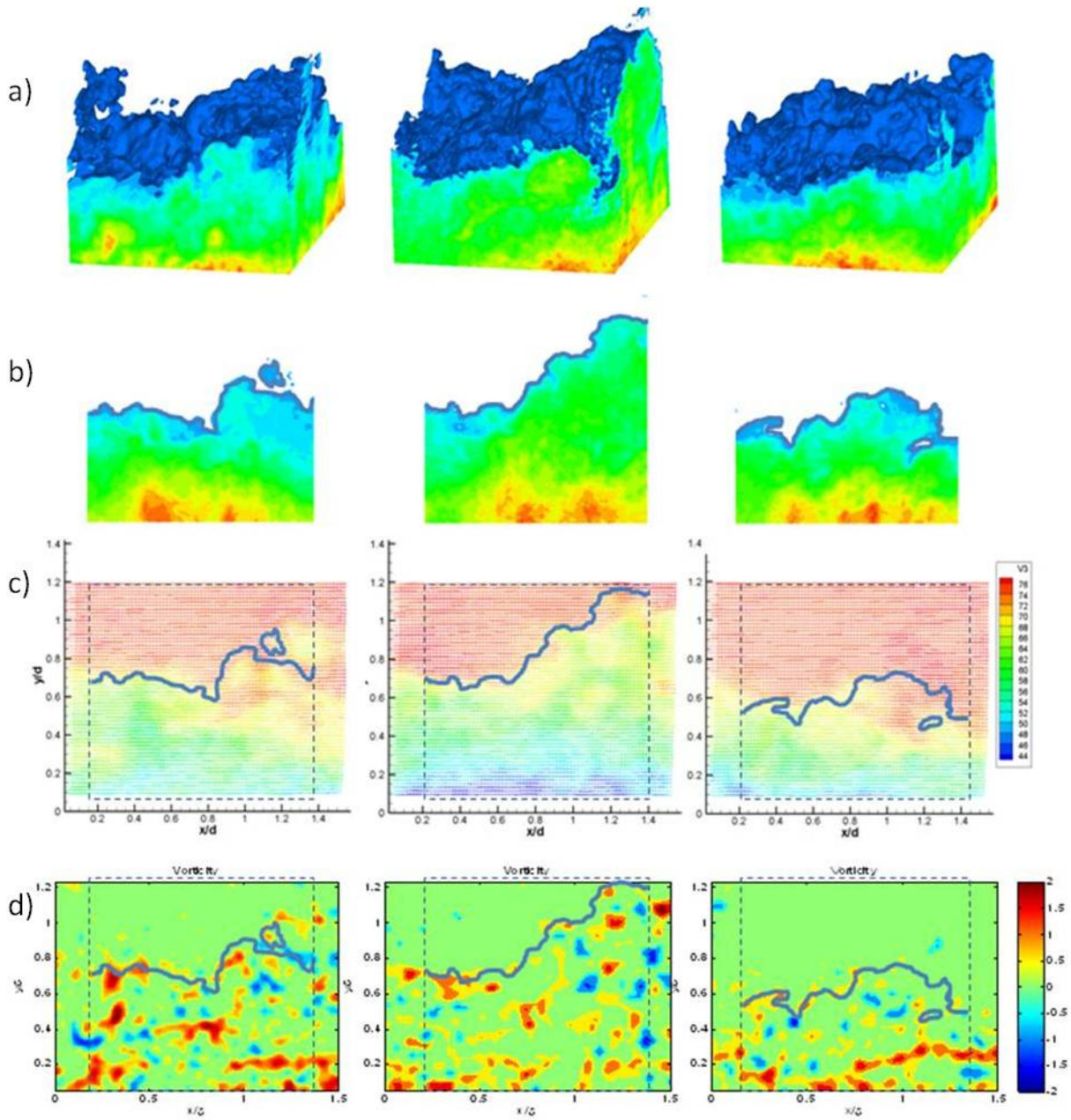

Figure 4.9: 3-D flow visualization image (a), middle slice from flow visualization (b), corresponding 2-D velocity field (c), and corresponding 2-D vorticity field (d) with boundary layer edge from flow visualization overlaid for 3 different instances.

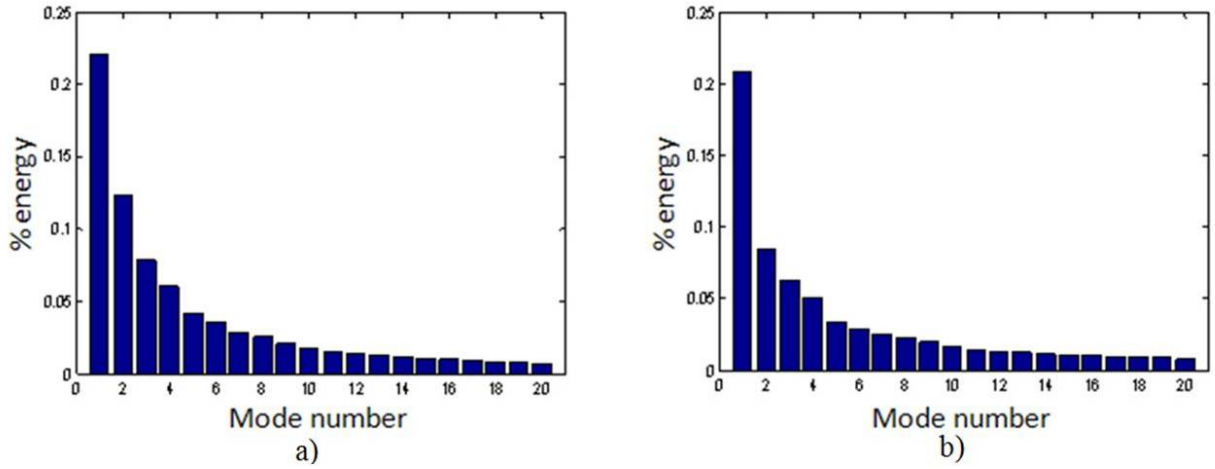

Figure 4.10: Modal energy distribution of first 20 modes for middle slice flow visualization (a) and velocity (b)

4.3.4 Proper Orthogonal Decomposition

Many observations can be made by studying individual snapshots of the flow. There are, however, some efficient ways to decrease the data into more manageable sets, while still being able to make observations about the structures in the flow. Lumley, in 1967, first proposed using POD to detect coherent structures in turbulent flows [60]. Recently, POD and LSE have emerged as tools for identifying structures in the boundary layer using various forms of data, including PIV. The method of snapshots is used to take all 218 sequences and extract the most energetic structure into POD modes. The proper orthogonal decomposition can be performed on the 3-D flow visualization, a 2-D slice of the flow visualization, and the 2-D velocity data. POD can give insight into the structures that are observed in the flow. Additionally, the POD modes obtained from the flow visualization images can be compared with those obtained from the velocity data to provide a possible connection between the two. In this chapter some preliminary observations will be made about the POD, with the knowledge that more trials and a large set of sequences will be acquired in the future. The results presented in this chapter illustrate the basic premise of the methodology described, and are some of the observations.

Figure 5.8 shows the energy of the first 20 modes for 2-D flow visualization and 2-D velocity. Like most POD modes, a good portion of the energy lies in the first few modes for both flow visualization and velocity. The convergence of modal energy is quite similar between the two, although some differences can be determined. One noticeable difference is the relative energy in the second mode for both instances. Again, a larger dataset would help improve the accuracy of these POD modes.

To further examine the correlation between the structure observed in the velocity field and the intensity fields, correlations were calculated between the POD time coefficients determined from the velocity modes and intensity modes, respectively. In other words, each image (whether velocity or intensity) in the set was projected onto the first 20 POD modes calculated from the set. In this fashion, the velocity field at an instant in time is represented by the 20 time coefficients obtained through projection onto the POD velocity basis. The intensity field is represented, in a likewise fashion, through projection onto the POD intensity basis. A correlation between the time coefficients of each representation was then performed over the entire data set. The presumption in this case is that if the structure in the intensity field (as best represented through the POD intensity modes) is random relative to the structure observed in the velocity field (as best represented through the POD velocity modes), then there should be no correlation between their time coefficients. On the other hand, if the structure is similar, then there should be a measurable level of correlation between the two representations of the flow.

The value of the correlations is shown graphically in Figure 4.11a where it should be noted that a negative correlation is just as meaningful as a positive correlation. In this figure, the correlation coefficients have magnitudes of up to 0.5, which is significant considering the differing nature of the data (velocity vs. intensity). Moreover, one can observe that the modes are roughly ordered in the same way such that the most energetic velocity modes correlate best with the most energetic intensity modes and vice-versa. This is not to say that the modes represent a perfect match with each other. Rather, they do not. For example,

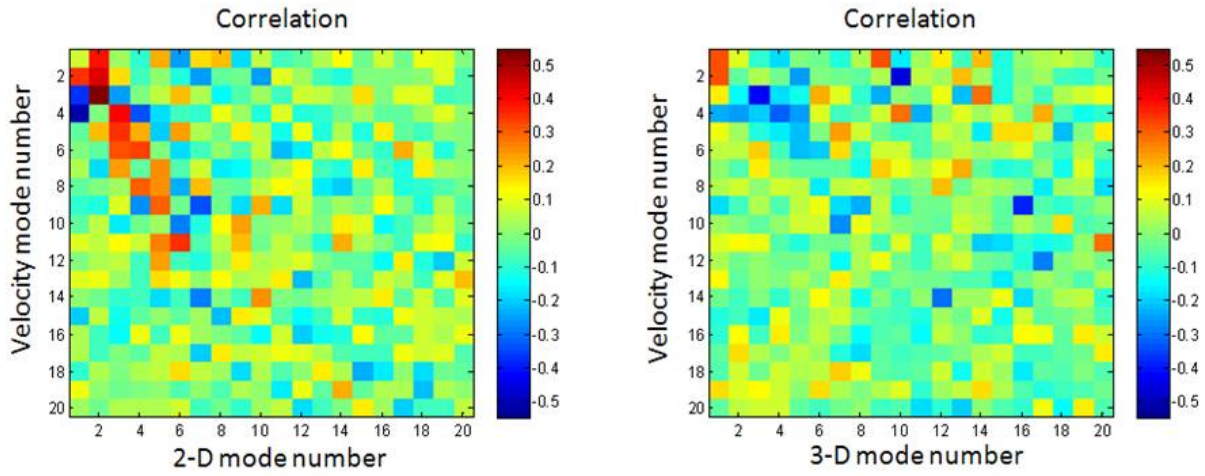

Figure 4.11: Correlation between the velocity modes and the (left) 2-D flow visualization modes and the (right) 3-D flow visualization modes

mode 2 of the intensity data appears to correlate with modes 1, 2 and 3 of the velocity field. Further thought is necessary to better understand the full implications of this analysis.

In light of the ultimate objective of this work, which is to relate 3-D flow visualization images to the underlying velocity field, a similar analysis was conducted using POD modes constructed from the 3-D intensity images. In a similar fashion as before, each 3-D image is represented by the time coefficients of the first 20 POD modes. The correlation between the time coefficients based on the 3-D image and the time coefficients based on the 2-D velocity field are shown in Figure 4.11b. In this case, the magnitude of correlation is much lower. This result suggests that the structure represented by the 3-D POD modes does not project well onto a 2-D velocity representation of the same flow field. This is in contrast to the 2-D intensity data, which did project well on the 2-D velocity representation of the same flow field. This is evidence that the 3-D nature of the flow is more complex and worthy of further investigation.

4.4 Discussion

The simultaneous application of PIV and 3-D flow visualization based on the seeding of a boundary layer with smoke presents multiple representations (i.e. 2-D velocity field, 2-D intensity and 3-D intensity) of the same flow field. The objective of the experiment in this chapter is to assess to what degree these different representations are similar.

Qualitative comparison between the 2-D intensity images and 2-D velocity field show that the boundaries (i.e. intensity gradients) observed in the intensity field correspond quite well with boundaries observed in the velocity field. In particular, the outer most edge of the boundary layer, which exhibits the strongest contrast in intensity, is well captured using an intensity threshold. Intensity gradient internal to the boundary layer and visible in a high quality flow visualization images also appear to match well with different regions in the velocity field. It is difficult to extend this conclusion to the 3-D data, however, due to the relatively poor quality of 2-D slices that constitute a 3-D image. Examination of the vorticity field yields a similar result where the boundaries between regions of different intensity appear to be marked by trains of vortices.

To provide another viewpoint of this problem, proper orthogonal decomposition was applied to both the velocity data and intensity data as a means of objectively identifying the large-scale structures that form the basis for the instantaneous representations of the flow. Further analysis was conducted by comparing the simultaneous occurrence of POD intensity and POD velocity modes. A significant degree of correlation was found between these modes to suggest that many of the large scale features present in the flow are well represented in both the flow visualization and velocity data. The ordering of these modes (and relative importance) was similar, but does not present a one-to-one correspondence between POD modes of different types. Furthermore, the correspondence between modes did not carry over as well to a 3-D representation of the flow based on intensity data. This indicates that the 3-D structure of the flow is markedly different than that 2-D structure giving further credence towards the need for 3-D models of the turbulent boundary layer.

Nonetheless, the similarity between the intensity fields and the velocity data was somewhat surprising and encouraging. To explain this connection, the following picture is presented to describe the relationship between the smoke based intensity images and the velocity field. The premise is that smoke serves as a passive scalar that marks the low momentum regions of the boundary layer. As the smoke is injected into the boundary layer at the wall, it essentially marks the low momentum fluid upstream of the measurement volume. The only means by which the smoke can be shifted away from the wall is through the shedding of vorticity, which leads to the formation of vortices in the boundary layer. The action of these vortices is to bring unseeded high-momentum free stream fluid into contact with the low momentum fluid near the wall forming sharp discontinuities in the image intensity. This action continues throughout the evolution of the boundary layer such that multiple intensity levels are formed within the boundary layer. Conceptually, this picture is similar to that presumed in earlier works employing smoke or dye based flow visualization; however, it has not been as rigorously tested as it is here. The preliminary observations of this work are consistent with the ideas presented here; however, it is somewhat surprising that these ideas hold over large distances downstream from the smoke injection point. This latter point is likely a consequence of the minimal dissipation present in this high Reynolds number flow.

At this point, the above picture is a good working hypothesis and in need of much more consideration and work. Nonetheless, the overall results are particularly encouraging in the context of the objectives of this chapter which seeks to provide a solid foundation upon which to interpret 3-D flow visualization images.

The experiment presented in this chapter serves as the impetus for better, and more detailed examination of the true effect of the slit on the boundary layer and a more in-depth look at the connection between the smoke intensity and velocity measurements in Chapter 5. In addition, larger set of images will be obtained that is more suitable for POD analysis, particularly for higher order modes that represent some of the smaller scale features of the flow. Linear stochastic estimation will also be used to estimate the velocity

field from instantaneous flow visualization snapshots to give a rough estimate about the underlying velocity field. Future enhancements to the trial described in this chapter also include capturing a larger number of flow visualization volumes with a higher resolution camera to better investigate the structures in the flow.

Chapter 5

On the Relationship Between Image Intensity and Velocity in a Turbulent Boundary Layer Seeded with Smoke Particles

5.1 Introduction

This chapter presents a comparison of flow visualization (image intensity of light scattering by smoke particles) and velocity measurements (from PIV) of a seeded turbulent boundary layer. The motivation of this chapter is the long-term goal of using a high-speed scanning technique in conjunction with classical flow visualization techniques to observe the 3-D organization of large scale and very large scale structures in boundary layers with adverse pressure gradient. Due to their large dimensions (on the order of 10s of boundary layer thicknesses), observation of these structures with PIV is often not possible and flow visualization through smoke injection remains a powerful investigative tool. As such, this chapter provides further investigation of the strengths and limitations of smoke visualization with a particular emphasis on how accurately the smoke marks the edge of the boundary layer and the correlation between the structures observed in flow visualization images and those observed from planar velocity fields.

Over the years, researchers have pieced together a generally accepted picture of a turbulent boundary layer as discussed in Chapter 2. Flow visualization, such as seeding smoke into the boundary layer, has historically served an important role in determining details of the underlying structure of a turbulent boundary layer. The flow visualization trials of Praturi and Brodkey, Head and Bandyopadhyay, and Smits and Delo, among others, have led to very important discoveries of the structures in a turbulent boundary layer [45, 13, 46]. In fact, much of the current understanding of the turbulent boundary layer has flow visualization experiments at its roots which often lead to more detailed investigation.

The separation of the vortical boundary layer and irrotational freestream flow and the entrainment process at the boundary layer edge has been studied as far back as Corrsin and Kistler in 1954 and Kovasznay et al. in 1970 [6, 8].

Expanding to 3-D flow visualization, Goldstein and Smits in 1994, Delo and Smits in 1997, and Delo, Kelso, and Smits in 2004, studied a zero pressure gradient turbulent boundary layer, giving insight to its coherent structures [40, 20, 54]. They clearly saw large-scale structures in the x-z plane (where y is the wall-normal direction) aligned along diagonals +/- 50 degrees from streamwise. The spacing along the lines varied, but was approximately 1δ in the outer portion of the boundary layer. This spanwise orientation had not been documented extensively before this experiment. They also found that ejections appear to be spatially organized and linked to the passage of the large scale motions [20].

To this end, the relationship between flow visualizations and more developed techniques, such as PIV is further explored. Two-dimensional image pairs at different velocities and different downstream locations on the wind tunnel wall have been captured. The image pairs can be used for velocity measurements through PIV, or can be downsampled for flow visualization of smoke intensity. The effect of the slit and of the smoke on the boundary layer parameters is determined and the boundary layer edge in flow visualization is compared to velocity measurements. A direct correlation between velocity deficit and smoke intensity is used for comparison and for calculation of a velocity deficit field given only the flow visualization image. Proper orthogonal decomposition is used to calculate the modes (building blocks) of the flow visualization and velocity fields. Using the correlation between the POD modes, the relationship between smoke intensity and velocity is explored and linear stochastic estimation is then used to construct an estimated velocity deficit field for a given flow visualization image. This estimation can be compared to the actual velocity deficit field measured by the PIV. This complementary POD/LSE approach is used for two reasons: first, to see the correlation between velocity modes and flow visualization modes, and secondly, to test the ability of flow visualization images to estimate a velocity deficit field. This technique

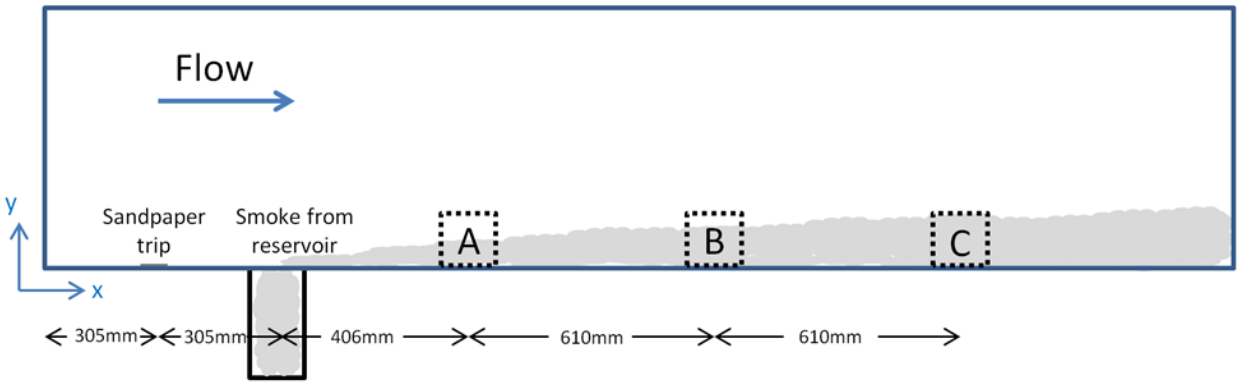

Figure 5.1: Side view of experimental setup

is not suggested as a means of estimating the velocity, but as an exercise to further explore the relationship between smoke intensity and velocity deficit.

5.2 Experimental Arrangement

Experiments were conducted in the Auburn University Advanced Laser Diagnostics Laboratorys 0.6 m x 0.6 m wind tunnel. The tunnel is an open circuit, blow-down wind tunnel, with a 2.4 m long test section and a maximum speed of 30 m/s. A 2.5 to 1 square contraction with 1.8 m length is used to accelerate the flow to the square test section. The test section is preceded by a stainless steel honeycomb and three screens of 80% porosity to condition the flow and create a uniform velocity across the test section.

Experiments were performed to image the boundary layer formed on the bottom wall of the wind tunnel. The flow on the wall was tripped to a turbulent flow by 60 grit sandpaper, which extended across the entire span of the test section and 25 mm in the streamwise direction. The sandpaper can be classified as k-type roughness elements, which, for these cases, extended approximately 4 to 6% into the local boundary layer thickness. Downstream 305 mm from the sandpaper, smoke is introduced through a slit in a port at the bottom of the wind tunnel. The slit is 3.2 mm wide in the streamwise (x) direction (which corresponds to about 3% to 5% of the boundary layer thickness for the velocities studied in this paper) and 100 mm long in the spanwise (z) direction.

For this trial, three measurement locations were considered: 0.406 m, 1.016 m, and 1.626 m downstream of the slit, referred to as locations A, B, and C respectively. These distances correspond to approximately 8.5δ, 15.5δ, and 22.5δ using the local boundary layer thickness for the 14.5 m/s trial which varied slightly for the other freestream velocities. For each location, three different freestream velocities were considered: 6.9 m/s, 14.5 m/s, and 22.1 m/s. The Reynolds numbers based on momentum thickness were between 2100 and 8600 as shown in Table 5.1.

	Location		
	A	B	C
6.9m/s	2146	2604	2719
14.5m/s	4289	5469	5527
22.1m/s	6263	8396	8511

Table 5.1: Reynolds numbers (based on momentum thickness) for each case

The smoke machine used for this experiment is a ViCount Compact 1300 oil-based smoke generator that produces particles 0.2-0.3 micrometers in size. The smoke fills a reservoir below the tunnel and then is naturally pulled into the wind tunnel via the slit. The smoke flows along the bottom of the wind tunnel and seeds the boundary layer. The open circuit design of the wind tunnel allows the room to slowly fill up with smoke so as to seed the freestream flow at a much lower density than the seeded boundary layer. The freestream flow is seeded sufficiently so PIV can be performed on the whole flow field while still contrasting with the boundary layer for flow visualization.

A New Wave Research Solo III PIV laser at a wavelength of 532 nm was used for trials. It provides 50 mJ of energy per pulse with a duration of 3-5 nsec. The laser was directed from the top of the tunnel down through the upper wind tunnel wall and incident onto the bottom wall in order to illuminate a single streamwise/wall-normal plane of the flow. The camera is a Cooke Corp. Sensicam QE Doubleshutter 12 bit CCD camera. Each PIV image is 1376 by 1040 pixels. The field of view was approximately 64 by 84 mm in the wall normal and streamwise directions, respectively. The images were run through 5 cross-correlation

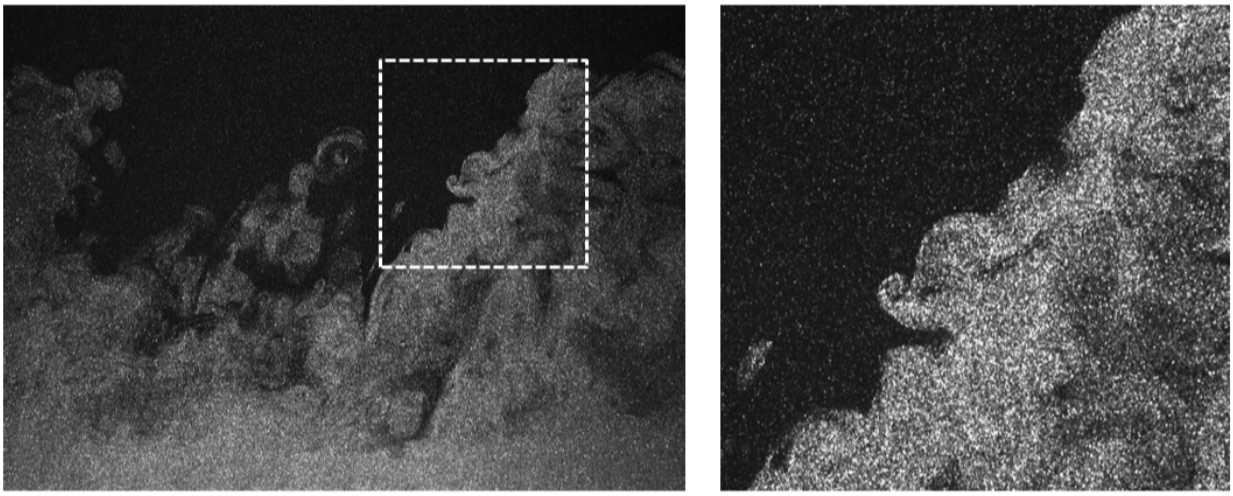

Figure 5.2: Sample image showing particles in the boundary layer and in the freestream flow

passes with window deformation with a starting window size of 128 by 128 pixels and a final window size of 32 by 32 with a 50% overlap. The final velocity field was 85 by 64 vectors. Files were converted to Matlab compatible matrices for calculations.

Special attention was paid to the seeding of the boundary layer and the freestream flow, where a proper balance in their relative intensities is necessary for the PIV algorithms to work properly. Flow visualization images work well with a fully seeded boundary layer and no smoke in the freestream; however, PIV processing requires images of individual particles throughout. As shown in Figure 5.2, the boundary layer was seeded with enough smoke for quality flow visualization images, while still able to distinguish individual particles, and the freestream was seeded with less smoke, but still enough for PIV processing. It should be noted that modern PIV algorithms are fairly robust with respect to the dynamic range associated with the particle image. A robust post-processing technique was used to replace missing and spurious vectors and to smooth the data [64].

In this paper, the term flow visualization is used to to represent the intensity images that result when smoke is introduced into the boundary layer through a slit, as is done in a traditional fashion. Many flow visualization techniques must also rely on lower resolution images. In order to emulate this effect, the same images used for PIV processing were

downsampled to a resolution of 344 by 260 calculating the average intensity of each 4 by 4 window of pixels. The intensity of the downsampled images are used in this flow visualization investigation, comparing the boundary layer edge and correlating the POD modes with velocity modes to gain insight into the relationship between the two given the same field of view at the same instant. In addition, for a direct correlation between intensity and velocity, the images were further downsampled to a resolution of 85 by 64 which corresponds to the same resolution of the vector fields produced using the PIV analysis.

5.3 Complementary POD/LSE Approach

In the current trial, there are 43,800 pixels in every flow visualization image, and 5,292 velocity vectors (each with an x and y component) in each velocity field. Correlating every pixel in the smoke intensity (flow visualization) images with every vector in the velocity field realizations could be quite intensive and unnecessary. However, proper orthogonal decomposition (POD) can be used to compress a dataset into a manageable set of spatial modes while still preserving the opportunity to make observations about the structures in the flow. In this case, the velocity mode coefficients are estimated given the known flow visualization mode coefficients.

To relate the flow visualization intensity to the velocity field, a complementary POD/LSE technique is utilized in which POD is used to compactly represent the intensity/velocity fields and LSE is used to connect them. First, the flow visualization images are used to calculate the flow visualization modes, and the PIV image pairs are used to calculate the velocity modes, as shown in Figure 5.3. For each image, the modes coefficients are determined by projecting the image onto the mode. The mode coefficients for all 1350 images are then used to develop a correlation between the flow visualization modes and the velocity modes. This correlation is then used to convert from flow visualization to velocity via Equation 3.

Once the flow visualization modes, velocity modes, and correlation matrix are calculated, a flow visualization image can be used to approximate a velocity field. The flow

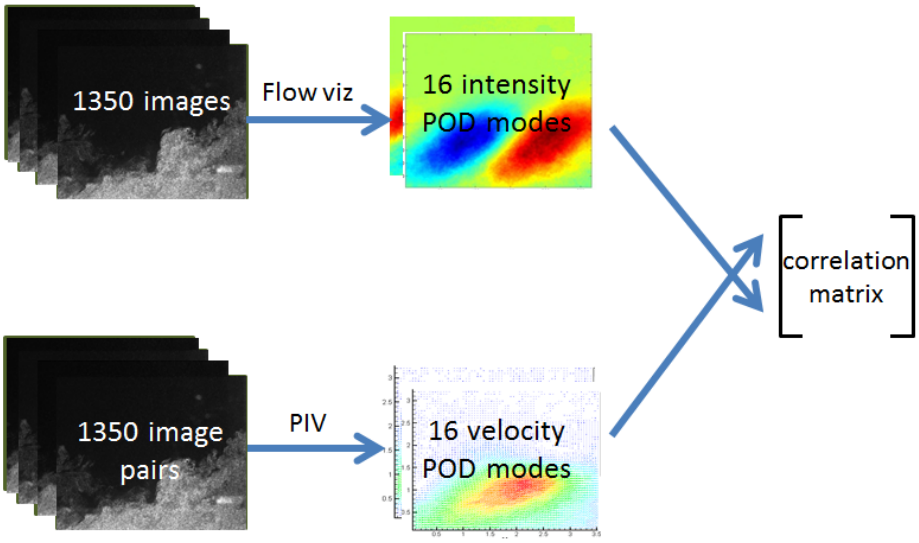

Figure 5.3: Diagram of complementary POD/LSE approach - creating correlation matrix

visualization image is projected onto the flow visualization modes to calculate the time coefficients. These coefficients are then converted to velocity mode coefficients via the correlation matrix developed previously. The new velocity coefficients are then applied to the velocity modes and summed to calculate the approximated velocity field.

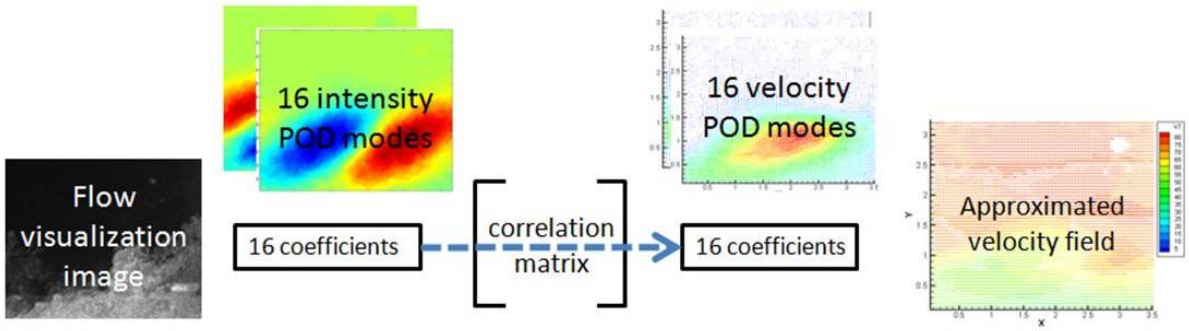

Figure 5.4: Diagram of complementary POD/LSE approach - estimating velocity

The accuracy of the approximated velocity field can be compared to the actual velocity field calculated at that same instant in time. It is strongly emphasized that this procedure is utilized here solely as an exercise to study the relationship between image intensity and

velocity; it is not suggesting this as a viable means of making velocity measurements in turbulent flow fields.

5.4 Experimental Results

5.4.1 Effect of slit and smoke

To determine the effect of the slit and smoke on the boundary layer, trials at locations A and B were run with the slit covered and uncovered at a freestream velocity of 22.1 m/s. For the first case, the freestream flow was seeded, and the slit was covered with tape allowing no air to be swept into the boundary layer. This case is labeled "no slit/no smoke" in Figure 4. In the second case, the freestream flow was seeded, and the slit was uncovered allowing air to be drawn in, but the reservoir under the slit was not filled with smoke, so the boundary layer did not fill with smoke. This is labeled "slit/no smoke" in the figure. In the third case, the freestream flow was seeded and the boundary layer was densely filled with smoke via the slit and reservoir and is labeled "slit/smoke" in Figure 5.5.

The impact of the slit and smoke is seen in the differences in the boundary layer profiles. For the two cases where the slit was uncovered, there is higher momentum fluid in the inner region of the boundary layer as seen in shape of the boundary layers for location A and B for the first two cases. The difference in the profiles at location B, which is further away from the slit, is less pronounced than the difference in location A.

A densely seeded flow has the potential to locally bias the velocity vectors by cross-correlating structures in the flow instead of the particles. To determine the effect of the dense smoke on the velocity measurements, case 2 (slit/no smoke) and case 3 (slit/smoke) were run with the only difference being the amount of particles being swept into the boundary layer via the slit. As seen in the boundary layer profiles, there is no noticeable difference in these two cases where the slit was uncovered. These two boundary layer profiles were nearly identical. The only noticeable difference in these two cases shows up in the Reynolds stresses, <uv>, where below a y+ value of about 1000, the stresses in the no smoke case

are slightly larger than when the smoke is introduced in the boundary layer. In the outer region of the boundary layer these differences are minimal as the data points collapse on each other.

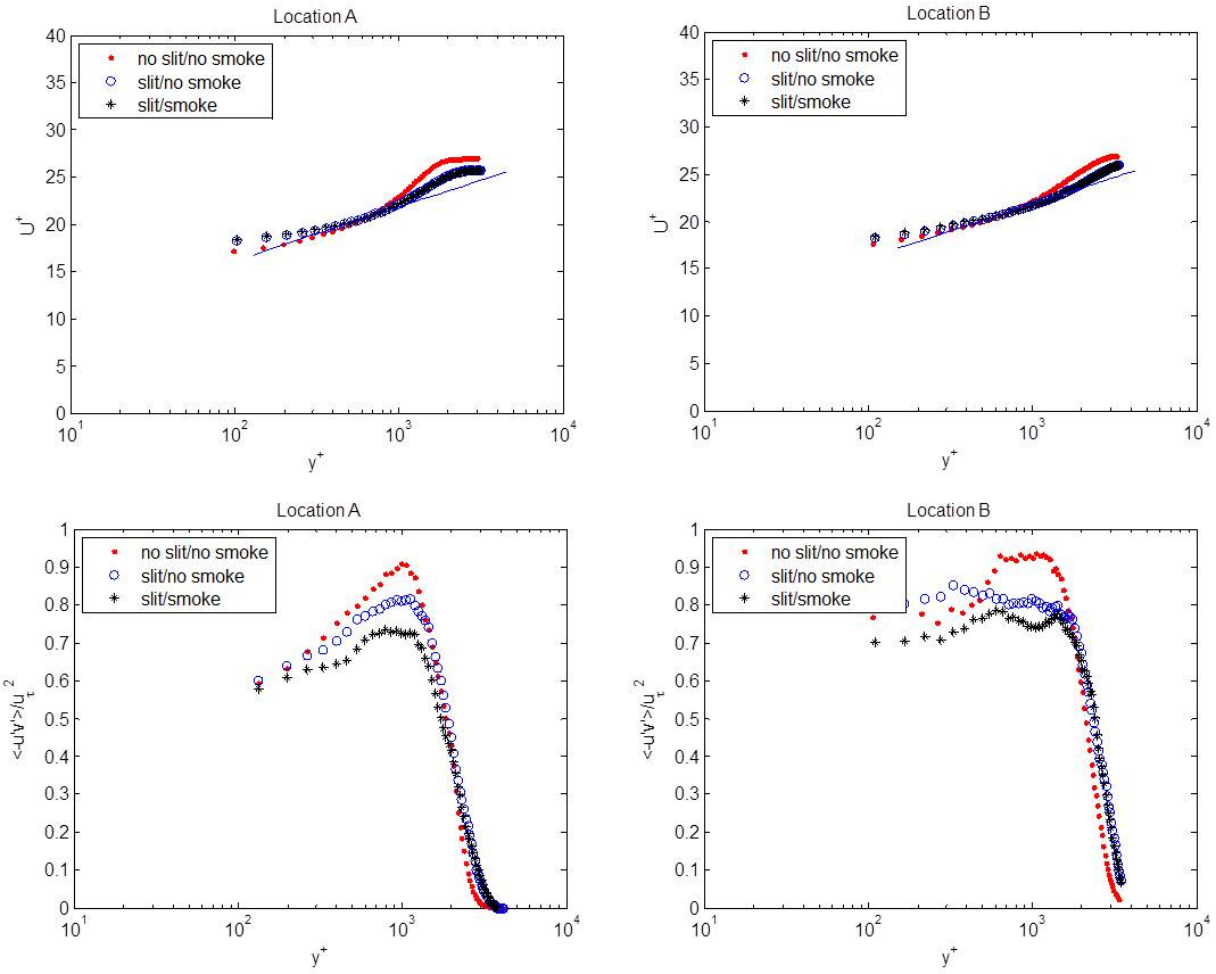

Figure 5.5: Comparison of boundary layer profiles with and without the slit, and with and without smoke - u^+ and $<-uv/u^\tau>$ locations A and B

For Locations A and B, the boundary layer thicknesses, δ, are increased by 8.6 and 2.0 percent respectively when the slit is uncovered. The presence of the slit also reduces the magnitude of the displacement thickness (δ^*), momentum thickness (θ), and shape factor (H). For each of these parameters, the impact on Location A is greater than the impact on Location B, indicating that the effect of the slit is reduced with downstream distance. The

effect of the dense smoke in the boundary layer is again negligible as seen by little to no change in the boundary layer parameters of the slit/no smoke case vs. slit/smoke case.

		δ (cm)	δ* (cm)	θ (cm)	H
A	no slit/no smoke	4.45	0.64	0.46	1.42
	slit/no smoke	4.83	0.58	0.43	1.34
	slit/smoke	4.95	0.58	0.43	1.33
B	no slit/no smoke	6.22	0.79	0.58	1.36
	slit/no smoke	6.35	0.76	0.58	1.31
	slit/smoke	6.35	0.76	0.58	1.30

Table 5.2: Boundary layer parameters for the three cases at locations A and B

The effect of these variables on the large-scale structures in the boundary layer can also be observed by looking at the velocity POD modes with and without the slit and with and without the smoke. Figure 5.6 and Figure 5.7 show these modes at Locations A and B respectively, which are non-dimensional, normalized U velocity fluctuation fields. Qualitatively, the modes at location A (nearest the slit) are quite different. The first four modes show that the slit does have an effect on the velocity profiles, increasing the boundary layer and increasing the size of the structures in the flow. The location at A is the most impacted by the slit and its effect on the flow as shown in the first four modes in Figure 5.6.

Looking at Figure 5.7 and the modes further downstream (at location B), shows much similar features between the flow without the slit, with the slit but no smoke, and with the slit and smoke. They are similar with only slight modification in the shapes of the modes for the cases with and without the slit. The higher order modes similarly show small differences between the first two cases and no noticeable differences between cases 2 and 3. The differences in the shapes of the modes between the first two cases indicate that the slit causes the structures to be larger and further away from the wall, which is consistent with the notion of mass injection into the flow. Higher order modes and modes at other locations give the same general result and are not shown here for the sake of brevity, but can be found in the Appendix.

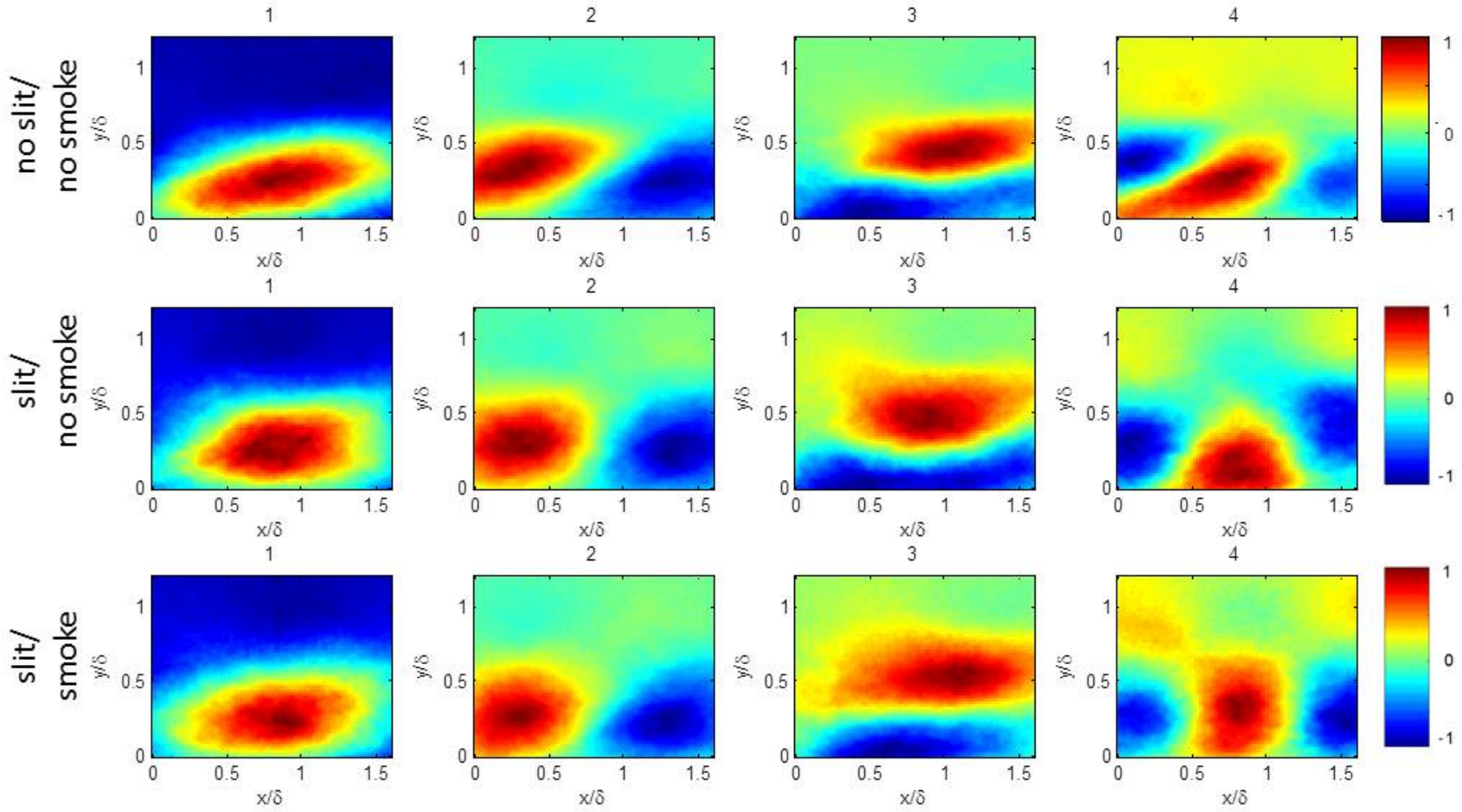

Figure 5.6: First four POD modes of non-dimensional streamwise velocity fluctuation at location A with a) slit covered, b) slit uncovered, but no smoke, and c) slit uncovered and smoke

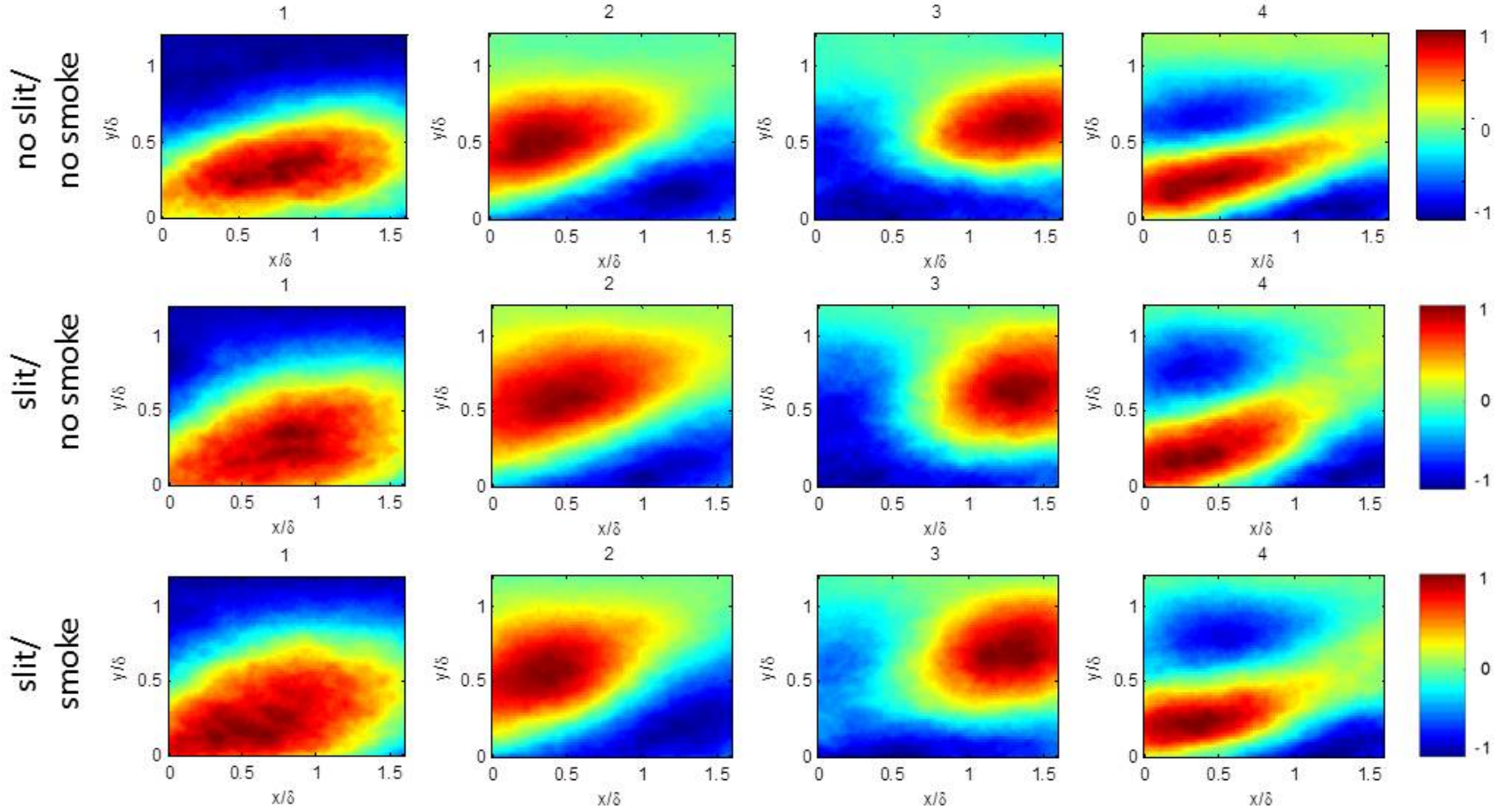

Figure 5.7: First four POD modes of non-dimensional streamwise velocity fluctuation at location B with a) slit covered, b) slit uncovered, but no smoke, and c) slit uncovered and smoke

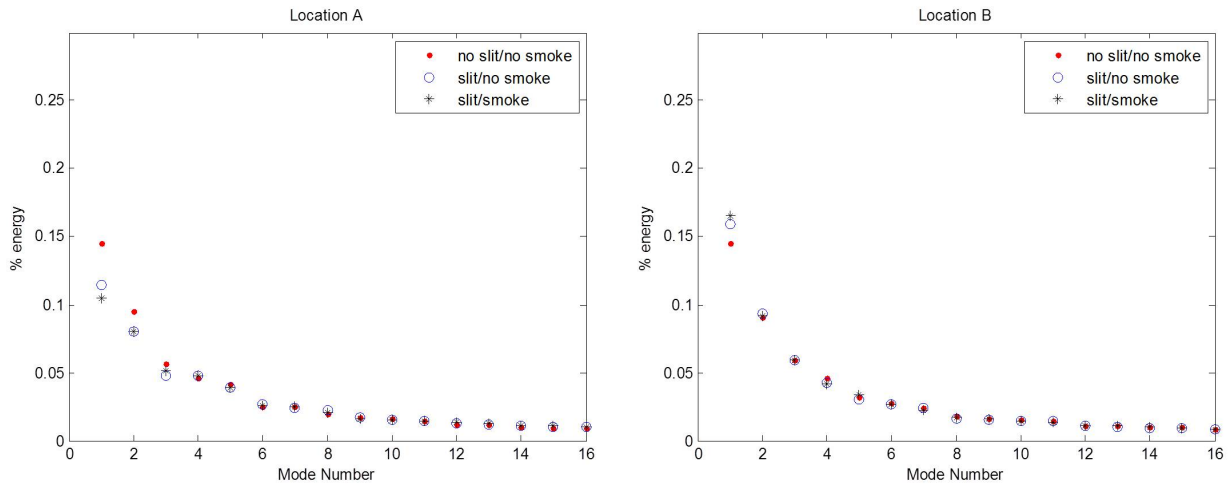

Figure 5.8: Percent of modal energy in the first 16 modes at location A and B for instances of slit covered, slit uncovered but no smoke, and slit uncovered and smoke

With respect to the energy content of the modes, there were small differences in the modal energy of the first three modes. The first two modes for the covered slit case had a slightly larger percentage of modal energy at location A than the slit/no smoke and slit/smoke cases. This can be seen in Figure 5.8 This difference decreased at Location B, and for both locations, the higher order modes showed negligible differences in energy. This effectively shows that the presence of the slit does alter the boundary layer by allowing mass to be swept in through the slit, but this effect is small and decreases with downstream distance. There are very minimal changes in the boundary layer due solely to the smoke being densely introduced into the boundary layer via the slit.

5.4.2 Boundary Layer Edge

To see how accurately the boundary layer edge identified using flow visualization images compares with the edge identified from velocity and vorticity fields, instantaneous snapshots of flow visualization, velocity deficit, and vorticity are compared in Figure 5.9 for cases at location B. Streamwise velocity deficit, δU, is defined as

$$\delta U = \frac{U_\infty - U}{U_\infty} \tag{5.1}$$

In addition, the vorticity, ω is calculated by

$$\omega = \frac{\delta v}{\delta x} - \frac{\delta u}{\delta y} \tag{5.2}$$

using the centered difference approach, and the units for vorticity are s^{-1}.

Upon inspection of the images it is apparent that the boundary layer edge from flow visualization corresponds favorably with the boundary layer edge from velocity and vorticity measurements. In this case, the boundary layer edge in velocity measurements is defined as 95% of the freestream velocity. A threshold for vorticity was set such that it neglected the obvious vorticity from noise of the velocity measurements.

The flow visualization does a good job in depicting the separation of the rotational flow from the irrotational freestream. The large scale shapes of the flow in the flow visualization images, velocity fields, and vorticity fields are comparable. In all the snapshots shown, and in others investigated, the boundary layer from flow visualization corresponds to the edge in velocity and vorticity, similar to the work of Holzner et al. on the turbulent front generated by an oscillating grid [66]. There was no distinguishable difference in this accuracy with respect to downstream distance, suggesting that the seeding of the boundary layer accurately depicts the outer edge of large-scale structures contained in the boundary layer and, at least over the distances considered here, is not affected by the history of structures that occurred upstream and have since died out. There were also no noticeable differences in the effect of the freestream velocity and the comparison of the boundary layer edge.

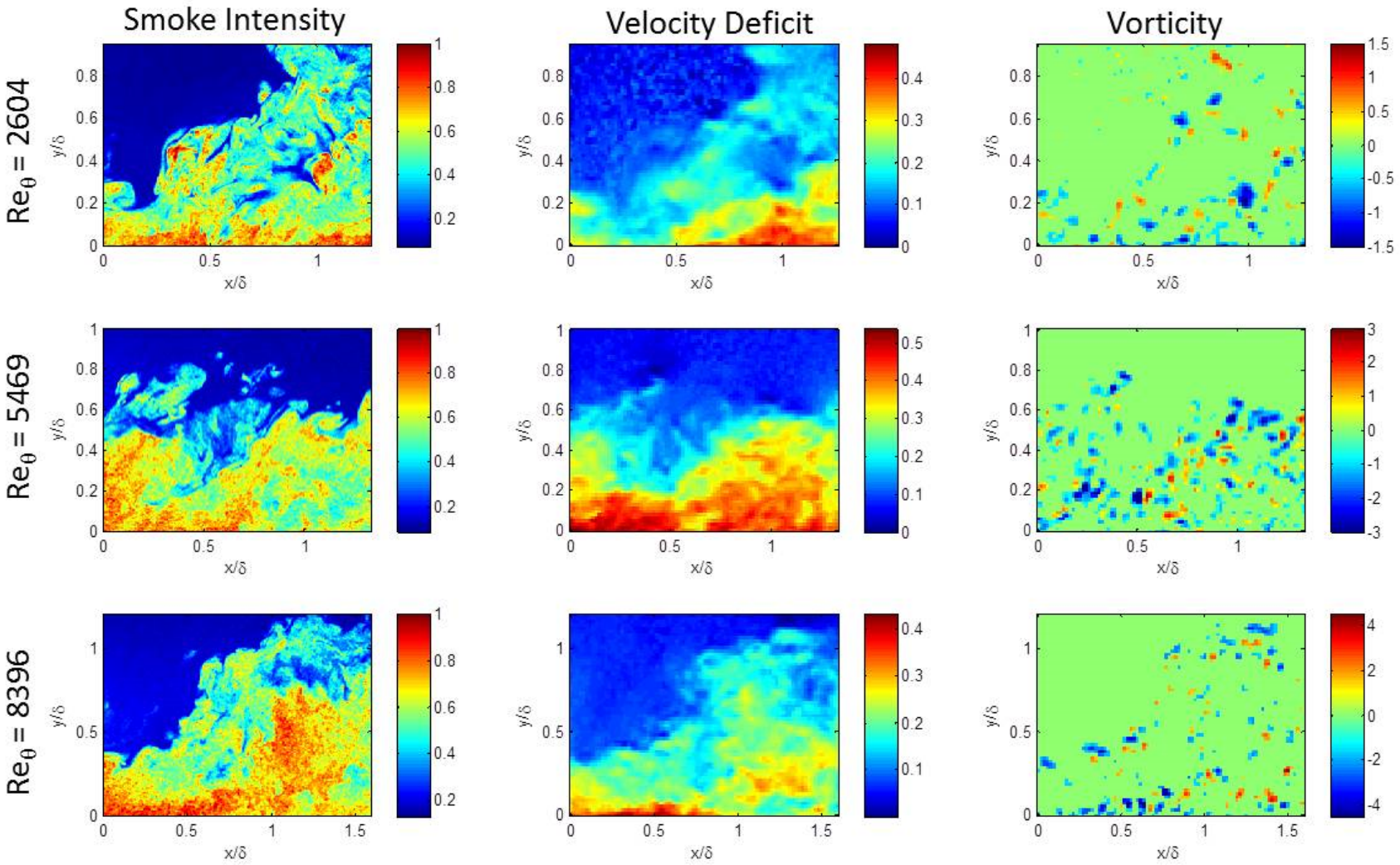

Figure 5.9: Examples of comparison of boundary layer edge in normalized smoke intensity, streamwise velocity deficit, and vorticity at location B at three different Reynolds numbers

The boundary layer edge in flow visualization images can be calculated using the method described in Prasad and Sreenivasan [53]. Figure 5.10 shows an example of the selection of the boundary layer edge. The inflection point of the thresholded average intensity as a function of the threshold can be detected and used as the demarcation line between the seeded boundary layer and the freestream flow. The boundary layer for this example in Figure 5.10 could be set at 0.23 of maximum intensity, and calculating the gradient of this graph can mathematically give an objective value to be used for the boundary layer edge.

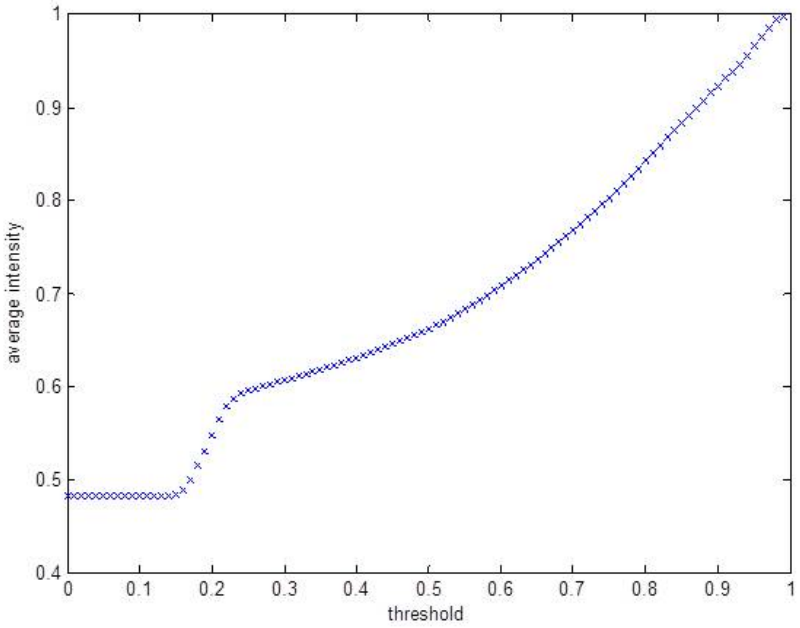

Figure 5.10: Thresholded average intensity as a function of the threshold

To further illustrate the ability of the boundary layer edge detection, Figure 5.11 displays the boundary layer edge of flow visualization at 23% of the maximum smoke intensity, and the boundary layer edge from velocity at 95% of the freestream velocity overlaid on the vorticity field. Both boundary layer edges and vorticity fields are similar in showing the upstream edge of the large scale motion. In this case, the boundary layer thickness varies from 0.4δ at the upstream (left) side of the image to 0.9δ at the downstream side of the image, which is evident by looking at flow visualization, velocity, or vorticity images. The turbulent bulge extends

over 0.7δ in the streamwise direction and beyond the field of view. The agreement between the boundary layer edge in flow visualization, velocity, and vorticity in this image and others further validates the ability of flow visualization to indicate size, shapes, and locations of turbulent bulges in the flow. The smaller features of the boundary layer, however, (0.1δ and under) are not in as much agreement between the different measurements. Thus flow visualization would not necessarily be appropriate to identify these smaller structures.

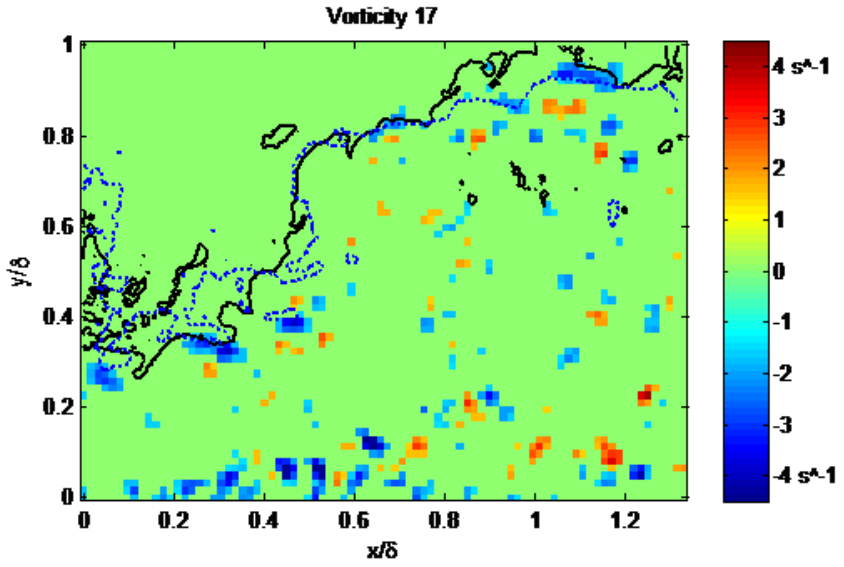

Figure 5.11: Velocity (blue dotted) and flow visualization (black) boundary layer edge overlaid on vorticity field

5.4.3 Smoke Intensity vs. Velocity

In seeking to determine how much information can be obtained from flow visualization images, it is important to investigate the correlation between flow visualization intensity and velocity measurements at the same instant. While there may not be a one to one correlation, the relationship between flow visualization and velocity is worth exploring further to determine what, if any, correlation may exist.

5.4.3.1 Direct Comparison

As a baseline to compare the complementary POD/LSE technique, a direct comparison of velocity to flow visualization (smoke intensity) is first calculated. To account for a slight non-uniformity of the laser sheet intensity in the streamwise direction of the image (perpendicular to the incident light), every pixel was normalized by multiplying each pixel with the ratio of the largest intensity value in its row (of the average image) divided by the average pixel value at that location. This increases the intensity toward the edges of the image, where the laser intensity was less than at the center of the laser sheet. For this direct comparison portion of these trials, the intensity images were further downsampled to 85 by 64, which is the same resolution as the interrogation areas for PIV images so that there could be a one to one comparison of intensity and velocity.

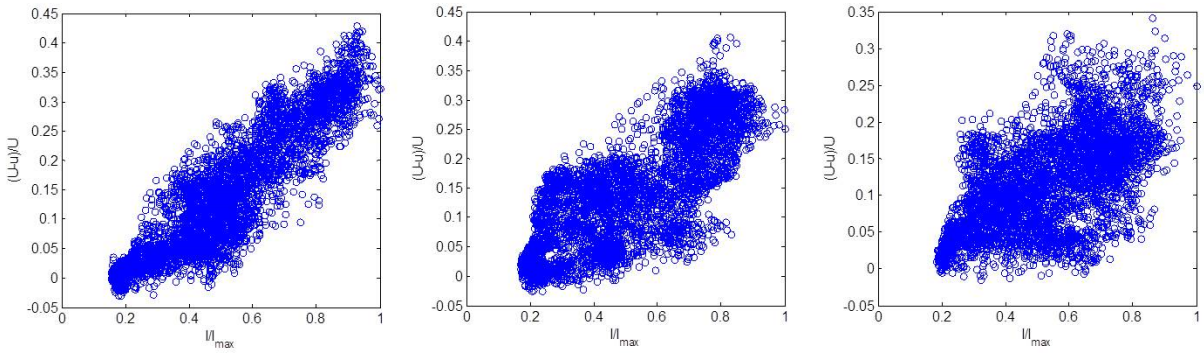

Figure 5.12: Examples of scatter plots of U velocity deficit vs. normalized smoke intensity at 3 different snapshots

Figure 5.12 shows scatter plots of the streamwise velocity deficit and image intensity for three different snapshots. Generally, higher image intensities are encountered closer to the wall, where lower speed fluid (higher velocity deficit) resides and in line with the notion that the smoke essentially serves as a marker for the low momentum fluid. In addition, lower speed fluid can potentially cause the smoke to coalesce, leading to further increases in image intensity. Conversely, lower image intensity is found away from the wall due to the presence and presumed mixing of unseeded free stream fluid into the boundary layer.

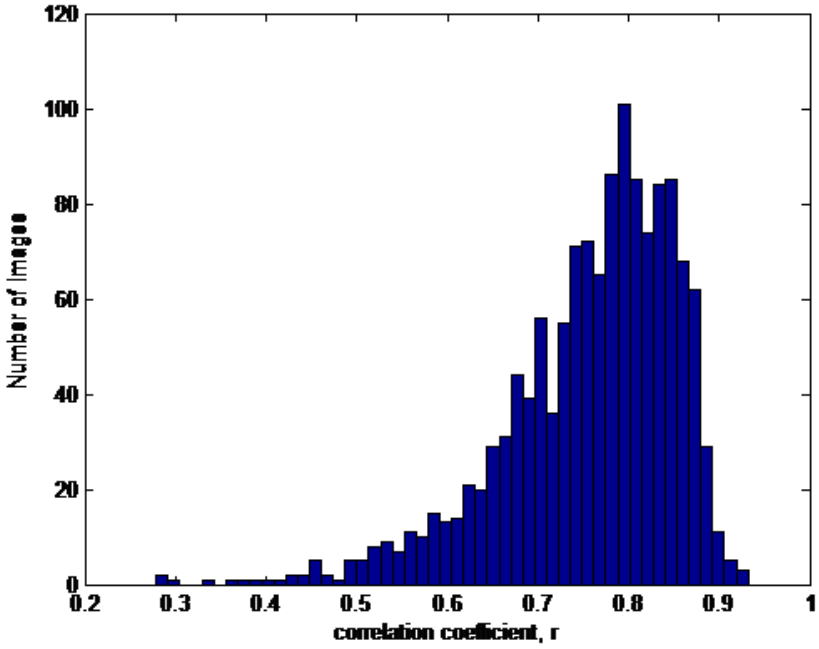

Figure 5.13: Histogram of correlation coefficients, r, for images at Location B, Re = 8396

For some images, such as the first plot shown in Figure 8, there is a relatively strong linear relationship between smoke intensity and streamwise velocity deficit. Most of the sequences were similar to the 2nd plot in Figure 5.12, with a linear relationship, but a significant width in the scatter plot. There were also a few instances where the relationship was not linear and there did not appear to be a strong correlation at all, as shown in the third plot.

The strength of this correlation can be quantified by calculating the correlation coefficient between the flow visualization image and the velocity image. The correlation coefficient, r, of the image intensity, I, and the velocity deficit, δU, is defined as the ratio of the covariance divided by the product of their standard deviations, or,

$$r(I, \delta U) = \frac{\sum_{i=1}^{n}[(I_i - \bar{I})(\delta U_i - \overline{\delta U})]}{\sqrt{\sum_{i=1}^{n}(I_i - \bar{I})^2 \sum_{i=1}^{n}(U_i - \overline{\delta U})^2}} \tag{5.3}$$

where n is the number of images in the trial, $\bar{I}$ is the average intensity image, and $\bar{U}$ is the average streamwise velocity component field. By subtracting out the average, the

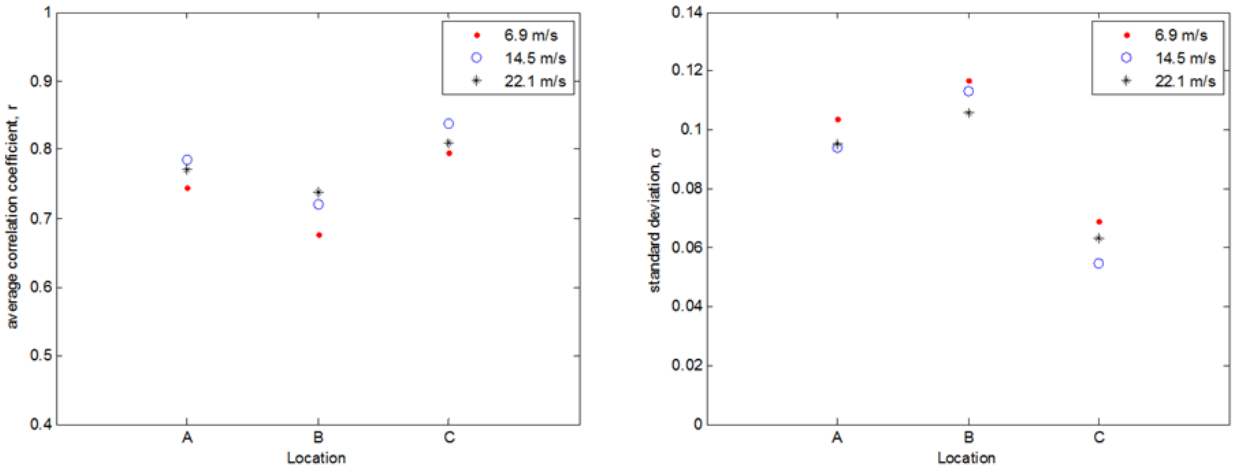

Figure 5.14: Average (left) and standard deviation (right) of correlation coefficients, r, of smoke intensity and streamwise velocity component

fluctuating components are investigated, therefore the correlation coefficient will be 1 or -1 if the two variables are perfectly correlated or perfectly anti-correlated, respectively. The coefficient will be zero if the two are not correlated at all. The correlation between each smoke intensity image and velocity deficit image for each trial is calculated, and a histogram of the correlation coefficients is shown for the case of the Re = 8,396 at location B in Figure 5.13. For this case, the average correlation coefficient is .757 and the standard deviation is .0971. For all nine cases, the average and standard deviation are shown in Figure 5.14.

The correlation coefficients range from about 0.7 to 0.84, with location B being least correlated for the three downstream distances. The standard deviation is also largest at location B. At this point, the cause of this drop in correlation and increase in standard deviation at location B is unknown. These correlations were calculated looking at the same field of view with reference to the local boundary thickness. The trials with the 6.9 m/s free stream velocity produced the smallest correlation coefficient averages and largest standard deviation.

For each of the nine trials (three different velocities at three different locations), all velocity measurements and intensity measurements were directly compared and a linear least squares best fit approximation was calculated for the data set. The relationship was

then used to take a flow visualization image (which was extracted and not used in the best fit calculation) and convert the smoke intensity to streamwise velocity measurements. This estimation of streamwise velocity measurements can be compared to the actual velocity measurements taken. Again, these estimates are not meant to imply that the velocity can be estimated strictly from flow visualization images, but as an exercise to quantify the relationship between the two and for comparison to POD/LSE estimations.

Qualitatively, the estimates can be compared to the actual velocity measurements. Part a of Figure 5.15 shows one example from each freestream velocity at location B. In general, the estimation of the boundary layer compared well to the actual boundary layer. Specifically, the shapes of the outer boundary layers were surprisingly similar to the shape in the actual velocity plots. The estimate tended to underestimate the peaks of the velocity deficit, but the overall, large-scale shapes of the outer boundary layer were similar in many cases.

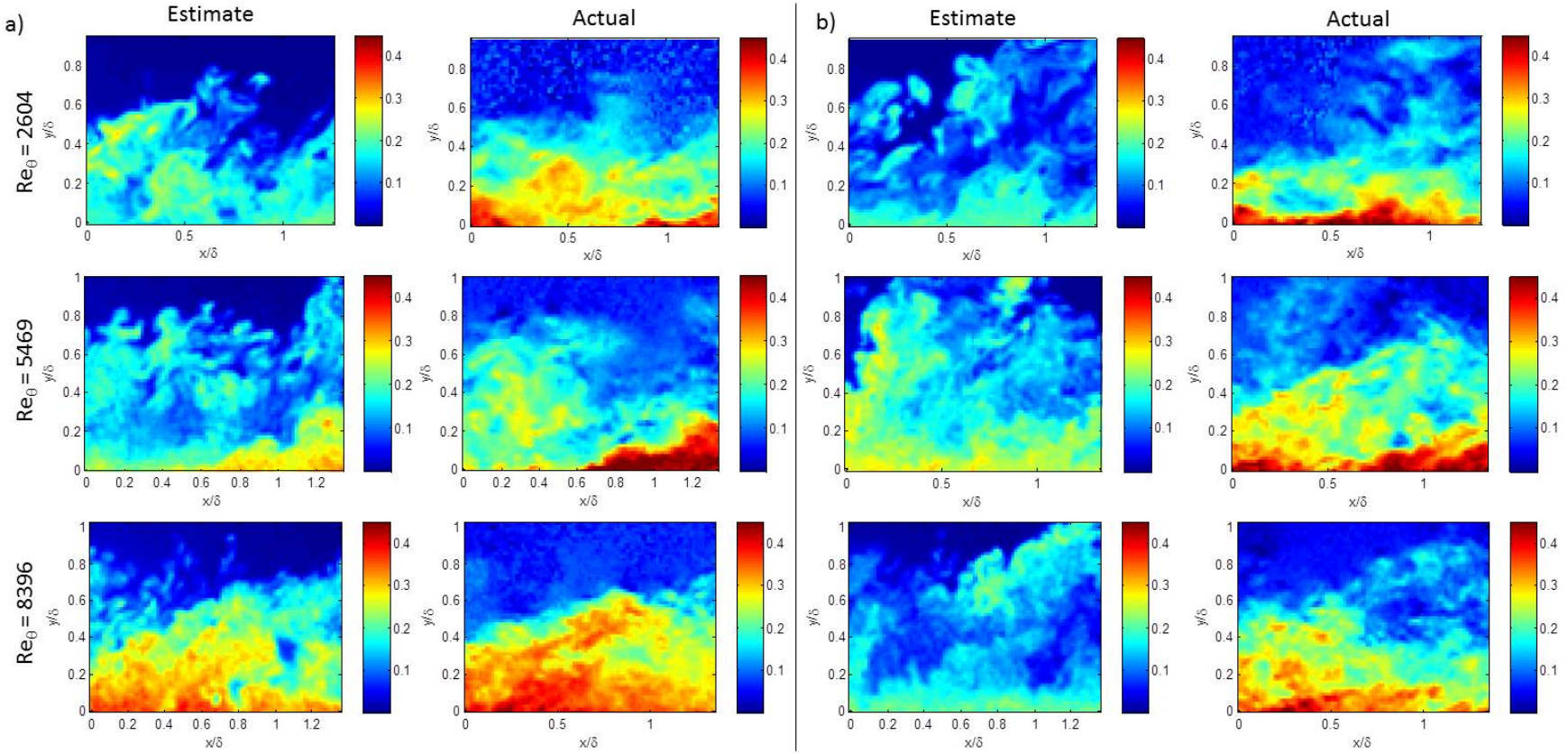

Figure 5.15: Examples of good estimates (a) and poor estimates (b) of streamwise velocity deficit compared to actual velocity deficit fields at Location B using direct correlation method of converting intensity to velocity

Looking closer at a few of these cases at location B shows that the image intensity reveals some relatively good estimates of the boundary layer structure. For the case of Re = 2,604 in Figure 5.15 part a, the boundary layer edge on the left side of the estimated image is similar, but slightly higher than the actual velocity deficit. The protrusion in the middle of the image is shown in the estimate and is faintly detected in the actual velocity deficit. The sloping boundary layer edge on the right side of the estimate and actual image are nearly identical. For the case of Re = 5,469 in part a, the first noticeable similarity is the low speed fluid at the bottom right captured by both images. The boundary layer edge deviates slightly from the estimate and actual, but both show a large structure on the left side, about 0.8δ in height that drops down toward the middle right of the image. The estimated view shows the boundary layer rising toward 1δ at the right edge of the image, which is not as apparent in the actual velocity field, though can faintly be seen. For the trial with a Re = 8,396 in part a, the estimated and actual boundary layers show a large inclined structure rising from 0.4δ at the left side of the image to 0.8δ at the right. Figure 5.15 part a shows just one example from each location each velocity, but the estimations at all three velocities and all three locations were comparable to these shown in Figure 5.15.

Part b of Figure 5.15 shows cases where the estimated velocity did *not* show similar features to the actual velocity indicating that deviations are possible, although not overly common. These were instances where the estimation and actual velocity deficit plot did not match well. They were generally occasions where the outer portion of the boundary layer consisted of very high intensity smoke which did not correlate to low velocities. Estimations at all three locations and all three velocities similarly showed instances where the estimations were inaccurate. Comparisons of smoke intensity with wall-normal velocity, velocity magnitude, and vorticity were also investigated with no relationship found. In addition, intensity gradients were used for correlation with no relationship found between the gradients and any velocity or vorticity measurements.

5.4.3.2 Complementary POD/LSE Results

In seeking to determine how much information can be obtained from flow visualization images, the correlation between flow visualization intensity and velocity measurements at the same instant were investigated further by considering the POD modes generated for each data set. As the POD modes represent the most energetic structures of each set, it is an interesting exercise to see how well the activity of the most energetic modes correlate when comparing intensity to velocity data.

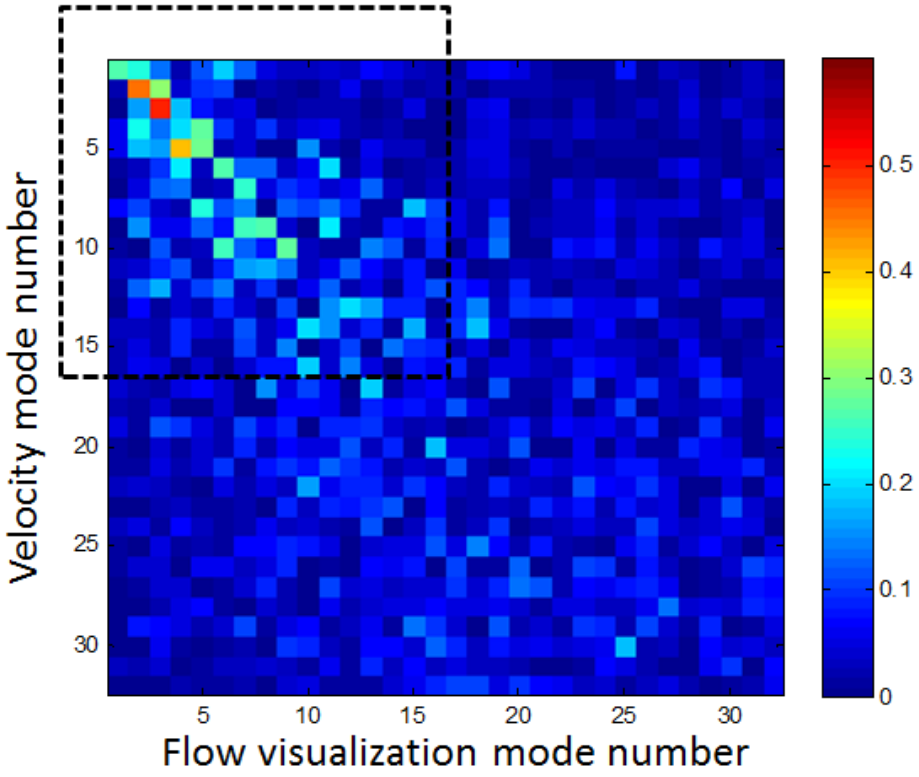

Figure 5.16: Correlation coefficients of 32 velocity and flow visualization modes

Figure 5.16 shows the correlation between the POD time coefficients for each set. The time coefficient represents the degree to which a particular mode is present at any given instant in time. As can be seen, there is a strong correlation in the appearance of the most energetic intensity modes and the most energetic velocity modes with correlation coefficient values as high as 0.6. At higher mode numbers, the correlation drops significantly indicating

that the relationship between velocity and intensity is constrained to only the most energetic (largest spatial scales) modes and does not extend to the small scale structure.

Using the linear stochastic estimation with the correlation values of each of the modes, a flow visualization image can be converted to an estimated velocity field. The flow visualization image is projected onto the flow visualization modes to calculate the time coefficients. These coefficients are then converted to velocity mode coefficients via the correlation matrix, L_{ij}, using equation 3.3 in chapter 3. The new velocity coefficients are then applied to the velocity modes and summed to calculate the approximated velocity deficit field. This procedure is similar to the direct estimation procedure described earlier; however, through the POD/LSE technique, only the portion of the signal that is correlated is used to obtain the estimation. Figure 5.17 shows several examples for location B. These are examples from images which were not used in the initial POD and correlation measurements.

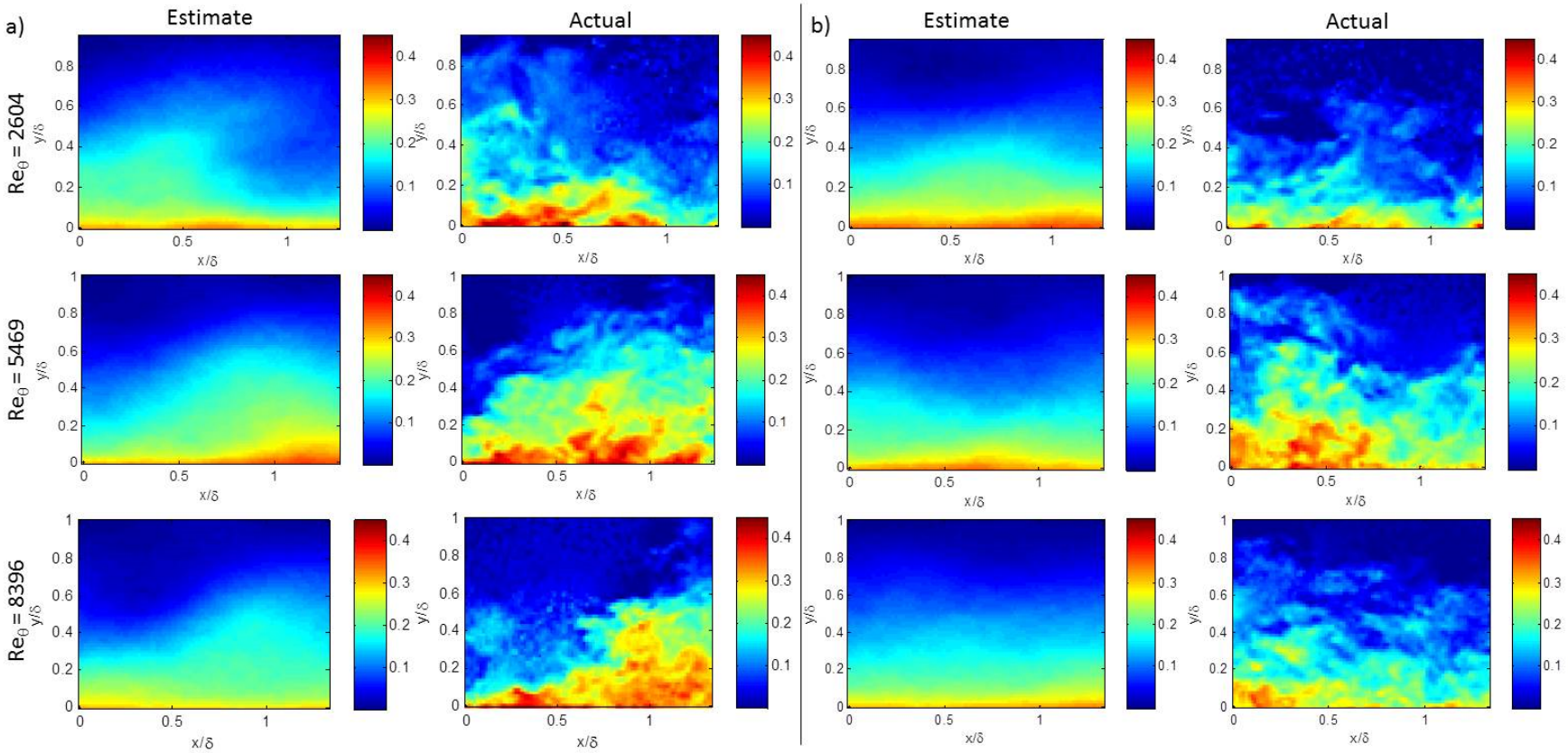

Figure 5.17: Examples of good estimates (a) and poor estimates (b) compared to actual U velocity deficit fields at Location B using complementary POD/LSE approach

Immediately apparent is that the smaller scale motions and structures are filtered because only the first 16 modes were used in correlation and reconstruction. This is consistent with the earlier observations that while the smoke effectively marks the large-scale, low momentum regions of the flow, it does not effectively mark the small-scale structure of the flow. Overall, there are some similarities in the estimations compared to the actual velocities. For the example from the trial with a freestream velocity of 6.9 m/s in part a, the estimated velocity shows a higher edge on the left of the image, sloping downward on the right. This is similar to the actual velocity, but the actual shows much more details in the boundary layer.

For the two trials at higher velocities, the estimated and actual depict a smaller structure on the right half of the image rising to about 0.6δ in height. In many cases, like examples in part a, the overall shape of the boundary layer and large scale structures in the velocity estimation matches well with the actual velocity. However, there are also instances where the estimations are not similar to the actual velocity fields. To emphasize that not all estimations followed the actual velocity field, some examples of poor estimations are shown in part b of Figure 5.17. The cases where the actual boundary layer is especially convoluted do not give very good estimates from the POD/LSE technique.

The effectiveness of the POD/LSE technique for velocity estimation can be compared to the direct correlation technique by looking at the correlation between estimated and actual velocity deficit fields. Figure 5.18 shows higher correlation values for the POD/LSE technique, especially at locations B and C. The complementary POD/LSE technique filters out the small scale features, whereas the direct approach attempts to keep them, many times inaccurately, leading to the higher correlation values for the former technique. Particularly interesting is the trend of increasing correlation with downstream distance, which seems to indicate that the effectiveness of smoke of marking the large-scale, low momentum regions improves with time, in contrast to the notion that history effects render the smoke meaningless.

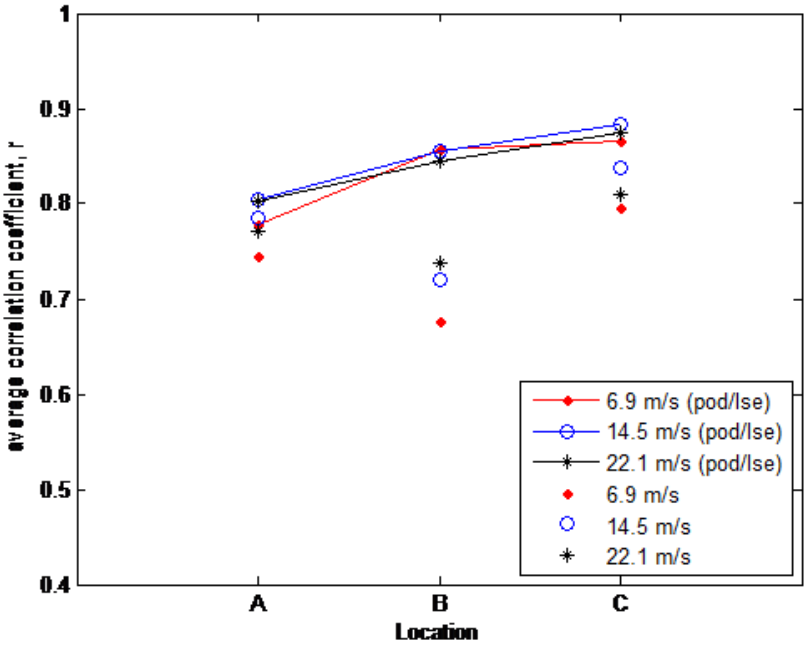

Figure 5.18: Average correlation of estimated and actual velocity fields from the POD/LSE technique and direct approach

An important concern is the possibility that the POD/LSE technique has higher correlation values due to simply smoothing out the smaller scale features. However, applying a mean smoothing filter to the original flow visualization image increases the correlation coefficients by only 0.7% to 1.1%. The largest correlation coefficients were found using a 32 by 32 filter on the original image. In addition, smoothing the velocity vectors in conjunction with smoothing the flow visualization images increased the correlation coefficients by 0.9% to 1.4%. Therefore, the increase in the correlation coefficients with the POD/LSE approach due to more than just a consequence of filtering the data to remove the smaller features in the flow.

5.5 Discussion

The turbulent boundary layer tripped by sand paper on the wind tunnel wall was investigated at three downstream locations and at three different freestream velocities. The

boundary layer was seeded in such a way that PIV could be performed on the entire image, but the delineation from boundary layer and freestream could be ascertained for flow visualization.

Seeding the boundary layer via a slit is a widely used method for flow visualization trials; however, the effect of the seeding on the boundary layer structures is usually not discussed. Trials were performed with and without the slit covered (and no smoke coming in through the slit) and velocity measurements were compared at the first two locations. The turbulent boundary layer thickness increased by 8.6% and 2.0% at locations A and B respectively due to the air being passively swept into the boundary layer via the slit. Other boundary layer parameters were slightly affected. As downstream distance increased, the effect of the slit on the boundary layer decreased. Furthermore, there seemed to be little or no effect of the slit on the first few POD modes, which represent the larger and most repeatable structures in the turbulent boundary layer.

With the slit uncovered, trials were run with and without smoke entering the boundary layer via the slit. This was performed to test the seeding and PIV processing to investigate whether the smoke affects the velocity measurements. There were no differences in the boundary layer profiles, boundary layer parameters, and POD modes when the smoke was allowed to be swept into the boundary layer.

To see how accurately the boundary layer for flow visualization compares with the boundary layer velocity and vorticity fields, instantaneous snapshots of vorticity, velocity deficit and flow visualization were compared for all 9 cases. In all cases, the boundary layer edge from flow visualization does correspond favorably with the boundary layer edge from velocity deficit and vorticity measurements. There were no noticeable differences at differing velocities or downstream distances.

Direct comparison of velocity and smoke intensity showed a correlation of higher intensity smoke to lower velocity fluid. The average correlation coefficient was between 0.68 and 0.84 for the cases. Using this linear relationship to estimate the velocity deficit field from a

flow visualization image (as an exercise to further delve into this relationship), the estimates show many of the same features and boundary layer shapes in most instances. There were, of course, cases where the estimations did not match the actual velocity fields.

Proper orthogonal decomposition modes of velocity and intensity modes were correlated. Those correlations were used with linear stochastic estimation to estimate a velocity field given a flow visualization image. These estimations showed some similar characteristics to the actual velocity, but all small scale features were washed out of the reconstructions.

Overall, the trials showed that smoke effectively marks the low-momentum region of the flow and delineates the edge of the boundary layer. Both direct correlation and POD/LSE results clearly establish this relationship but confine it to only the largest scale features. Surprisingly, there is little evidence of any history effects affecting this relationship. In fact, the POD/LSE results appear to show the relationship improving with downstream distance. Therefore, seeding smoke through a slit can be considered as a relevant approach for visualization of the largest scales and features of the flow. However, significant caution should be exercised when using images such as this to infer smaller scale features or details about the underlying flow. Thus, PIV and other inherently quantitative techniques should be the first choice, but if prohibitive, flow visualization is a viable tool.

Chapter 6

Comparison of Large Scale 3-D Features in Zero and Adverse Pressure Gradient Turbulent Boundary Layers

6.1 Introduction

Coherent motions in turbulent boundary layers have received considerable attention in the field of fluid dynamics. The understanding of the three-dimensional dynamics of these organized structures in an adverse pressure gradient is relevant as researchers attempt to model, predict, and control wall-bounded flows. Decades of research has led to a basic picture of the canonical ZPG turbulent boundary layer, but the structures in turbulent boundary layers on the verge of separation are less well defined. Though many engineering applications such as helicopter blades, turbines, ships, and aircraft experience APG turbulent boundary layer flow, historically, this has been considered one of the most difficult flows to predict with turbulent models [30].

This chapter examines the large scale motions under three different pressure gradients using 3-D flow visualization. In using a scanning, 3-D flow visualization technique, this work avoids the drawbacks associated with characterizing three-dimensional features based on only 1-D or 2-D measurements.

Historically, 2-D flow visualization of a turbulent boundary layer using the intensity of light scattered from smoke seeded into the flow has served a very important role in examining the large-scale structures. Important flow visualization studies such as those of Praturi and Brodkey [45], Head and Bandyopadhyay [13], and Smits and Delo [46], just to name a few, have uncovered characteristics of the structures, which led to more quantitative, follow-up measurements.

In the previous chapter, simultaneously applied 2-D flow visualization and 2-D PIV was used to explore the relationship between qualitative flow visualization images and quantitative planar velocity data [67] in a turbulent boundary layer similar to the work in this chapter. This showed that while flow visualization may obscure some of the small scale features of the flow, it is effective in identifying the large scale features in the flow, in particular, the boundary layer edge, and is thus suitable for characterizing large scale features in the boundary layers in situations where PIV is not possible or practical. The experiments performed in this chapter take advantage of these findings and use 3-D flow visualization to study the 3-D characteristics of large scale structures contained in ZPG and APG boundary layers. The approach is comparable to the work of Delo and Smits [20] and Smits and Delo [46] who use a similar technique to investigate structures in a ZPG turbulent boundary layer.

In general, there is a scarcity of information about the 3-D characteristics of large scale structures and their organization in adverse pressure gradient turbulent boundary layers. This chapter contributes to the understanding of these structures by reporting 3-D flow visualization measurements made in a zero pressure gradient and two adverse pressure gradient turbulent boundary layers (β=8.1 and β=9.7). Observations about the boundary layer structures are made by investigating the instantaneous flow visualization volumes, the power spectral density of the volumes, the features from binary image slices, and conditionally averaged volumes around a structure for these Reynolds numbers, Re_θ, between 7400 and 8400. The investigation of these structures has not been previously performed for these adverse pressure gradients or for the large 3-D field of view (3.4δ by 4.3δ by $.5\delta$) as is done in this chapter.

6.2 Experimental Arrangement

6.2.1 Facility and Particle Seeding

All experiments were conducted in Auburn University's 0.6 m x 0.6 m wind tunnel. It is an open circuit, blow-down wind tunnel, with a 2.4 m long test section and a maximum

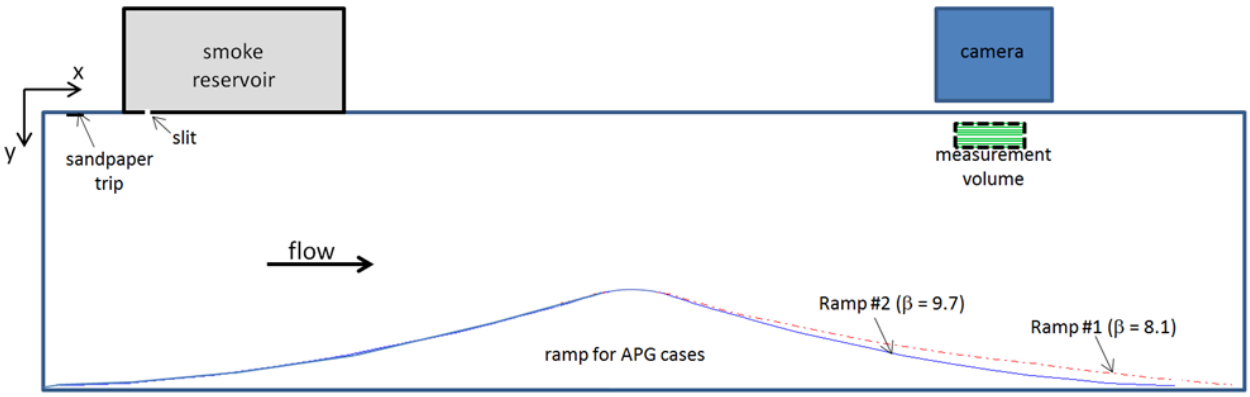

Figure 6.1: Schematic of experimental setup side view (not drawn to scale)

speed of 30 m/s. A square contraction of 2.5 to 1 with a length of 1.8 m is used to accelerate the flow to the test section. Preceding the test section are stainless steel honeycomb and three screens of 80% porosity to condition the flow and to create a uniform velocity across the test section.

For this experiment the boundary layer formed on the top wall of the wind tunnel was investigated. The flow on the wall was tripped to a turbulent flow by a strip of k-type roughness elements approximately 1 to 2 mm high. The strip was 38 mm long in the streamwise direction and covered 0.46 m or about 75% of the spanwise length of the test section. Smoke was introduced through a slit in the top of the wind tunnel 0.3 m downstream of the slit, as shown in Figure 1. Smoke was produced using a ViCount Compact 1300 oil-based smoke generator that produces particles 0.2-0.3 micrometers in size. The slit was 3 mm in the streamwise dimension and spanned 75% of the spanwise length of the test section. The smoke traveled along the top of the tunnel 132 cm downstream to the measurement location. The average boundary layer thickness at this location was approximately 50 to 56 mm for the boundary layers investigated in this experiment depending on the pressure gradient. Figure 6.1 illustrates the experimental setup in which x is the streamwise direction, y is the wall-normal direction, and z is the spanwise direction.

6.2.2 3-D Flow Visualization Technique

The main piece of instrumentation used in this technique is a pulse burst laser system built in-house capable of producing laser pulses at repetition rates in excess of 1 MHz over a 1 msec long window. An in depth discussion of this flow visualization technique can be found in Thurow and Lynch [68]. Recently, additional amplifier stages have been added to the system such that, for this experiment, the laser energy is greater than 50 mJ for each pulse in the burst. See Thurow et al. (2013) for a review of applications of these ultra-high repetition rate lasers [69]. For 3-D flow visualization, a burst of 14 laser pulses was produced at 1 MHz repetition rate and deflected off of a 6 mm aperture galvanometric scanning mirror. A long focal length spherical lens and a cylindrical lens located in front of the scanning mirror were used to form an approximately 1 mm thick laser sheet whose position is determined by the momentary angle of the scanning mirror.

The high-speed camera, detailed later, was mounted directly above the tunnel, and a mirror was used to view the streamwise-spanwise planes of the illuminated boundary layer. Figure 6.2 shows the downstream view of the experiment (with the flow normal to the page). The laser was directed from the side of the tunnel and scanned from bottom to top to capture the 2-D planes which were reconstructed to a 3-D visualization. The field of view used in this case was 1284 pixels by 1636 pixels in the streamwise and spanwise directions, respectively, which correspond to 3.4δ by 4.3δ The distance from the scanning mirror to the field of view was 1.93 meters. The scan in the wall-normal direction consisted of 14 slices and scanned a distance of 25 mm from the tunnel wall to 63 mm in the wall normal direction capturing approximately 0.5δ to 1.2δ of the boundary layer for the velocities in this experiment. The angular variation between each slice is .0012 radians. Images closer to the wall were not acquired as they would have been nearly uniformly seeded with smoke and not offer significant contrast between the seeded boundary layer flow and unseeded freestream.

Images were acquired for each successive laser pulse using a Cordin gated intensified CCD framing camera. The camera is capable of acquiring up to 16 images with 2,048 x

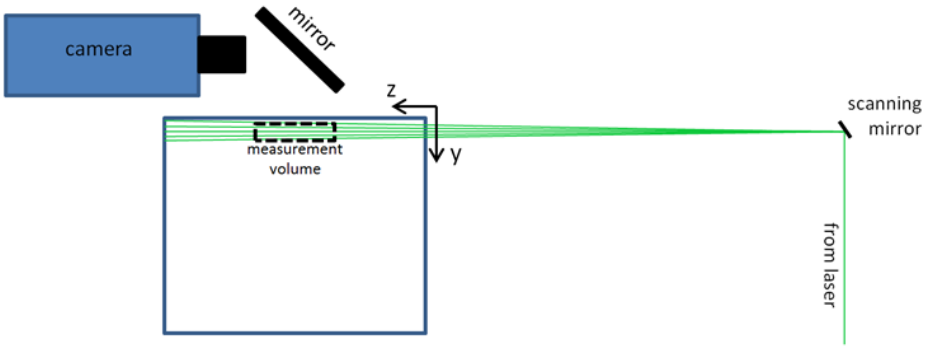

Figure 6.2: Schematic of experimental setup (downstream view)

2,048 pixel resolution at framing rates up 40MHz. The framing rate was set to 1 MHz such that, for this trial, a sequence of 14 images was acquired in 14 microseconds. The movement of the flow field between the first and last image was negligible (on the order of a maximum of three pixels).

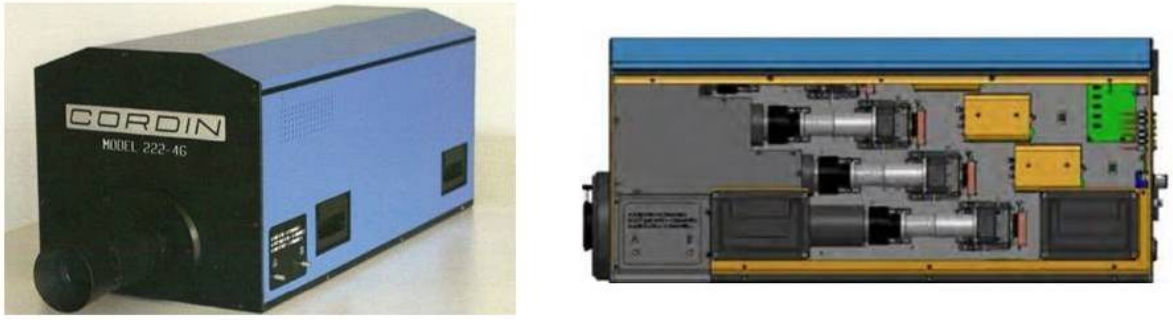

Figure 6.3: Cordin Camera

6.2.3 Adverse Pressure Gradient Ramps

Following the method outlined by Stratford [70], a ramp was fabricated that created an adverse pressure gradient with a boundary layer close to separation. A Stratford ramp produces an adverse pressure gradient that causes minimum shear stress over the pressure recovery area region and thus allows for a maximum pressure recovery over a minimum length at which the flow is on the verge of separation at all points. The profiles of the

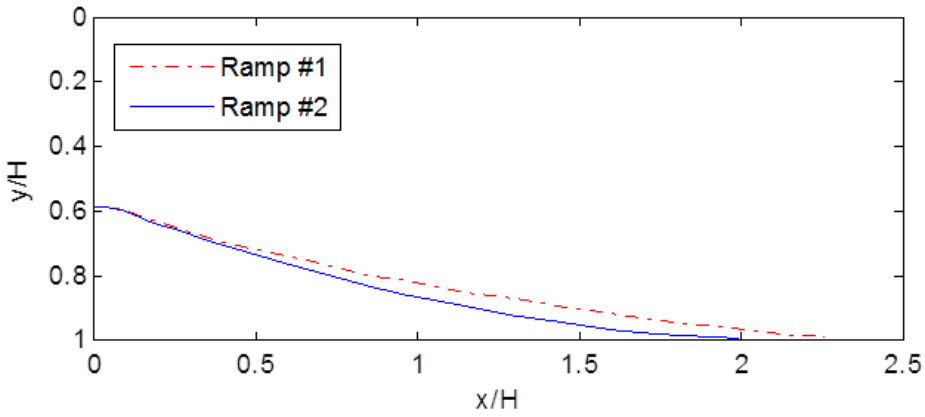

Figure 6.4: Profile of adverse pressure gradient ramps

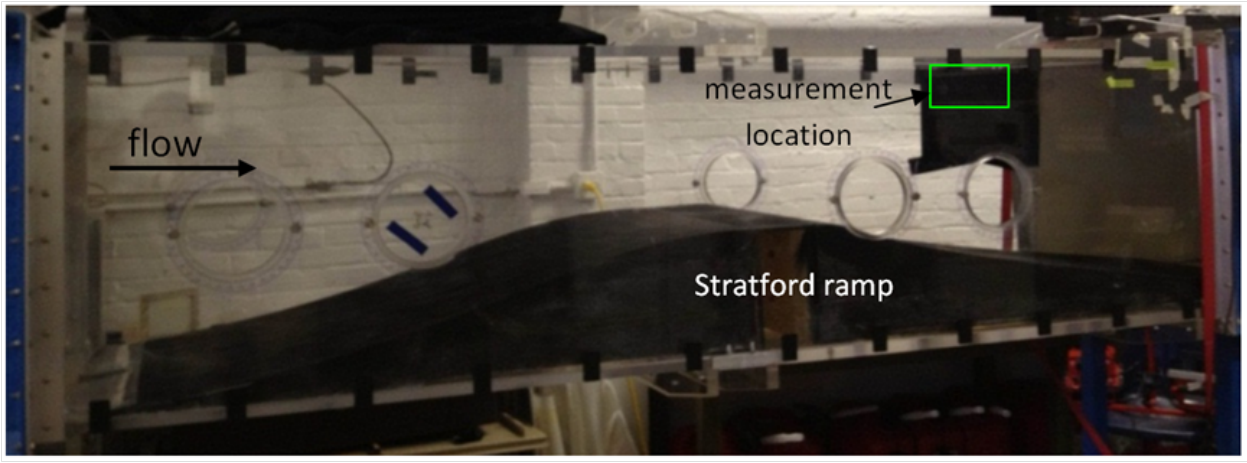

Figure 6.5: Photograph of ramp installed in wind tunnel

adverse pressure gradient ramps are shown in Figure 6.4. A parabolic favorable pressure gradient ramp precedes the adverse pressure gradient ramps. A 127 mm flat section joins the two ramps.

For all trials described in this chapter, the turbulent flow at the measurement location was fully attached. Careful observation of smoke visualization and velocity measurements showed no signs of back flow. No intermittent transitory detachment (back flow 20% of the time) or even incipient detachment (back flow 1% of the time) as described by Simpson [44] was found to occur in the flow produced by the APG ramps for the velocities measured for this experiment. The ramps installed in the wind tunnel are shown in Figure 6.5.

6.3 Flow Visualization Image Processing

Each nearly instantaneous flow visualization volume consists of 14 independent images, each representing a different streamwise-spanwise slice through the flow. Several image processing steps are applied to each image in a sequence. First, a dark background image is subtracted to minimize any background signal and to mitigate the effect of a few hot pixels. Next, the average frame-to-frame image intensity fluctuation is corrected to normalize the nominal image intensity in each of the 14 images. In addition, a time averaged image is also used to correct for a streamwise variation in image intensity associated with the non-uniform illumination of the laser sheet. Lastly, the images are smoothed with a 9 x 9 moving average filter, which reduces the influence of high spatial frequency noise associated with the camera's image intensifiers.

The boundary layer edge in flow visualization images was found objectively by using the technique proposed by Prasad and Sreenivasan [53]. In this technique, the inflection point of the average smoke intensity above a set threshold is calculated and used to define the edge between seeded low-momentum boundary layer fluid and the unseeded free stream. This effectively marks the instantaneous edge of the boundary layer as has been demonstrated in the previous chapters [67]. The images were then converted to binary so that the intensity inside the boundary layer was set to one and outside the boundary layer was set to zero. The full intensity images and binary images were both used for most of the investigative techniques described in the paper. Figure 6.6 shows an example of the original images from the high speed camera at different wall-normal heights and the binary images after smoothing and boundary layer edge detection.

Figure 6.7 shows a sample 3-D flow visualization volume with dimensions and an overhead view of the same instance. In this figure, Tecplot software was used to fit and visualize an iso-surface located at the boundary layer edge with shading used to indicate the wall-normal height of the boundary layer edge.

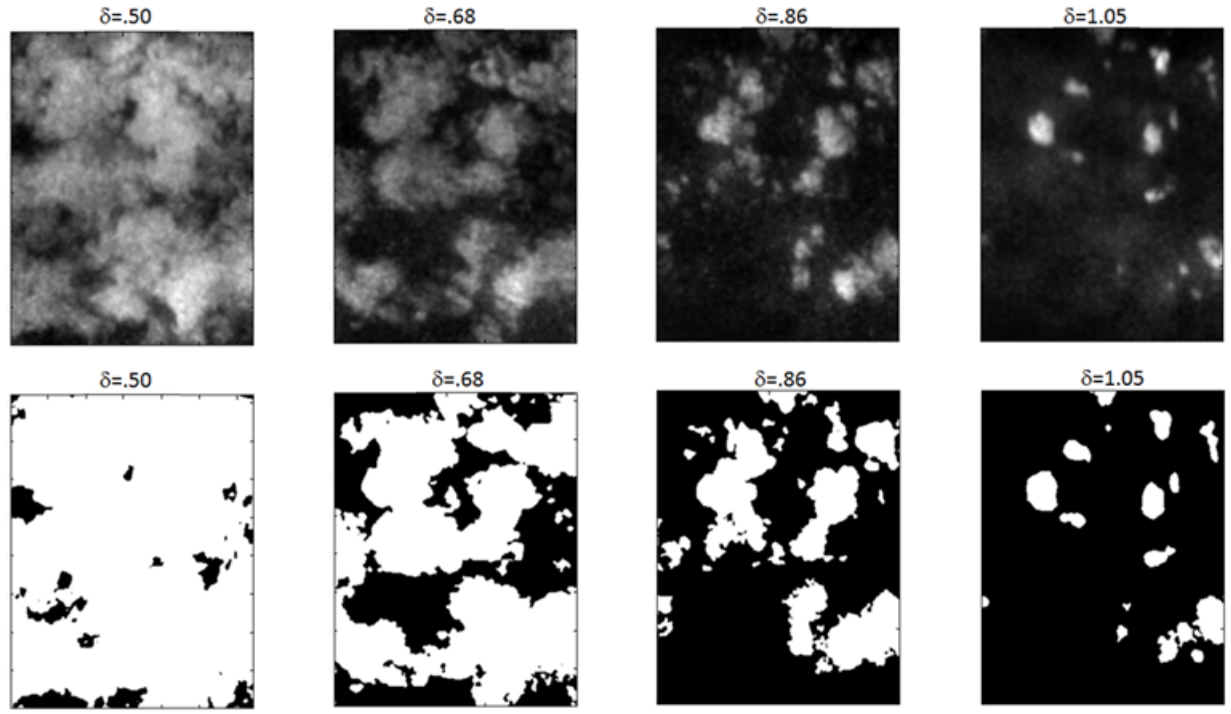

Figure 6.6: Original intensity images and binary images after boundary layer edge detection for the $\beta = 0$ case. Flow is from left to right. Shown are 4 out of the 14 slices

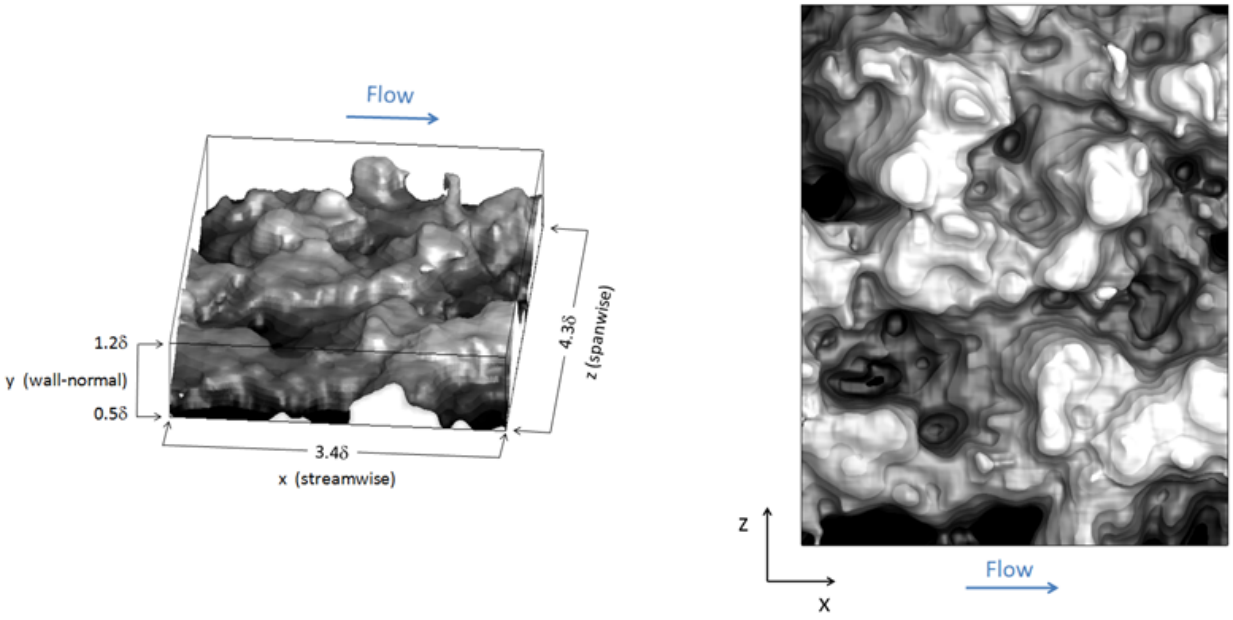

Figure 6.7: Orthogonal and overhead view of an example 3-D flow visualization for the $\beta = 0$ case

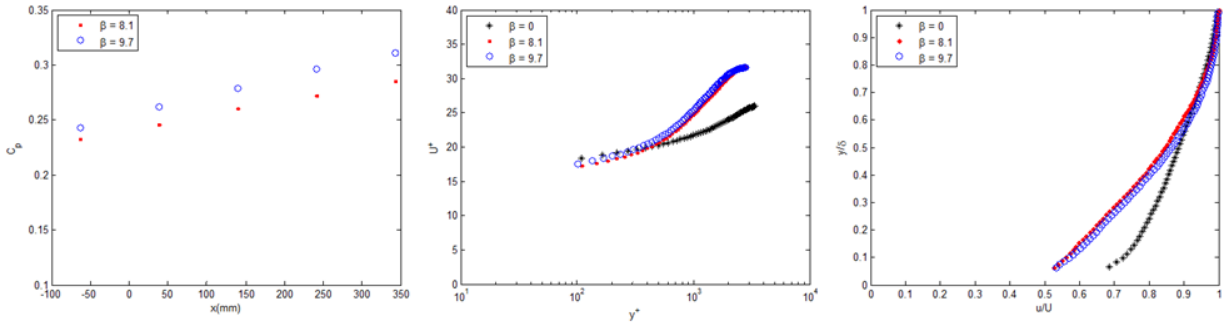

Figure 6.8: Canonical pressure coefficients, boundary layer profiles normalized with inner parameters, and boundary layer profiles normalized with outer parameters

6.4 Boundary Layer Parameters

Two-dimensional particle image velocimetry was performed to calculate the boundary layer parameters for the three different cases presented in this chapter. First, a trial was performed without any ramp in the wind tunnel for a zero pressure gradient case. Then, trials were run with two adverse pressure gradient ramps. The velocities for the three cases were adjusted to give comparable Reynolds numbers based on momentum thickness, Reθ. Calculated from the velocity profiles, the average boundary layer thickness, δ, displacement thickness, δ, momentum thickness, θ, and shape factor, H, are displayed in Table 6.1.

	U(m/s)	δ(mm)	δ* (mm)	θ(mm)	H	Re_θ	β
No ramp	18.6	55.9	7.92	6.02	1.32	8380	0
Ramp # 1	20.8	51.5	8.41	4.90	1.72	7610	8.1
Ramp # 2	21.0	52.1	8.61	4.72	1.82	7420	9.7

Table 6.1: Boundary layer parameters

The friction velocity, v*, and wall shear stress, τ_w, are calculated using the technique described by Kendall and Koochesfahani of fitting the data points to the Spalding profile in the log region of the boundary layer [65]. The friction velocities for the first and second APG ramp trials were 0.30 m/s and 0.28 m/s respectively. Pressure measurements were taken from static pressure ports at the top tunnel wall (at the measurement locations) spaced 101.6 mm in the streamwise direction. The pressure measurements were sampled for 0.5 seconds at a

rate of 1 kHz and averaged over 7 trials using a manometer calibration. Using the wall shear stress and pressure measurements from static pressure ports on the top of the wind tunnel wall, the equilibrium pressure gradient parameter, β, can be found. As described by Clauser [38],

$$\beta = \left(\frac{\delta*}{\tau_w}\right)\left(\frac{dP_\infty}{dx}\right) \tag{6.1}$$

For the first APG trial, the average pressure gradient across the field of view was 103.9 Pa/m, which corresponds to a β of 8.2, generally considered to be a moderate to strong adverse pressure gradient. With a similar exerimental arrangement, Aubertine and Eaton [71] investigated a mild APG boundary layer with a value of $\beta = 2.5$. The steeper adverse pressure gradient ramp produced a flow with an average pressure gradient of 129.1 Pa/m or a value of $\beta = 9.7$ for the velocity measured in the third trial.

6.5 Results

For each of the three cases (β= 0, β= 8.1, β= 9.7), 488 instantaneous volumes of the smoke intensity of the turbulent boundary layer were captured. Three-dimensional flow visualizations were reconstructed for each of the snapshots for all three trials. The 3-D flow visualization images, power spectral density, binary images, and conditionally averaged features were investigated and compared for the three different pressure gradients.

6.5.1 Flow Visualization Images

A few observations can be made through direct examination of the instantaneous flow visualization images in 2-D and in 3-D (Figure 6.9 and Figure 6.10). Figure 6.9 shows an example of an orthogonal view from each of the three trials that give a general indication of the structures found in each of the cases. Flow is from left to right with dimensions indicated in the figure.

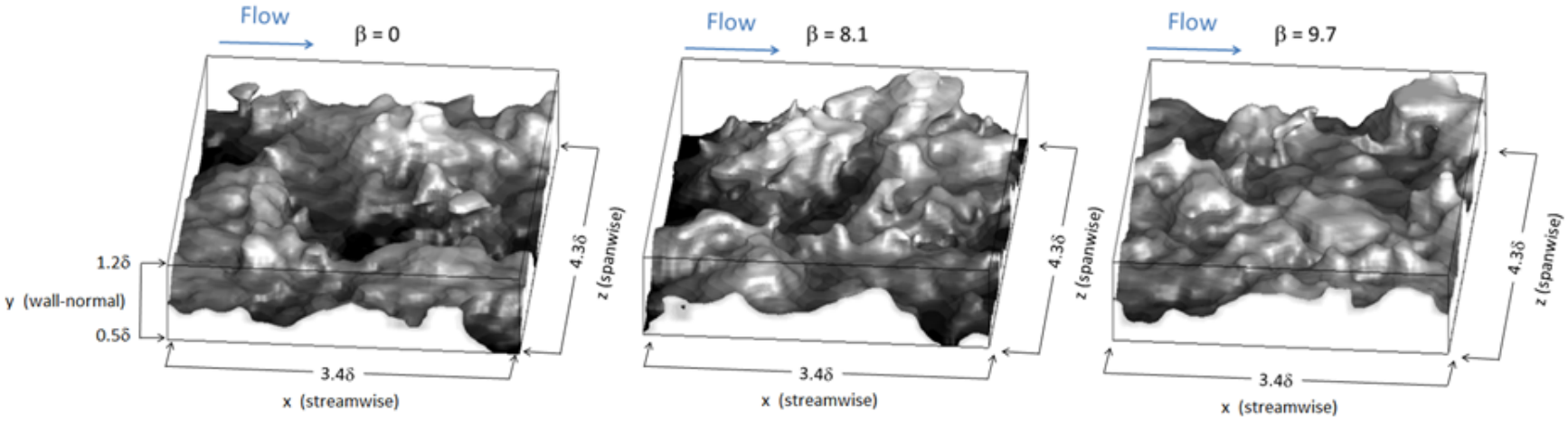

Figure 6.9: Sample instantaneous 3-D flow visualizations at different pressure gradients (flow from left to right)

An iso-surface is used to show the location of the boundary layer edge with color corresponding to the wall-normal height of the instantaneous boundary layer edge. The dimensions are 3.4δ in the streamwise direction and 4.3δ in the spanwise direction for all three cases each normalized by its average boundary layer thickness. The wall normal height spans from 0.5δ to 1.2δ for all three cases.

Figure 6.10 shows overhead views of the same three instances in the first row with two additional examples from each case in the second and third rows. At first glance, the 3-D visualization for the ZPG and APG cases are quite similar. The boundary layer edge has the appearance of a rough surface with a variety of scales and features. In all three cases, large scales on the order of a boundary layer thickness can be observed as well as smaller, bumpy features at the boundary layer edge. Upon closer inspection, some differences are noticed. For the first instance of the zero pressure gradient case, there appears to be three large features as highlighted by solid black circles in the overhead view of Figure 6.10. There are also two large valleys in the image - as shown by the white dotted circle - one at the center and one in the top left which show the instantaneous boundary layer edge dipping under 0.5δ.

For the first case of $\beta = 8.1$ in Figure 6.10, the features vary in size and are spaced at different distances. There is a large feature (or conglomeration of features) in the upper half of the overhead view, which extends over 1.5δ in the streamwise and spanwise direction. There are some smaller structures in the lower half of the image that extend away from the wall, but do not appear to be connected to a larger scale structure. For the first overhead view of the $\beta = 9.7$ case, small structures of about a size of 0.5δ are seen scattered throughout the image, but are not as distinct as observed in the zero pressure gradient case.

From investigating the entire collection of flow visualization images in 3-D and slices in 2-D, a few general observations can be made. The structures at the boundary layer edge occur as a variety of shapes, not appearing circular or elliptical in many instances. For all three cases, the structures have similar heights and depths, extending in the wall-normal

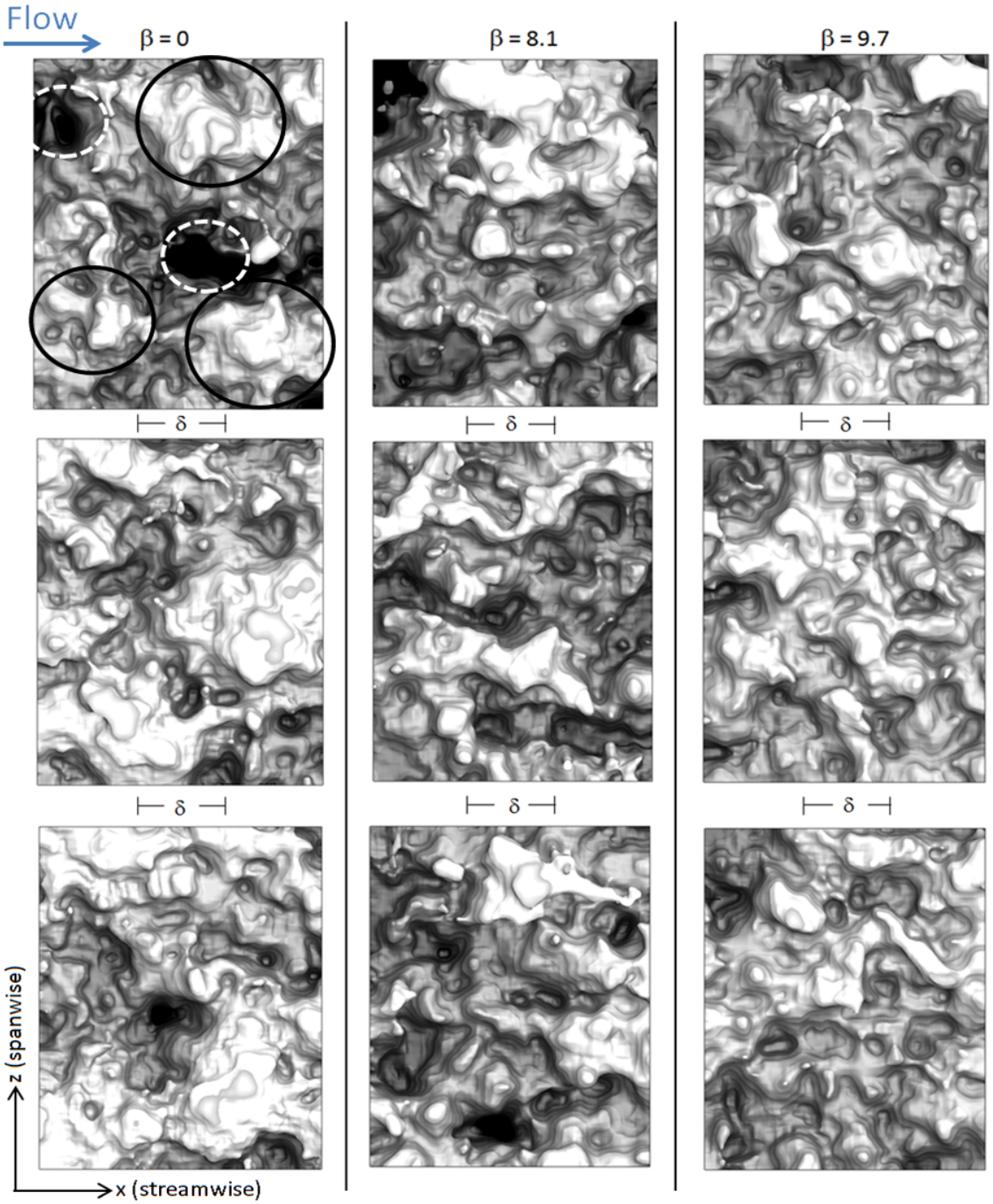

Figure 6.10: Overhead views of flow visualization volumes for the $\beta = 0$, $\beta = 8.1$, $\beta = 9.7$ cases (flow from left to right)

direction to over 1.2δ and dipping down to $.5\delta$ in the span of less than 1δ in the streamwise and spanwise directions. Structures observed in the adverse pressure gradient cases tend to be not as large or distinct as in the zero pressure gradient case. Rather, their size is more varied whereas in the zero pressure gradient case the size is larger and more uniformly distributed. In a similar vein, structures in the zero pressure gradient case appear to be spaced further apart. The structures in the ZPG case are more often aligning and coalescing in larger turbulent bulges. In contrast, for the APG cases, the structures near the edge of the boundary layer are smaller, each in its own region of the flow and making a smaller protuberance in the boundary layer edge. No organization or preferential alignment of the structures with each other is noticeable by looking at the 3-D flow visualization volumes for any of the cases. There does not appear to be an appreciable difference in the inclination angle of the structures as the pressure gradient changes. The structures in each case have a variety of angles from horizontal with most being inclined in the flow direction between 30 and 60 degrees. The flow features in the 3-D visualizations indicate small differences in the flow behavior of the three different pressure gradients. Although there is no discernible alignment or organization, the features of the ZPG case are more uniform and slightly larger than the APG cases, but more quantitative measurements are needed to make this connection.

6.5.2 Power Spectral Density

Each wall-normal slice of the flow visualization volumes was transformed using a two-dimensional fast Fourier transform. The magnitude of the transform for a certain wave number (κ_x or κ_z) gives an objective indication of the relative importance of structures of that size in the image. To compare the size of structures in the flow visualization data at different wall-normal heights and at different pressure gradients, the magnitude of the Fourier transforms for certain wave numbers (κ_x or κ_z) are compared. The Fourier transform in the wall-normal direction was also computed, but it presented little additional information due to the relatively small number of samples, 14, in the wall normal direction.

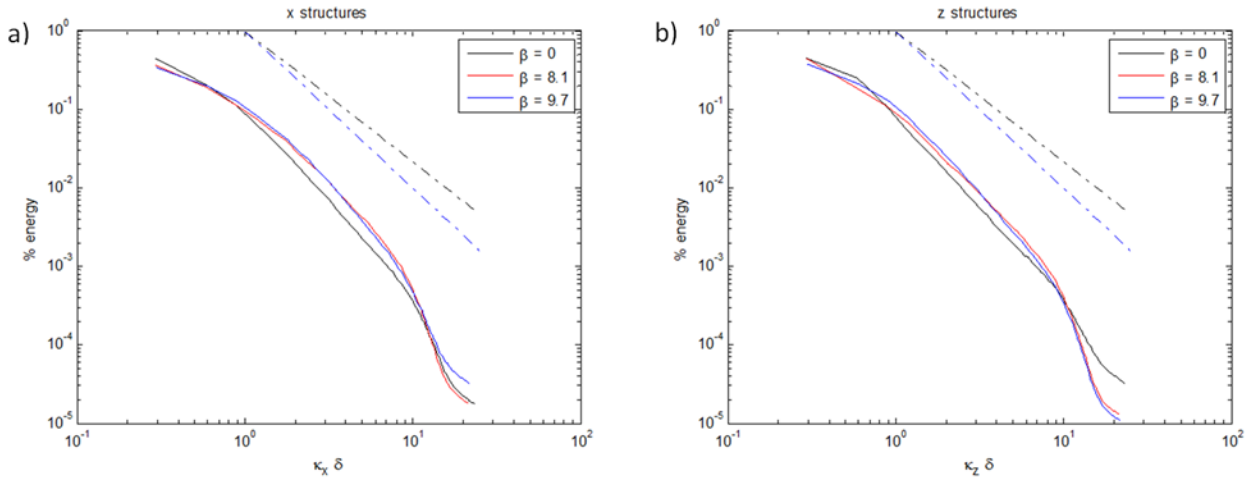

Figure 6.11: Power spectral density of the Fourier transformed intensity images and normalized by unity for each of the three pressure gradients at a wall normal height closest to y = 0.88δ a) κ_x integrated over all κ_z values b) κ_z integrated over all κ_x values

Figure 6.11 shows the average power spectral density of the intensity images normalized to unity for all three pressure gradients and a) integrated over all κ_z values or b) integrated over all κ_x values. The wave numbers (κ_x and κ_z) are normalized by the average boundary layer thickness, δ Figure 6.11 shows the power spectral density for a wall normal height closest to y/δ =0.88, although the same analysis was repeated for slices taken at all wall normal heights visualized in this study.

In all of the wall-normal heights for all pressure gradients, the lowest frequencies contain more energy than the higher ones. The spectra does not contain a distinct peak in the low frequency range indicating that scales larger than the field of view (4.3δ by 3.4δ) are present in the flow for all cases. In comparing the spectra for different pressure gradients, the β = 0 case has a higher spectral energy for κ_x δ values of less than 0.7 whereas the adverse pressure gradient cases have greater spectral energy above this value. This corresponds to a wavelength of approximately $1.4\delta$and indicates that the larger structures ($>1.4\delta$) occur more often in the zero pressure gradient case, whereas the adverse pressure gradient cases had smaller structures ($<1.4\delta$) appear more frequently. This is consistent with the observations made from inspection of the instantaneous flow visualization images.

In all cases, the energy in the structures decreases at a steeper slope compared to the $\kappa_x^{-5/3}$ curve which is commonly seen in the power spectral density of boundary layer velocity measurements. Here, the $\kappa_x^{-5/3}$ curve is shown for comparison only, as one would not necessarily expect the intensity power spectral density to follow the velocity exactly. Similarly, for wavelengths less than 1.4δ and greater than 0.1δ, the adverse pressure gradient cases had more energy than the zero pressure gradient case for structures in the spanwise direction as shown in Figure 10b. There are minimal differences in the structures in the streamwise (Figure 10a) and the spanwise (Figure 10b) directions. For all cases there is a drop off in the spectral density for the smaller structures at the right end of the graph due to the smoothing filters and deletion of the smallest features ($<0.05\delta$) to account for noise in the images.

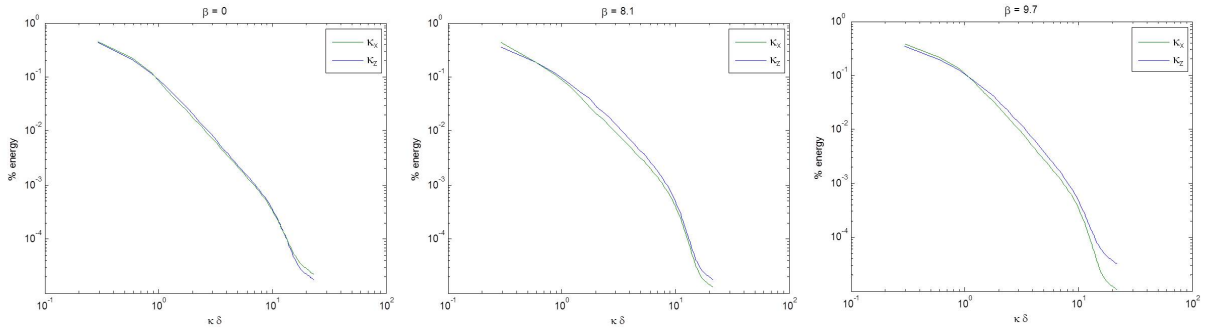

Figure 6.12: Power spectral density of the Fourier transformed intensity images (normalized to unity) for all three pressure gradients at a wall normal height closest to y=0.88δ for κ_x integrated over all κ_z values (green line) and κ_z integrated over all κ_x values (blue line)

Figure 6.12 shows the power spectral density of streamwise (x) and spanwise (z) structures on the same graph at one wall-normal height (y=0.9δ) for each pressure gradient. In the APG cases, there is more energy in the larger wavelength structures (lower frequency) in the streamwise direction compared to the spanwise direction. There is more energy in the spanwise direction for structures less that about 1 boundary layer thickness in the APG

cases. This suggests that the structures are longer in the streamwise direction than the spanwise direction for the APG cases, but for the ZPG case, the structures in both direction are nearly identical, suggesting more circular features.

Figure 6.13 shows the power spectral density computed for 2-D images positioned at different wall-normal heights. Each curve is normalized such that relative importance (or prevalence) of a particular scale relative to other scales within the image can be identified. For the ZPG case, the general trends are similar for all heights. While curves at each wall-normal height are not exactly in order, generally, there is a slight redistribution of energy towards the smaller scales as wall-normal height increases, which is consistent with observations from the 3-D volumes. For the APG cases, the trends are similar, but changes associated with the wall normal position are more pronounced indicating a stronger dependence of the structure size on the wall-normal position. In particular, there is an inflection point near the middle of the graph at a $\kappa_x\delta$ value between 2 and 3, corresponding to structures with a wavelength between 0.3δ and 0.5δ. Not exclusively, but generally, there is more energy in the structures greater than 0.5δ at the smaller wall normal heights, and there is more percent energy at the smaller structures further away from the wall.

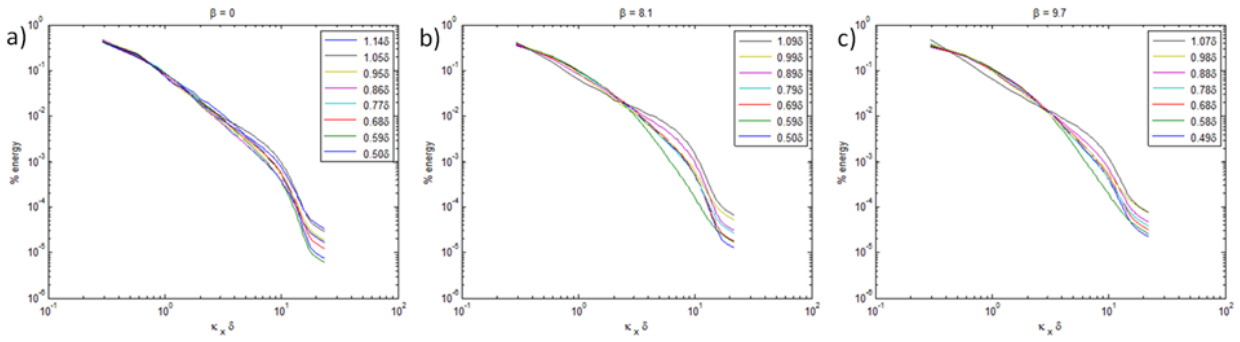

Figure 6.13: Power spectral density of the Fourier transformed intensity images and normalized by unity for each of the three pressure gradients at select wall normal heights (κ_x integrated over all κ_z values)

6.5.3 Binary Images

To further identify and quantify large scale features, the flow visualization images were converted to binary such that inside the boundary layer edge corresponds to a value of one and outside the boundary layer is zero. By converting the images to binary, the structures outlined by the boundary layer edge are easily identifiable using the "regionprops" function in MATLAB's Image Processing toolbox. This function gives an objective description of the location, size, and shape of the features in the boundary layer without regards to intensity gradients within the boundary layer. In each horizontal slice (x-z plane) the "islands" which feature the inside of the boundary layer surrounded by the boundary layer edge are identified and their centroid locations and areas are calculated. Figure 6.14 shows the number of islands and the average area (normalized by δ^2) in each wall-normal slice for all three cases.

The largest number of islands occurs between about 0.7δ and 1.1δ for all three cases, indicating that this is the location where structures can most uniquely be identified in the context of the current visualization method. These wall-normal locations will be the focus of investigation in subsequent sections. The average area, or size, of the islands decreases with increasing wall-normal height as one would expect as shown in Figure 6.14. Beyond approximately 1.1δ very few structures can be identified with the average size being quite small for those that are identified. The average area of the features in the zero pressure gradient case is generally larger than the adverse pressure gradient case for nearly every wall normal height, which is consistent with earlier observations, indicating that the flow in the outer region of the boundary layer is more often organized in larger turbulent bulges compared to the APG cases. The structures in the ZPG case are not divided by the boundary layer edge into multiple, smaller features, but lie inside the boundary layer leading to larger areas of the binary features in these 2-D, streamwise-spanwise slices. From the area calculations of the binary images, the case of $\beta = 8.1$ averaged a smaller area than the case of $\beta = 9.7$ for most wall-normal heights which was not apparent in the visual detection of the turbulent

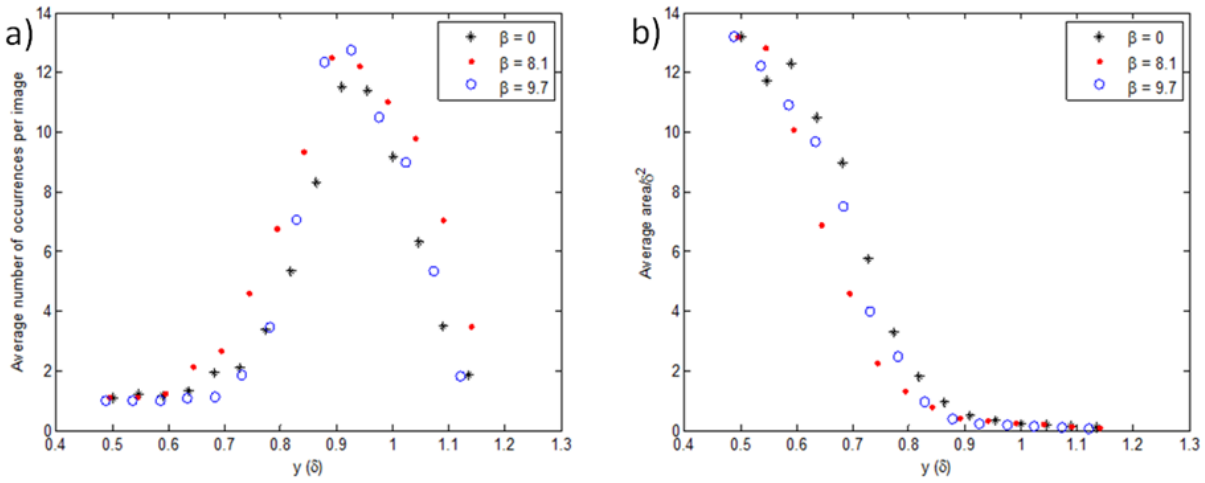

Figure 6.14: a) Average number of islands and b) average area of the islands (normalized by δ^2)

motions in the previous section. However, both APG cases consistently averaged areas less than the ZPG case at nearly every wall-normal height.

6.5.4 Conditionally Averaged 3-D Structures

Another method for analysis is to form a conditionally averaged 3-D flow visualization image based on some criteria about structures. In this work, a structure is characterized by its size and location at some wall normal height within the binary images (i.e. its footprint). As the binary image represents the presence of low momentum fluid, the method described here essentially identifies 'ejections' of low momentum fluid from the wall to the outer portion of the boundary layer. Based on the results described in the previous section, the largest numbers of ejections are found between a wall normal height of $.8\delta$ to 1.1δ. Initially, a height of 1.0δ is chosen at which to identify the size and centroid location of structures. Once a structure is identified, the remaining slices in the volume are spatially shifted such that the structure is nominally located at the center of the volume. This process is repeated for all of the 3-D visualizations, and all shifted volumes are averaged to form a conditionally averaged view of 3-D structures that meet the criteria. It should be noted that although

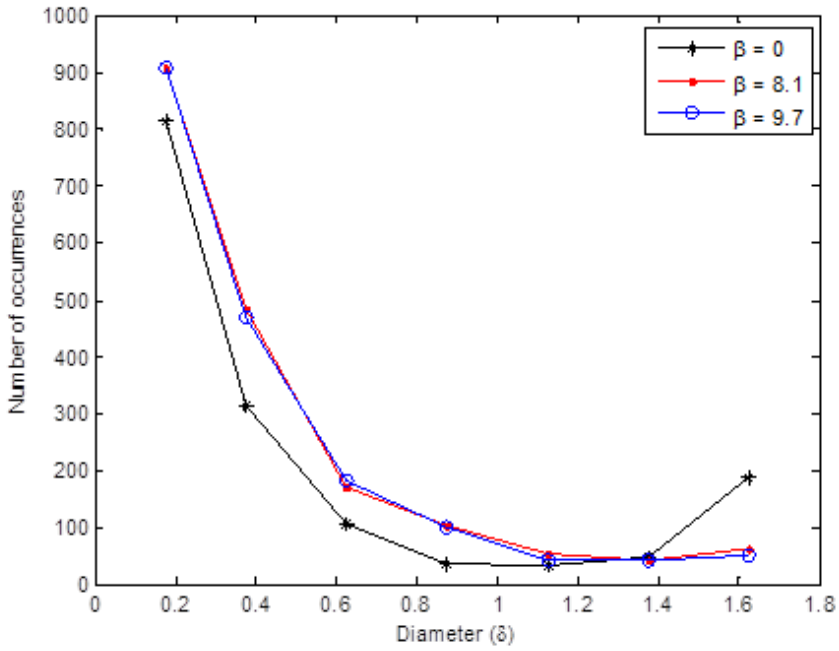

Figure 6.15: Histogram of occurrences for conditional averaged features with respect to feature size at a wall-normal height of 1.0δ

binary images are used to identify a structure, the conditional averaging is performed on the intensity images.

One criterion for selecting a structure is that it must occur in the inner 25% of the field of view so as to allow for the volume around the structure to be large enough for investigation. The distribution of the area of structures identified in this manner is shown in Figure 6.15. The two adverse pressure gradient trials contained more structures with an area between that of a circle with a diameter between 0.1δ and 1δ (first four data points) compared to the zero pressure gradient case. The zero pressure gradient case had more large structures as shown in Figure 6.15 with the last data point being the number of structures with a diameter above 1.5δ. The histogram serves as an objective measure of the size of structures similarly to a Fourier transform.

The conditionally averaged structures with an area of a circle with a diameter between 0.75δ and 1.0δ are shown in Figure 6.16. For each of the adverse pressure gradients, there were about 120 instances of a structure of this size at a wall-normal height of 1.0δ. For

the zero pressure gradient case, there were 52 instances. Figure 6.16 part a utilizes an isosurface at 60% of the maximum phase-averaged intensity value to present an imprint of the 3-D shape of the structure. The color of the isosurface is defined by the wall-normal location so as to highlight the differences in the height of the structure for each case. Figure 6.16 part b shows a streamwise/wall-normal (x-y) slice at the center of the average structure colored by the average intensity (arbitrary units) of the smoke. Figure 6.16 part c presents the same slice as Figure 6.16 part b, but with the non-conditionally averaged mean intensity subtracted. This effectively highlights the difference between the structure and the 'usual' state of the flow visualization images thus providing an idea for the influence a structure has on its surroundings.

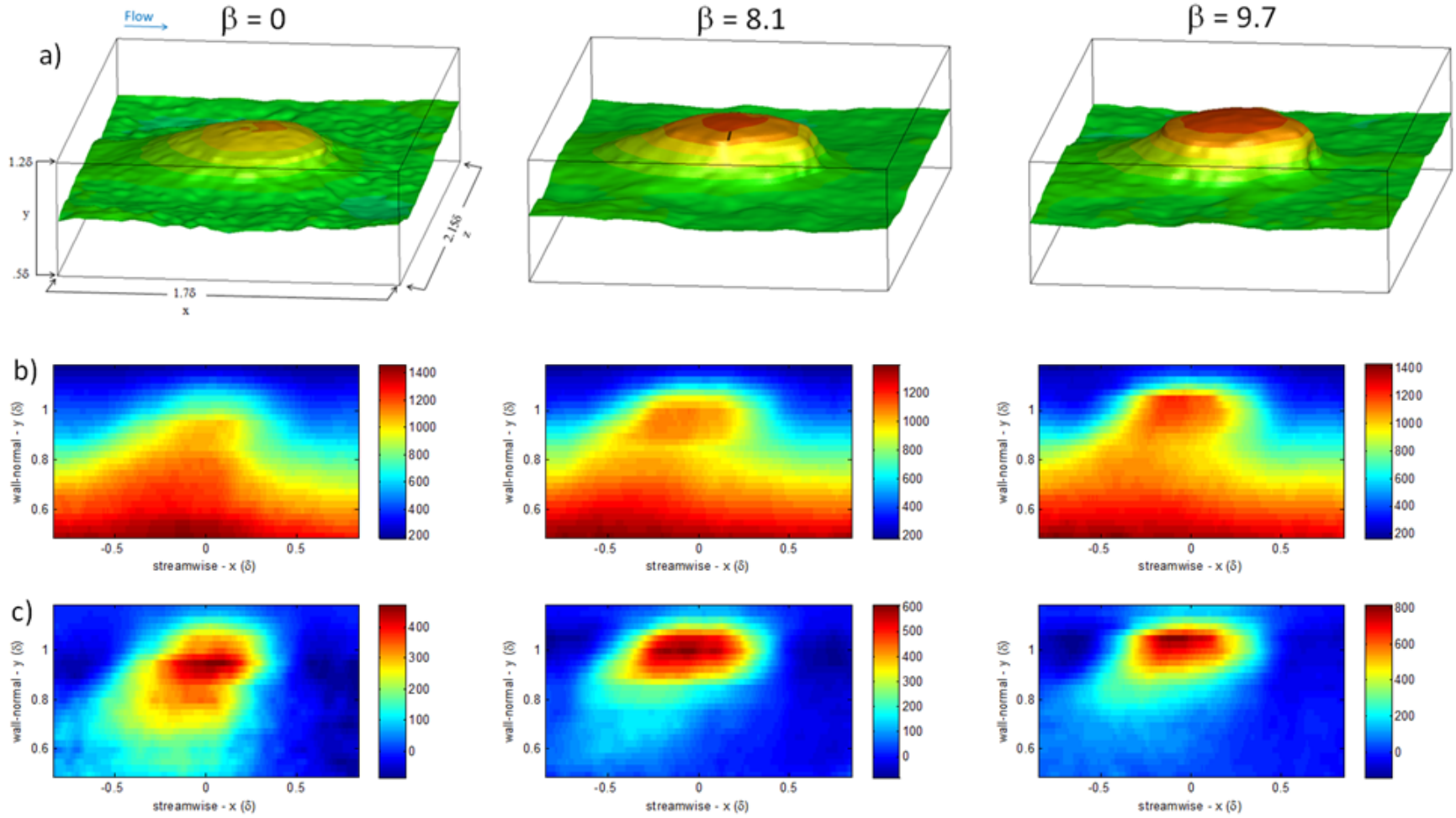

Figure 6.16: Conditionally averaged features at y = 1.0δ with a diameter between 0.75δ and 1.0δ, a) 3-D flow visualization b) streamwise/wall-normal slice and c) streamwise/wall-normal slice with mean subtracted

The three dimensional flow visualization of the smoke intensity around a feature at 1.0δ is shown in part A of Figure 6.16. The fluid at the center is more intense and extends into the boundary layer edge. The features are inclined in the flow direction between 45 and 50 degrees from the streamwise direction. There are some differences in the three cases. There are twice as many instances of a feature which fit the criteria for the APG cases, leading to the more uniform and smoother surface compared to the ZPG case. The isosurface of the 3-D structure shows that the conditionally averaged structure in the adverse pressure gradient cases extends higher in the wall-normal direction than in the ZPG case. The ZPG structure is wider and has a more gradual inclination from the surrounding fluid. The middle slice (part B) of the structure shows some similar features for all three cases, but with a slightly more well-defined core for the APG cases. By subtracting the mean from the feature, the differences in the three cases are enhanced as seen in part C. The APG structures' 3-D extent is located further away from the surface. The intensity of the core of the ZPG feature is about half the intensity of the core of the APG cases. Thus, when using the same criteria to identify structures in all three cases, structures in the APG case appear to be located further away and separate from the wall. In addition, they do not, at least on average, appear to be connected to the presence of a larger structure below the feature as compared to the ZPG case.

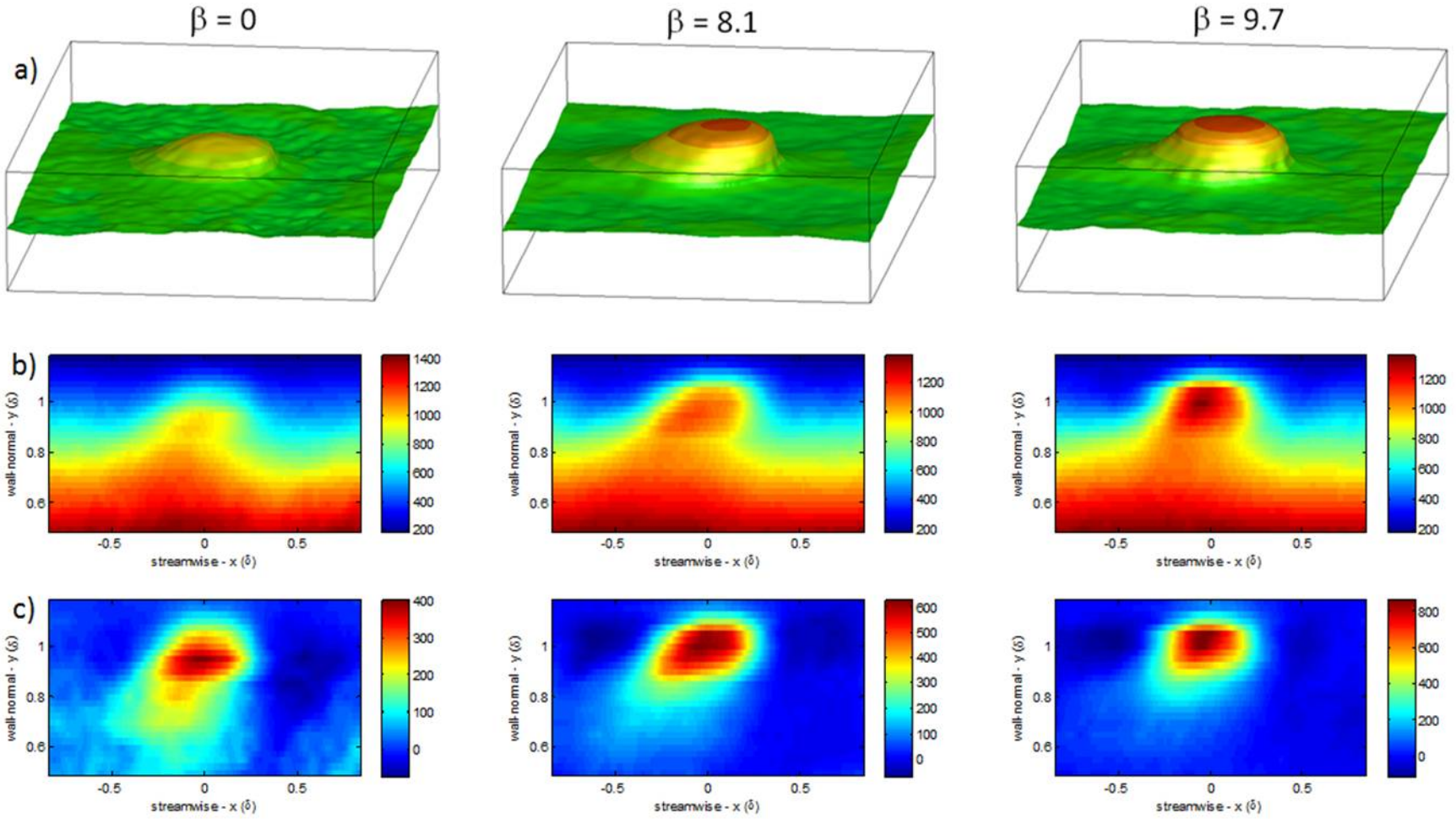

Figure 6.17: Conditionally averaged features at y=1.0δ with a diameter between 0.5δ and 0.75δ a) 3-D flow visualization b) streamwise/wall-normal slice and c) streamwise/wall-normal slice with mean subtracted.

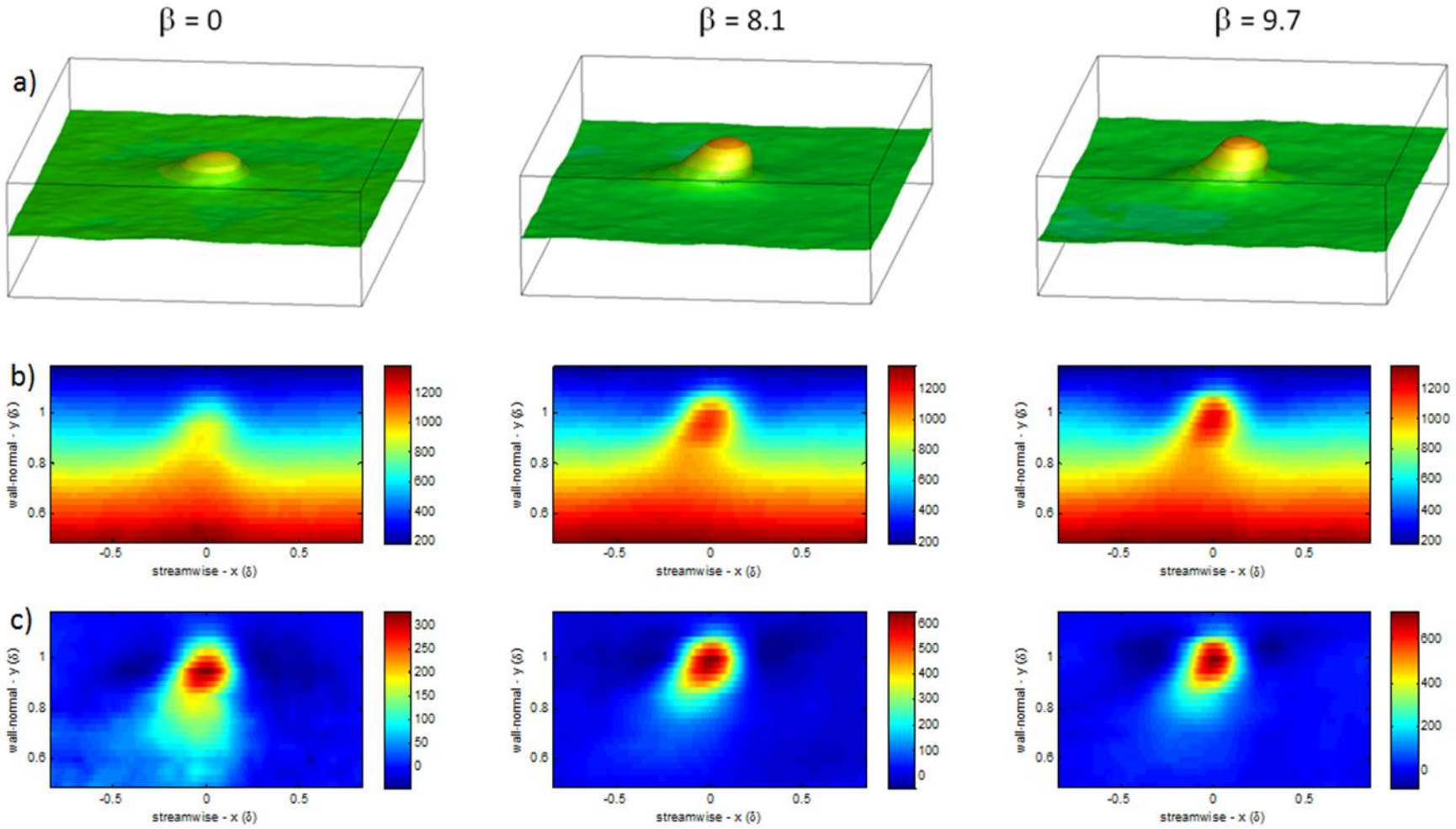

Figure 6.18: Conditionally averaged features at y=1.0δ with a diameter between 0.25δ and 0.5δ a) 3-D flow visualization b) streamwise/wall-normal slice and c) streamwise/wall-normal slice with mean subtracted.

Many of the same characteristics are seen in features of a different size at the same wall-normal height (y=1δ). Figure 6.17 shows features with a diameter between 0.5 and 0.75δ, and figure 6.18 are features with a diameter of between 0.25 and 0.5δ. For these smaller structures, the APG cases extend higher than the ZPG case. The intensities at the center of the features in the mean subtracted plots in Figure 6.17 and 6.18 appear to increase with increasing adverse pressure gradient, suggesting that the pressure gradient is making the conditionally averaged features more distinct from the surrounding fluid. The mean subtracted ZPG feature appears more connected to the fluid closer to the wall, whereas the APG cases are separated from the fluid underneath. The inclination angle for the ZPG case is closer to 50 degrees from horizontal, whereas the APG cases are at a roughly 45 degree angle in the streamwise direction. The differences in the three pressure gradients are consistent for the sizes of structures in Figures 6.16 and 6.17. It is also worth noting that there does not appear to be any neighboring structures in the conditionally averaged data possibly indicating that the large-scale structures observed here exist independent of one another.

The shape of the conditional averaged structures can also be compared by extracting a slice in the streamwise-spanwise plane at y=1.0δ. Figure 6.19 shows the shape of the contour lines at 60% of the maximum intensity at y=1.0δ. The three pressure gradients are plotted for structures between 0.25δ and 0.5δ, 0.5δ and 0.75δ, and 0.75δ and 1.0δ. The shapes of the structures are very similar with all three pressure gradients practically at the same curves. For structures between 0.75 and 1.0δ, the slight variations in the curves may be attributed to the fewer number of instances of structures of that size for all three cases. For all the streamwise-spanwise slices, the shape of the structures is slightly elongated in the streamwise direction compared to the spanwise direction. The eccentricity of the curves all lie between 0.63 and 0.69 for all three cases at the three pressure gradients.

The effect of the height at which to identify the initial feature is explored by looking at a wall-normal height above (1.1δ) and below (0.9δ) that used in Figures 6.16 and 6.17.

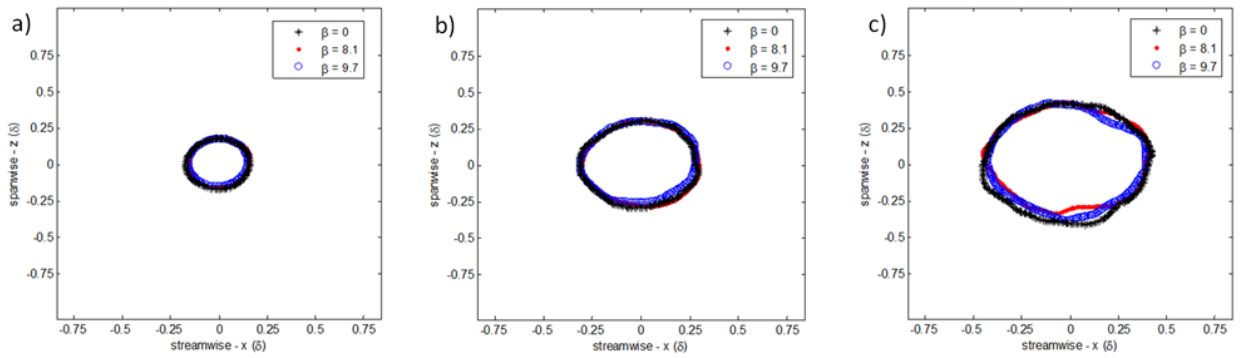

Figure 6.19: Spanwise-streamwise profile of the conditionally averaged structure, lines at 60% of the maximum intensity for a) structures between .25δ and .5δ, b) structures between .5δ and .75δ, c) structures between .75δ and 1.0δ

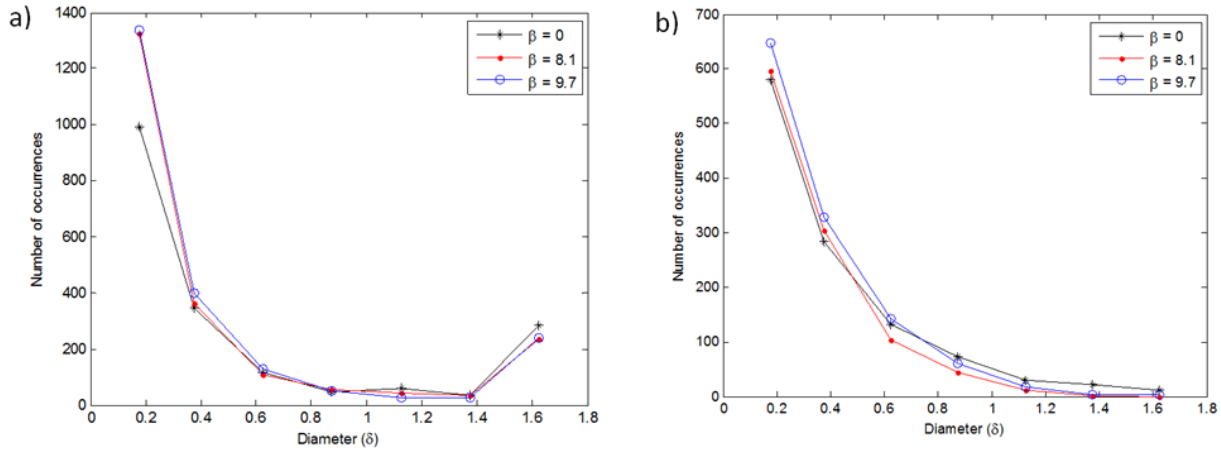

Figure 6.20: Histogram of occurrences for conditional averaged features with respect to feature size at a wall-normal height of a) 0.9$\delta$and b) 1.1δ.

Keeping the criteria for identifying a feature the same (a binary "island" in the inner 25% of the image), the number of occurrences distributed by size of structure is shown in Figure 6.20 for a wall-normal height of a) y=0.9δ and b) y=1.1δ. The number of occurrences decreases with increasing size for all three cases. At y=0.9δ, there are over 35% more instances of a feature between 0.1δ and 0.25δ for the APG cases compared to the ZPG case. The number of occurrences of a feature and its decreasing trend with increasing size are very similar for the three cases at the wall normal height of y=1.1δ. The largest features of a structure are not prevalent at wall normal heights above 1.0δ.

Figure 6.21 shows the conditional averaged features between 0.25δ and 0.5δ in diameter at y=0.9δ and figure 6.22 shows the conditional averaged features at y=1.1δ. The features at the center are more intense than the surrounding fluid, and the isosurface outlines a bump in the boundary layer edge at the center. The features at these new heights in Figure 6.21 and 6.22 can be compared to the conditionally averaged features at y=1.0δ in Figure 6.18. At y=0.9δ, the bump in the ZPG case is slightly smaller and less intense than the APG cases, but this trial is much more similar than the three cases are at y=1.0δ and y=1.1δ.

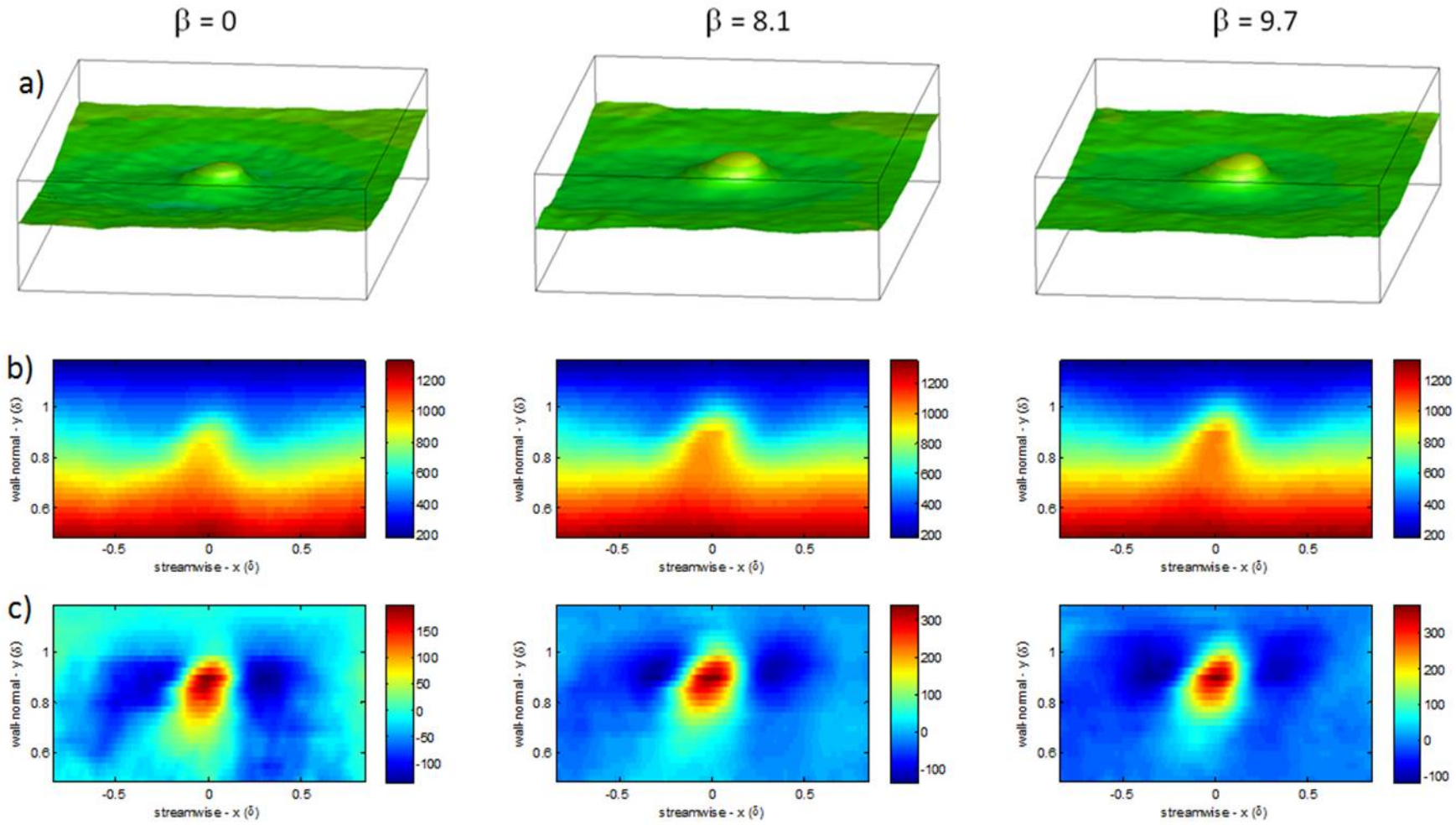

Figure 6.21: Conditionally averaged features at y=0.9δ with a diameter between 0.25δ and 0.5δ a) 3-D flow visualization b) streamwise/wall-normal slice and c) streamwise/wall-normal slice with mean subtracted.

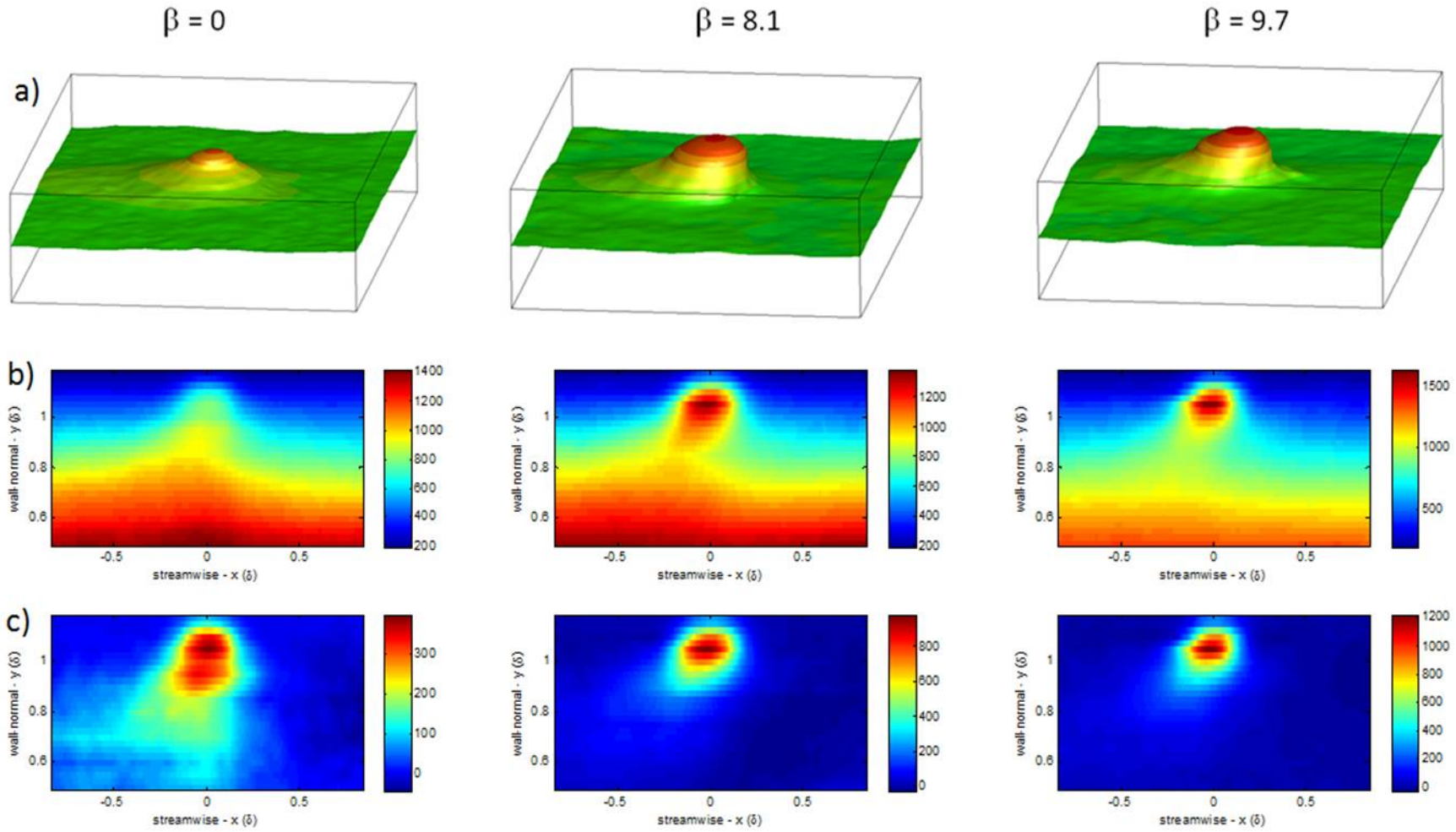

Figure 6.22: Conditionally averaged features at y=1.1δ with a diameter between 0.25δ and 0.5δ a) 3-D flow visualization b) streamwise/wall-normal slice and c) streamwise/wall-normal slice with mean subtracted.

The 3-D visualization in the top row shows the isosurface extending slightly higher in the wall-normal direction for the APG cases. The 3-D visualization of a feature at y=1.1δ is significantly higher for the APG cases than the ZPG cases. The shape of the structure at y=1.1δ is also different for the APG cases, where the ZPG case looks like just the tip of the much larger feature underneath and the APG cases are more distinct accumulations of intensity inclined in the streamwise direction. In fact, with increasing adverse pressure gradient at y=1.1δ, the features appear to be separating from the fluid closer to the wall, though careful observation of flow visualization and velocity measurements showed no evidence of boundary layer separation (or intermittent transitory detachment) in the flow. This indicates a de-correlation of the fluid intensity between the inner and outer regions of the flow. The pressure gradient is known to effect the inner region of the flow and the near wall portion differently in velocity measurements, and the corresponding change in the smoke intensity in the inner and outer region reflects that fact. These figures show that the increasing wall-normal height at which the structures are identified and investigated causes more significant differences in the shapes of the 3-D conditionally averaged features.

At a wall-normal height less than 0.9δ, the number of occurrences of well-defined "islands" in the binary images rapidly decreases as the smoke coalesces and more of the image is inside the boundary layer edge. Therefore, the number of instances which fit the criteria for the conditionally averaged features decreases such that investigating below a wall-normal height of 0.9δ is unsuitable by the previous means. However, at these heights closer to the wall, there are portions of the image which are still in the freestream (zero intensity in the binary images), and as such, investigating the areas of the image in which there is no intensity in the binary images could be useful in trying to peek into the fluid closer to the wall. Therefore, the same criteria as before are used (looking at a feature in the inner 25% of the image) at locations of 0.8δ and 0.7δ; however, in these cases features which lack smoke (opposite from the previous work in this section) are shown. In this section, these will be referred to as conditionally averaged valleys instead of conditionally averaged features. In

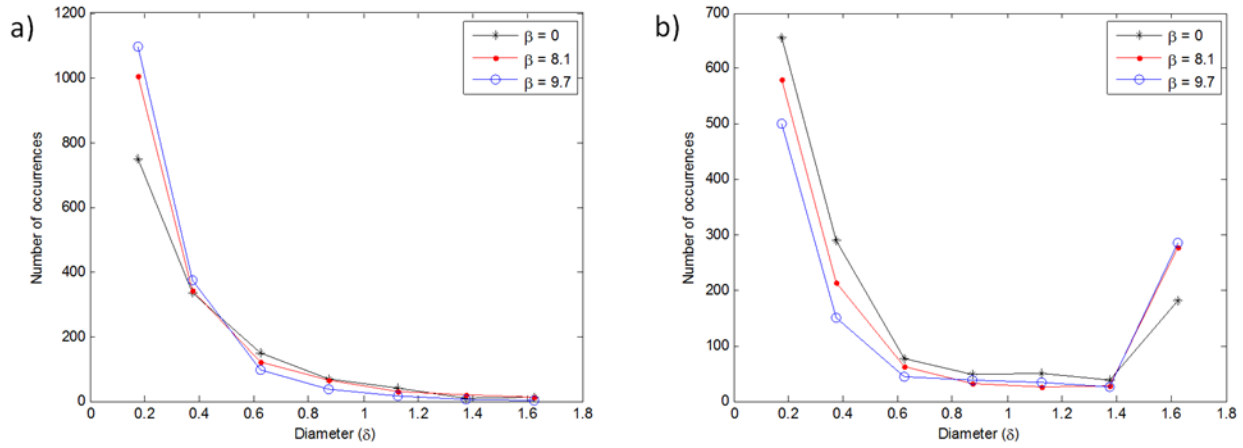

Figure 6.23: Histogram of occurrences for conditional averaged features of no smoke with respect to feature size at a wall-normal height of a) 0.7δ and b) 0.8δ

a sense, these features represent "valleys" or intermittency of high momentum, unseeded freestream fluid into the low-momentum, seeded boundary layer flow.

Figure 6.23 shows the number of occurrences of these valleys. At a boundary layer height of 0.7δ, there are more instances of small features of no smoke in the APG cases, whereas, at y=0.8δ, there are more occurrences in the ZPG case for most of the sizes, except for sizes larger than 1.5δ.

The 3-D conditionally averaged valleys are shown in Figure 6.24 for sizes between 0.25δ and 0.5δ at y=0.7δ and Figure 6.25 for valleys at y=0.8δ and y=0.7δ, organized similarly to those in Figures 6.17 and 6.21. It is difficult to see the difference in the 3-D flow visualizations in the first row for a height of y=0.7δ. The valleys in the center are similar and the side view through the midplane in part B show similar features. Subtracting the average emphasizes a few differences in the three cases. The extent of the strongest adverse pressure gradient is slightly higher than the bottom of the volume compared to the two other cases. Also the inclination of the ZPG valley is at a larger angle from horizontal compared to the two APG cases.

At a height of y=0.8δ (in Figure 6.25), there are fewer occurrences of the APG cases, leading to a more bumpy iso-surface for the 3-D flow visualization. The final row in Figure 6.25 shows that for the ZPG case, the freestream fluid penetrates the boundary layer further and closer to the wall. This is similar to the positive conditionally averaged features at y=0.9δ and above discussed in the previous section. The instances of no smoke for the ZPG more often have no smoke underneath it whereas, the instances of no smoke in the APG cases are not necessarily a part of a deeper valley. This was noticeable in the 3-D flow visualizations in part A of this section, where the ZPG case had more occurrences of valleys which were deeper than the APG cases. Conditionally averaged valleys sized between .5δ -.75δ, .75δ -1.0δ, and 1.0δ -1.25δ were investigated at 0.7δ and 0.8δ with similar results that ZPG cases show deeper valleys and were inclined at steeper angles than the APG cases. Negligible differences were seen with these larger structures, and the full data set and images at all heights and feature size can be seen in the appendix for completeness.

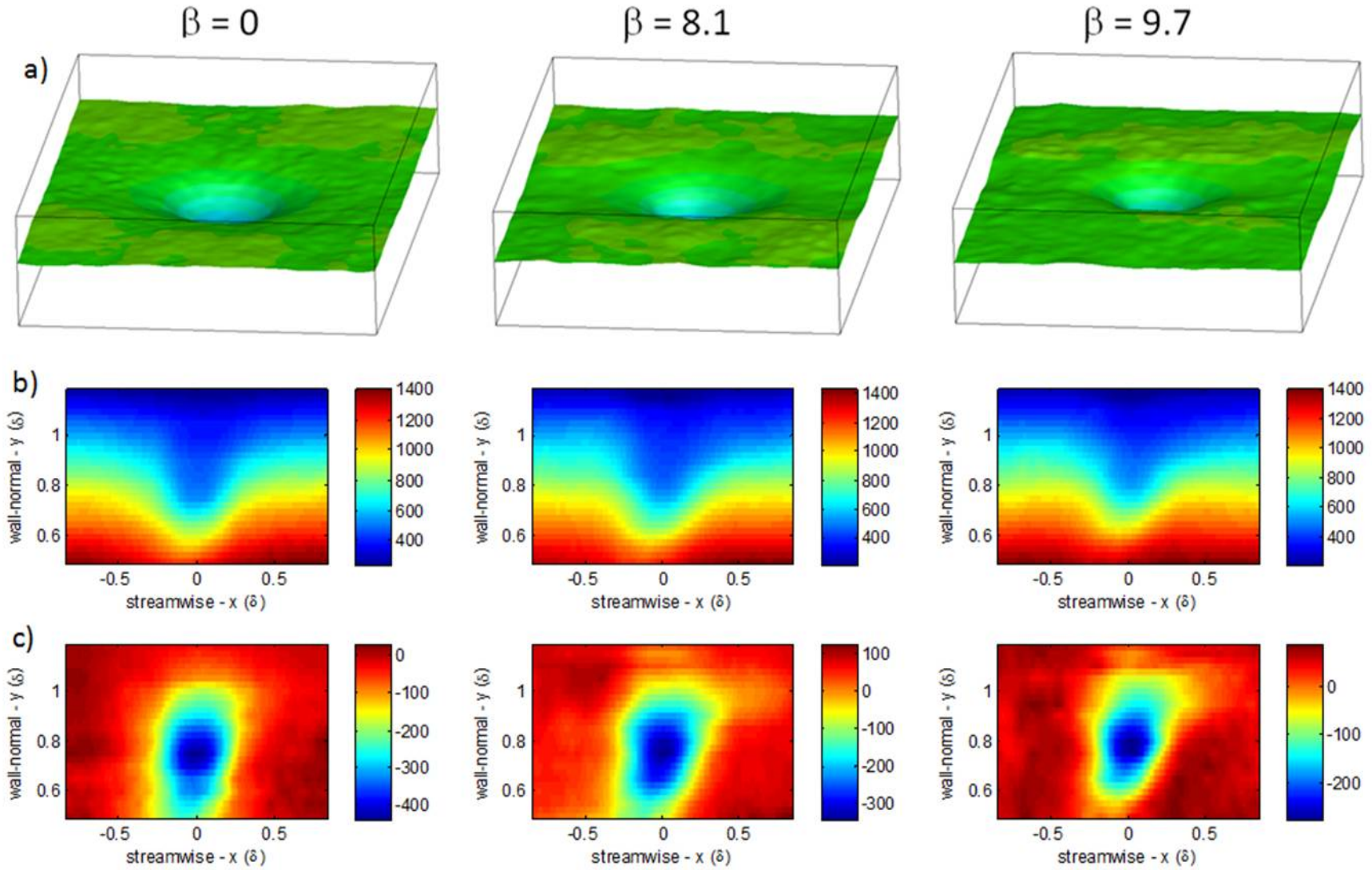

Figure 6.24: Conditionally averaged valley at y=0.7δ with a diameter between 0.25δ and 0.5δ a) 3-D flow visualization b) streamwise/wall-normal slice and c) streamwise/wall-normal slice with mean subtracted.

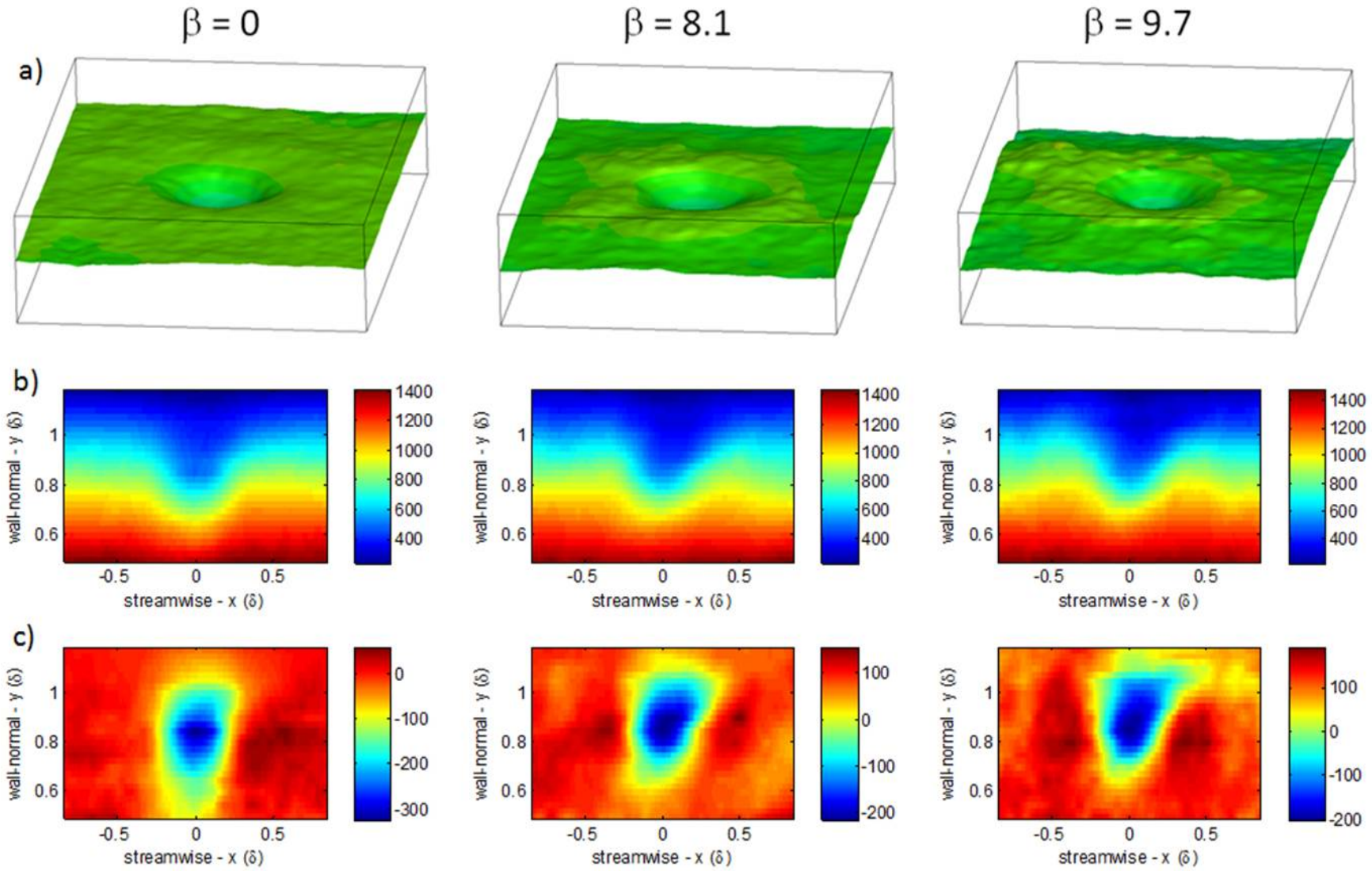

Figure 6.25: Conditionally averaged valley at y=0.8δ with a diameter between 0.25δ and 0.5δ a) 3-D flow visualization b) streamwise/wall-normal slice and c) streamwise/wall-normal slice with mean subtracted.

6.6 Discussion

As shown in previous chapter, the smoke in the boundary layer for this experimental setup accurately identifies the low momentum fluid and serves as an appropriate marker for the large scale motions in the outer region of the turbulent boundary layer [67]. For this trial, three-dimensional flow visualization snapshots of the intensity of the seeded flow were captured for a zero pressure gradient turbulent boundary layer and two adverse pressure gradient turbulent boundary layers. For comparison, 488 volumes for each pressure gradient were analyzed. Direct observation of the three-dimensional volumes consistently showed that the structures in the ZPG turbulent boundary layer were larger, more well-defined, and spaced farther apart than the features at the boundary layer edge in the adverse pressure gradient cases. Using the Fourier transformed intensity to more objectively compare the three cases showed that the power spectral density for the zero pressure gradient case contained more energy in the structures with a wavelength of 1.4δ and above than in the adverse pressure gradient case; whereas the adverse pressure gradient case had more energy in structures with wavelengths between 0.1δ and 1.4δ.

Converting the intensity images to binary images to specify whether the fluid lies inside of the boundary layer or in the freestream has previously been shown to effectively mark boundary layer edge [67]. Investigation of these binary slices using the regionprops function in MATLAB showed maximums in the number of islands between 0.85δ and 0.95δ for all three cases. The areas of the ZPG features were larger than the APG cases at just about every wall-normal height which confirms that the sizes of the structures are indeed larger, relative to the boundary layer thickness, for the ZPG case.

The conditionally averaged images with a feature near the center of the image at y = 1.1δ showed significant differences in the three cases. The structures in the APG cases were more intense than their surroundings compared to the ZPG case. The features also extended higher in the wall-normal direction for the APG cases. The number of occurrences of a feature at 0.9δ 1.0δ and 1.1δ showed that the ZPG case had fewer small structures and more large

structures than the APG cases. The difference between the numbers of occurrences of a conditionally averaged structure for the three pressure gradients decreased with increasing wall-normal height. The features grew taller with increasing pressure gradient and the signal of the smoke seemed to be disconnected from the smoke underneath almost as if it were about to separate though the flow was fully attached. This apparent disconnection was most evident at a wall-normal height of 1.1δ. There appeared to be no differences in the elliptical shape of the conditionally averaged features in the streamwise-spanwise direction, all with eccentricities between 0.63 and 0.69.

With increasing wall-normal location of the feature, the differences in the shapes of the feature increased with increasing pressure gradient. This distinct separation of the fluid in the features in the APG cases suggests more of an independence of the inner and outer layers in this case compared to the ZPG case. The ZPG conditionally averaged features were more connected to a larger feature closer to the wall. Similarly, the conditionally averaged valleys showed more of a connection to the fluid closer to the wall for the ZPG case compared to the ZPG cases. The disconnectedness of the APG conditionally averaged intensity images shows a loss of correlation between the outer region of the flow and the inner region, as the effect of the pressure gradient differs between the two regions. For the positive features and the negative valleys, the inclination angle of the features for the ZPG was greater than that of the APG features, and was more noticeably different closer to the wall.

It is universally known that the wake region of the turbulent boundary layer increases in an adverse pressure gradient [33]. The increase in sweep motions impacts coherent motions in the outer region [35] and the peak in Reynolds stress moves further from the wall in the APG turbulent boundary layer compared to the ZPG [37]. The conditional averaged structures in this chapter also indicate this behavior of structures residing further away from the wall compared to the ZPG case. This further validates the evidence that flow visualization does follow the behavior of the structures in the flow. Making observations from the seeded smoke

in the boundary layer will produce similar results from velocity and vorticity measurements from literature.

The results of this investigation shed further light into the structure of the large scales at the boundary layer edge in an APG boundary layer. The shape, eccentricity, and inclination of the conditionally averaged APG structures are uniquely shown in 3-D in this chapter to give insight to the APG turbulent boundary layer. This work shows the distinct difference and separation of the intensity in the outer region from the fluid closer to the wall in an APG but still attached flow which has not been shown previously. This chapter also illustrates the difficulty in drawing conclusions of 3-D features from 2-D measurements as features that have the same 2-D cross-sectional area and shape are considerably different when looking at the full 3-D volume. While not in the scope of this dissertation, valuable insight into the possible preferential alignment and organization of large scale features could be shown through similar 3-D flow visualization with a larger field of view than in this chapter. Similar conditional averaging using quantitative 3-D measurements such as tomo-PIV or plenoptic PIV would also be useful for comparison to the results presented in this chapter as the use of these newer 3-D techniques arises and begins to allow for measurements of larger fields of view.

Chapter 7

Contributions and Conclusions

This dissertation described the experimental investigation of the adverse pressure gradient turbulent boundary layer. Three separate experiments were carried out to validate and apply a three-dimensional flow visualization technique to examine the large scale motions in an adverse pressure gradient turbulent boundary layer. An experiment using simultaneous 3-D flow visualization with 2-D velocity measurements was described in Chapter 4 as a first attempt at examining a zero pressure gradient turbulent boundary layer. Secondly, an in-depth look at the connection between flow visualization and velocity measurements in 2-D is described in Chapter 5. Chapter 6 described a 3-D flow visualization experiment on a ZPG and two APG turbulent boundary layers detailing the difference in the large scale structures in the flows.

An initial flow visualization with simultaneous particle image velocimetry measurements were described in an attempt to further validate flow visualization measurements. This flow visualization technique had been attempted in this lab prior to this, but the validity of the flow visualization marking the features of the flow were not fully known. This simultaneous experiment was a first step in making a connection between the flow visualization and velocity. The smoke seeded in the turbulent boundary layer appeared to fill the boundary layer and the extent of the smoke and the extent of the boundary layer corresponded to the same location. The area of seeded flow in the flow visualization and the area of vorticity (inside the boundary layer) were in good agreement. To our knowledge, no three-dimensional flow visualization had simultaneously been complemented with two-dimensional PIV before this experiment. While this experiment proved a good starting point in examining the accuracy of the flow visualization, there were still some improvements which could be implemented

to better understand the flow. First, a more in-depth look at the connection between flow visualization, velocity, and vorticity could be carried out. Also, higher resolution cameras could be used and a larger field of view would be useful in examining the large scale motions and their possible organization. Also, an adverse pressure gradient turbulent boundary layer flow could be examined.

The second experiment detailed in this disseration is on the relationship between image intensity and velocity in a turbulent boundary layer seeded with smoke particles. This was a two-dimensional attempt at looking at flow visualization and velocity from the exact same images - at the exact same time frame to compare the two. The boundary layer was seeded with just enough smoke particles to fill the area for flow visualization but also distinguish the particles for quality PIV measurements. This experiment had not been detailed in literature before. A direct correlation of velocity intensity did show a correlation between low speed fluid and higher intensity flow. This was not a one-to-one connection, but was a regular presence in the data. An attempt to directly estimate a velocity field from the correlations and the flow visualization data proved useful for some data sets, but for others, the estimations were inaccurate compared to the true velocity measurements. A novel complementary proper orthogonal decomposition and linear stochastic estimation approach was constructed to use only the large scale features of both flow visualization and velocity in an attempt to connect the structures in the smoke and velocity measurements. Using the POD/LSE correlations to estimate velocity from flow visualization filtered out the small scale features and many times did estimate the velocity field roughly similar to the true velocity field. However, on many occasions the estimations were erroneous. This experiment proved a good attempt at making a connection that had not been made before.

Overall, the investigation led to a few main conclusions. First, the connection between high intensity fluid and low velocity flow was detailed, but the relationship was not strong enough to accurately estimate the velocity field given a flow visualization field. However, the current flow visualization technique did prove useful in identifying the true boundary

layer edge from velocity measurements. Also, the larger structures in the intensity of the flow could be confirmed to be the true large scale features apparent in the velocity fields. Thus, the flow visualization could be used for examination of large scale features in the outer region of the turbulent boundary layer.

The final experiment detailed in this dissertation is a three-dimensional flow visualization for the comparison of the large scale features in the zero pressure gradient and adverse pressure gradient turbulent boundary layer. A state of the art scanning flow visualization technique was used to look at a large volume in the ZPG and APG turbulent boundary layers. To our knowledge, the 3-D flow visualization of this large a volume with a high resolution camera has not been attempted before. The lack of information about the 3-D features and possible alignment in the outer region of the APG boundary layer led to the need of this experiment and illustrates its uniqueness. Investigation of the flow visualization volumes showed that features in the ZPG turbulent boundary layer were larger and more uniform. The ZPG features were also more inclined from the wall compared to the APG features. Investigation of the binary images and power spectral density confirmed that the ZPG structures were larger.

Conditional averaging of a structure at a certain wall-normal height showed that the fluid was disconnecting from the wall in the APG cases, though no signs of flow separation were found in the data. For the APG cases, the fluid in the outer region was decorrelated compared to the fluid closer to the wall. This decorrelation was greater with increasing height. This showed that the features in the ZPG turbulent boundary layer which may look the same as the features in the APG flow are, in fact, part of a larger volume beneath the structure. Whereas, the feature in the APG flow is more disconnected and part of a smaller region of fluid in the outer region. This clearly illustrates the caution needed when investigating 3-D features with 2-D measurements. The features which were similar in 2-D appeared quite different when looking at the volumes in 3-D. Contrary to the findings of Elginsa et al. [29] and Delo and Smits [20] no organization or preferential alignment of

the structures were seen in the 3-D flow visualization volumes or the conditional averaging volumes.

Bibliography

[1] Reynolds, O., "On the Dynamical Theory of Incompressible Viscous Fluids and the Determination of the Criterion," *Phil Trans Roy Soc of London,* 1883.

[2] Kline, S., Reynolds, W.C., Schraub, F.A., and Runstadler, P.W., "The structure of turbulent boundary layers," *J Fluid Mechanics,* Vol 30, 1967.

[3] Corino, E.R., and Brodkey, R.S., "A visual investigation of the wall region in turbulent flow," *J Fluid Mech,* Vol 37, Part 1, 1969.

[4] Willmarth, W.W., "Structure of turbulence in boundary layers," *Advances in Applied Mechanics,* Vol 15, pp 159-254, 1975.

[5] Smith, C. R., Walker, J. D. A., Haidari, A. H., and Sobrun, U., "On the dynamics of near-wall turbulence," textitPhil. Trans.: Phys. Sci. Engng., Vol 336, pp. 131-175, 1991.

[6] Corrsin, S., and Kistler, A.L., "The free-stream boundaries of turbulent flows," NACA, TN-3133, TR-1244, pp 1033-1064, 1954.

[7] Fiedler, H., and Head, M. R., "Intermittency measurements in the turbulent boundary layer," textitJ. Fluid Mech., Vol 25, pp. 719-735, 1966.

[8] Kovasznay, L.S.G., Kibens, V., and Blackwelder, R.F., "Large-scale motion in the intermittent region of a turbulent boundary layer," *J Fluid Mech,* Vol 41, pp. 283-325, 1970.

[9] Townsend, A. A., "Entrainment and the structure of turbulent flow," textitJ. Fluid Mech., Vol 41, pp. 13-46, 1970.

[10] Kim, K.C., and Adrian, R.J., "Very large-scale motion in the outer layer," *Phys Fluids,* Vol 11, pp. 417-422, 1999.

[11] Theodorsen, T., "Mechanisms of Turbulence," *Proc. 2nd Midwestern Conference on Fluid Mechanics,* 1952.

[12] Townsend, A.A., *The structure of turbulent shear flow,* Cambridge University Press, 2nd edition, 1956.

[13] Head, M. R., and Bandyopadhyay, P., "New Aspects of Turbulent Boundary-Layer Structure," *Journal of Fluid Mechanics,* Vol. 107, pp. 297-338, 1981.

[14] Robinson, S.K., "Coherent Motions in the Turbulent Boundary Layer," *Ann. Rev. Fluid Mech.,* Vol. 23, pp. 601-639, 1991.

[15] Falco, R.E., "A coherent structure model of the turbulent boundary layer and its ability to predict Reynolds number dependence," *Phil. Trans. R. Soc. Lond,* Vol 336, pp 103-129, 1991.

[16] Perry, A.E., Henbest, S., and Chong, M.S., "A theoretical and experimental study of wall turbulence," *J. Fluid Mech.,* Vol 165, pp 163-199, 1986.

[17] Townsend, A. A., textitThe Structure of Turbulent Shear Flow, Cambridge: Univ. Press 429 pp. 2nd ed. 1976.

[18] Adrian, R. J., "Hairpin vortex organization in wall turbulence," *Phys. Fluids,* Vol. 19, 041301, 2007

[19] Harun, Z., Monty, J., and Marusic, I., "The structure of zero, favorable, and adverse pressure gradient turbulent boundary layers," textitExperimental Techniques, pp 1-6, 2010.

[20] Delo, C., and Smits, A.J., "Volumetric visualization of coherent structure in a low Reynolds number turbulent boundary layer," *International Journal of Fluid Dynamics,* Vol. 1, 1997.

[21] Perry, A.E., and Chong, M.S., "On the mechanism of wall turbulence," *J. Fluid Mech.,* Vol 199, pp 173-217, 1982.

[22] Ganapathisubramani, B., Longmire, E.K., and Marusic, I., "Characteristics of vortex packes in turbulent boundary layers," *J. Fluid Mech.,* Vol 478, pp 35-46, 2003.

[23] Marusic, I., "On the role of large-scale structures in wall turbulence," *Phys Fluids,* Vol 13, pp. 735-743, 2001.

[24] Bogard, D. G., and Tiederman, W. G., "Burst detection with single-point velocity measurements," textitJ. Fluid Mech., Vol 162 pp 389, 1986.

[25] Adrian, R.J., Meinhart, C.D., and Tomkins, C.D., "Vortex organization in the outer region of the turbulent boundary layer," *J. Fluid Mech.,* Vol 422, pp 1-54, 2000.

[26] Tomkins, C.D., "The structure of turbulence over smooth and rough walls," Ph.D. Thesis, University of Illinois, Urbana-Champaign, 2001.

[27] Balakumar, B. J., and Adrian, R. J., "Large- and very-large-scale motions in channel and boundary-layer flows," *Philos Trans R Soc A,* Vol 365, pp. 665-681, 2007.

[28] Marusic, I., McKeon, B.J., Monkewitx, P.A., Nagib, H.M., Smits, A.J., and Sreenivisan, K.R., "Wall-bounded turbulent flows at high Reynolds number: recent advances and key issues," *Phys. Fluids,* Vol. 22:065103, 2010.

[29] Elsinga, G.E., Adrian, R.J., van Oudheusden, B.W., and Scarano, F., "Three-dimensional vortex organization in a high-Reynolds-number supersonic turbulent boundary layer," *J. Fluid Mech.,* Vol. 644, pp 35-60, 2010.

[30] Wilcox, D., *Turbulence Modeling for CFD,* DCW Industries, La Canada, California, 1993.

[31] Watmuff, J.H., "An experimental investigation of low Reynolds number turbulent boundary layer subject to an adverse pressure gradient," *Annual Research Briefs,* NASA/Stanford Center for Turbulent Research, 1989.

[32] Lian, Q.X., "A visual study of the coherent structure of the turbulent boundary layer in flow with adverse pressure gradient," *Journal of Fluid Mechanics*, Vol. 215, pp. 101-124, 1990.

[33] Nagano, Y., Tagawa, M., and Tsuji, T., "Effects of adverse pressure gradients on mean flows and turbulence statistics in a boundary layer," *Turbulent Shear Flows,* Vol 8, Springer, Berlin, pp 7-21, 1993.

[34] Krogstad, P., and Skare, P., "Influence of a strong adverse pressure gradient on the turbulent structure in a boundary layer," *Phys. Fluids,* Vol. 7, 1995.

[35] Nagano, Y., Tsuji, T., and Houra, T., "Structure of turbulent boundary layer subjected to adverse pressure gradient," *International Journal of Heat and Fluid Flow,* vol. 19, pp. 563-572, 1998.

[36] Tulapurkara, E. G., Khoshnevis, A. B., and Narasimhan, J. L., "Wakeboundary layer interaction subject to convex and concave curvatures and adverse pressure gradient," *Exp. Fluids,* Vol 31, pp. 697-707, 2001.

[37] Alving, A. E., and Fernholz, H. H., "Turbulence measurements around a mild separation bubble and downstream of reattachment," *J. Fluid Mech.,* Vol 322, pp. 297328, 1996.

[38] Clauser, F. H., "Turbulent Boundary Layers in Adverse Pressure Gradients," *J. Aeronaut. Sci.,* Vol 21, pp. 91-108, 1954.

[39] Bradshaw, P., "The turbulence structure of equilibrium boundary layers," *J. Fluid Mech.,* Vol 29, pp. 625645, 1967.

[40] Goldstein, J. E., and Smits, A. J., "Flow visualization of the three-dimensional, time-evolving structure of a turbulent boundary layer," *Phys. Fluids,* Vol. 6, pp. 577-587, 1994.

[41] Lee, J. H., and Sung, H. J., "Effects of an adverse pressure gradient on a turbulent boundary layer," *International Journal of Heat and Fluid Flow,* vol. 29, pp. 568-578, 2008.

[42] Marusic, I., and Perry, A.E., "A wall wake model for the turbulent structure of boundary layers," *J. Fluid Mech.,* Vol. 298, pp 389-407, 1995.

[43] Finnicum, D.S., and Hanratty, T.J., "Effect of favourable pressure gradients on turbulent boundary layers," *AIChE J.,* Vol 34(4), pp 529-540, 1988.

[44] Simpson, R. L., "Turbulent boundary-layer separation," *Ann. Rev. Fluid Mech.,* Vol. 21(1), pp. 205-232, 1989.

[45] Praturi, A.K., and Brodkey, R.S., "A stereoscopic visual study of coherent structures in turbulent shear flow," *Journal of Fluid Mechanics,* Vol. 89, pp. 251-272, 1978.

[46] Smits, A.J. and Delo, C. "Self-Sustaining Mechanisms of Wall Turbulence", In Coherent Structures in Complex Systems, Lecture Notes in Physics, pp. 17-38, Springer, 2002.

[47] Hutchins, N., Hambleton, W.T., and Marusic, I., "Inclined cross-stream stereo particle image velocimetry measurements in turbulent boundary layers," *J Fluid Mech,* Vol 541, pp. 21-54, 2005.

[48] van Dyke, M., *An Album of Fluid Motion,* The Parabolic Press, 1982.

[49] Hussain, A. K. M. F., "Role of coherent structures in turbulent shear flows," textitProc. Indian Acad. Sci. (Engng. Sci.), Vol 4, pp. 129-175, 1981.

[50] Talmon, A.J., Kunen, J.M.G., and Ooms, G., "Simultaneous flow visualization and Reynolds-stress measurement in a turbulent boundary layer," *J. Fluid Mech.,* Vol 163, pp 459-478, 1986.

[51] Westerweel, J., Hoffmann, T., Fukushima, C., and Hunt, J.C.R., "The turbulent/non-turbulent interface at the outer boundary of a self-similar turbulent jet," *Exp Fluids,* Vol 33, pp. 873-878, 2002.

[52] Bisset, D. K., Hunt, J. C. R., and Rogers, M. M., "The turbulent/non-turbulent interface bounding a far wake," *J Fluid Mech,* Vol 451, pp. 383-410, 2002.

[53] Prasad, R.R., and Sreenivisan, K.R., "Scalar interfaces in digital images of turbulent flows," *Exp. Fluids,* Vol. 7, pp. 259-264, 1989.

[54] Delo, C., Kelso, R., and Smits, A. J., "Three-dimensional structure of a low Reynolds number turbulent boundary layer," *J Fluid Mech,* Vol 512, pp. 47-83, 2004.

[55] Taylor, G.I., "The spectrum of turbulence," *Proc. R. Soc. London A,* Vol 164, pp 476-490, 1938.

[56] Dennis, D.J.C., and Nickels, T.B., "Experimental measurement of large-scale three dimensional structures in a turbulent boundary layer. Part 2. Long structures," *J. Fluid Mech.,* Vol 673, pp 218-244, 2011.

[57] Elsinga, G.E., and Ganapathisubramani, B., "Advances in 3D velocimetry," *Meas. Sci. Technol,* Vol. 24:020301, 2013.

[58] Westerweel, J., Elsinga, G.E., and Adrian, R.J., "Particle image velocimetry for complex and turbulent flows," *Annu. Rev. Fluid Mech.,* Vol. 45, pp 409-436, 2013.

[59] Brcker, C., Hess, D., and Kitzhofer, J., "Single-view volumetric PIV via high-resolution scanning, isotropic voxel restructuring and 3D least-squares matching (3D-LSM)," *Meas Sci Technol,* 24:024001, 2013.

[60] Lumley, J.L., The structure of inhomogeneous turbulence. In: *Atmospheric Turbulence and Wave Propagation,* ed. A. M. Yaglom, V. I. Tatarski, pp 166-178, 1967.

[61] Sirovich, L., "Turbulence and the dynamics of coherent structures. Part I: Coherent structures," *Q Appl Math,* Vol 45, pp. 561-571, 1977.

[62] Antonia, R. A., "Conditional sampling in turbulence measurement," textitAnn. Rev. Fluid Mech., Vol 13 pp 131-156, 1981.

[63] Wernet, M. P., "Symmetric phase only filtering: a new paradigm for DPIV data processing," textitMeas. Sci. Technol., Vol 16, pp. 601-618, 2005.

[64] Garcia, D., "A fast all-in-one method for automated post processing of PIV data," *Exp Fluids,* Vol 50, pp. 1247-1259, 2010.

[65] Kendall, A. and Koochesfahani, M., "A method for estimating wall friction in turbulent wall-bounded flows," *Exp Fluids,* Vol 44, pp 773-780, 2008.

[66] Holzner, M., Liberzon, A., Guala, M., and Tsinober, A., "Generalized detection of a turbulent front generated by an oscillating grid," *Exp Fluids,* Vol 41, pp. 711-719, 2006.

[67] Melnick, M.B., and Thurow, B., "On the relationship between image intensity and velocity in a turbulent boundary layer seeded with smoke particles," *Exp. Fluids,* Vol 55(2), 2014.

[68] Thurow, B., and Lynch, K., "Development of a high-speed three dimensional flow visualization technique," *AIAA Journal,* Vol. 47, pp. 2857-2865, 2009.

[69] Thurow, B., Jiang, N., and Lempert, W., "Review of ultra-high repetition rate laser diagnostics for fluid dynamic measurements," *Meas. Sci. Technol.,* Vol. 24, pp. 1-22, 2013.

[70] Stratford, B.S., "Prediction of Separation of a Turbulent Boundary Layer," *Journal of Fluid Mechanics,* Vol. 5 No. 1, pp. 1-16, 1959.

[71] Aubertine, C. D., and Eaton, J. K., "Turbulence development in a non-equilibrium turbulent boundary layer with mild adverse pressure gradient," *J. Fluid Mech.,* Vol 532, pp. 345-364, 2005.

[72] Panton, R.L., "Overview of the self-sustaining mechanisms of wall turbulence," *Prog. Aero. Sci., Vol. 37,* pp. 341-383, 2001.

[73] van Doorne, C.W.H., and Westerweel, J., "Measurement of laminar, transitional, and turbulent pipe flow using stereoscopic-PIV," *Exp. Fluids,* Vol. 42, pp 259-279, 2007.

[74] Bonnet, J.P., Cole, D.R., Delville, J., Glauser, M.N., and Ukeiley, L.S., "Stochastic estimation and proper orthogonal decomposition: Complementary techniques for identifying structure," *Exp Fluids,* Vol 17, pp. 307-314, 1994.

[75] Dennis, D. J. C., and Nickels, T. B., "On the limitations of Taylor's hypothesis in constructing long structures in a turbulent boundary layer," *J Fluid Mech,* Vol 614, pp. 197-206, 2008.

[76] Lee, J.H., and Sung, H.J., "Comparison of very-large-scale motions of turbulent pipe and boundary layer simulations," *Phys Fluids,* 25:045103, 2013.

[77] Zhou, J., Adrian, J., Balachandar, S., and Kendall, T.M., "Mechanisms for generating coherent packets of hairpin vortices in channel flow," *J. Fluid Mech.,* Vol 387, pp 353-396, 1999.

Appendices

Appendix A

Proper Orthogonal Decomposition Modes

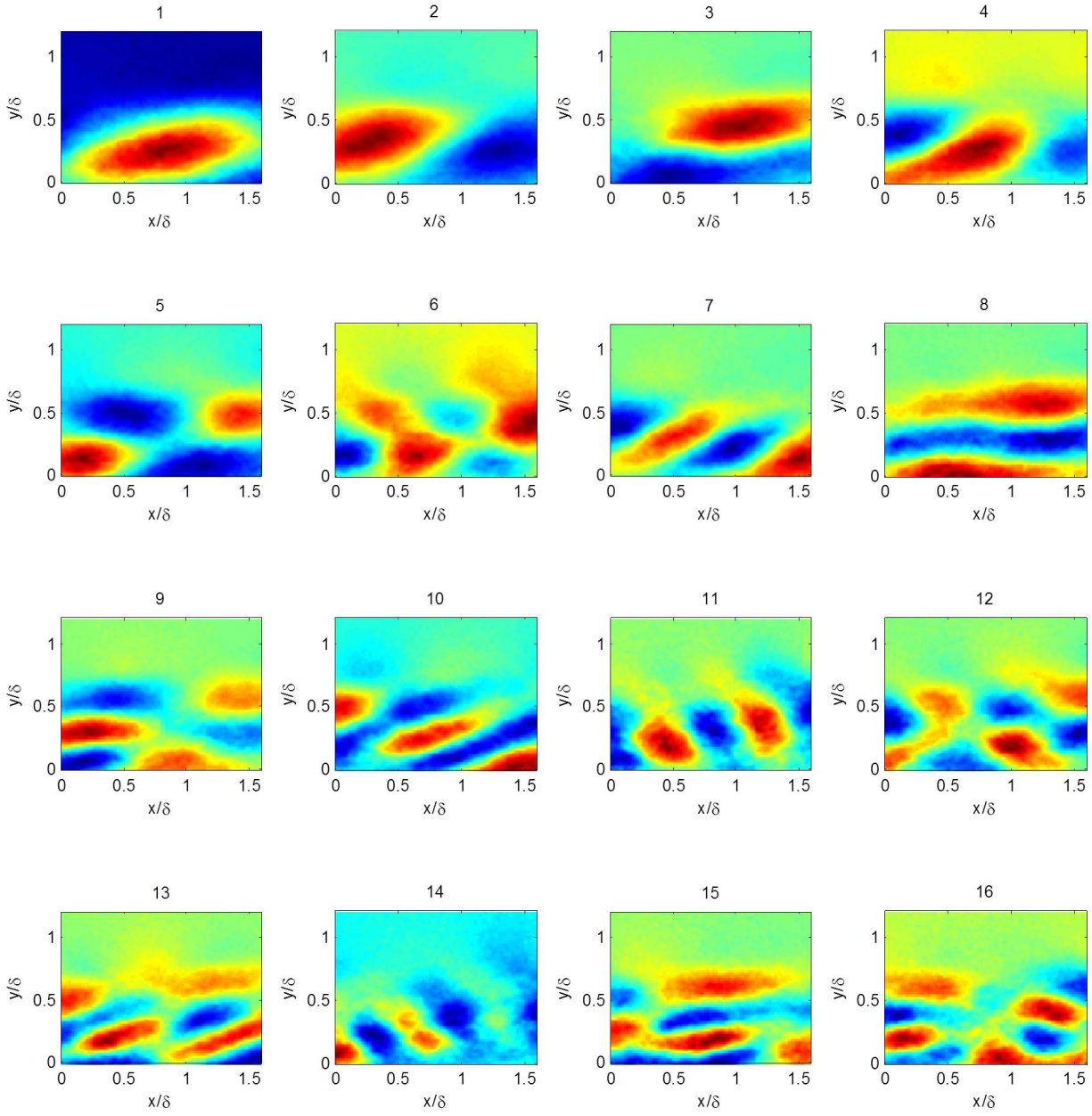

Figure A.1: First 16 velocity modes (streamwise velocity) at Location A with slit covered

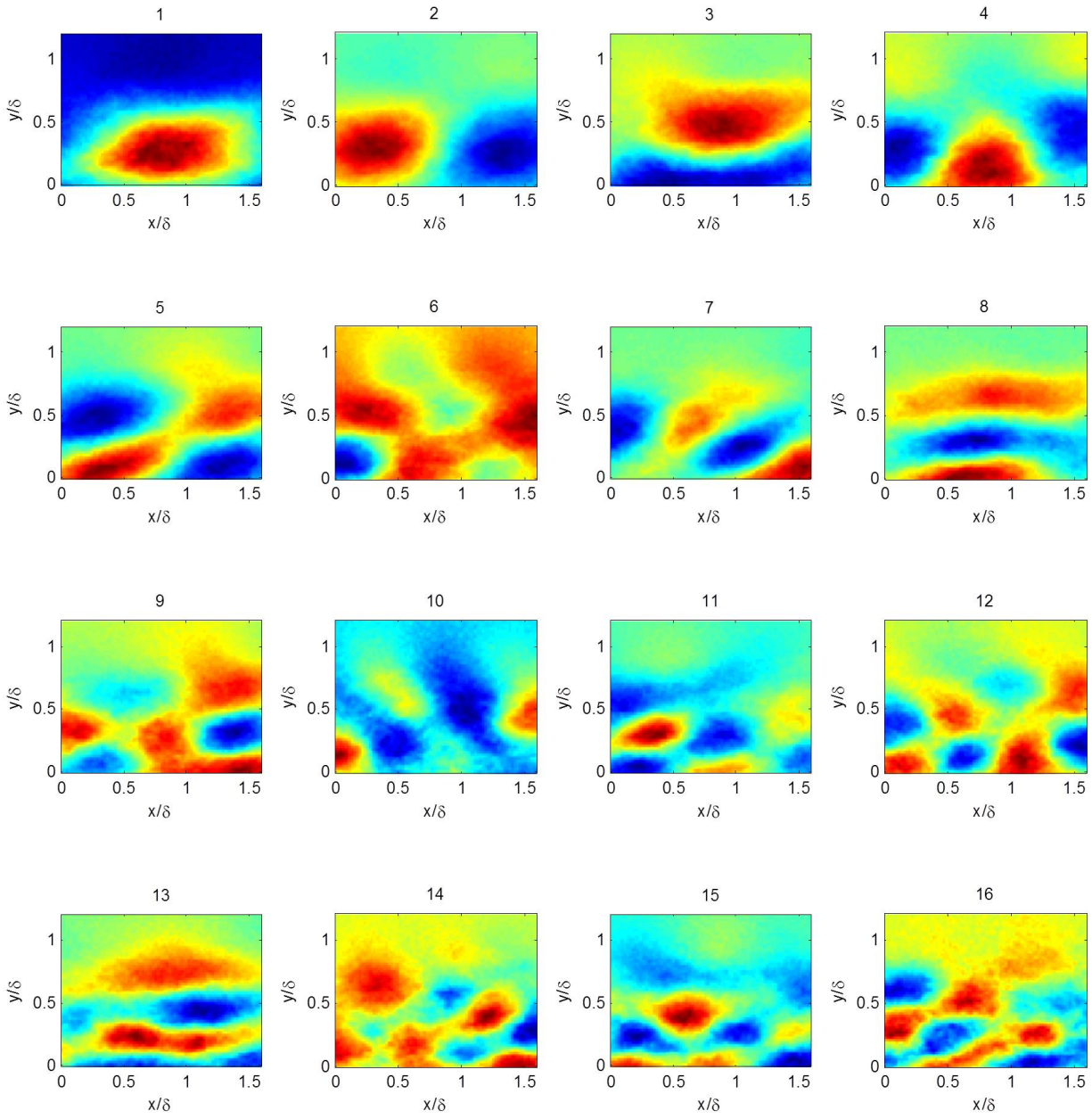

Figure A.2: First 16 velocity modes (streamwise velocity) at Location A with slit uncovered but no smoke

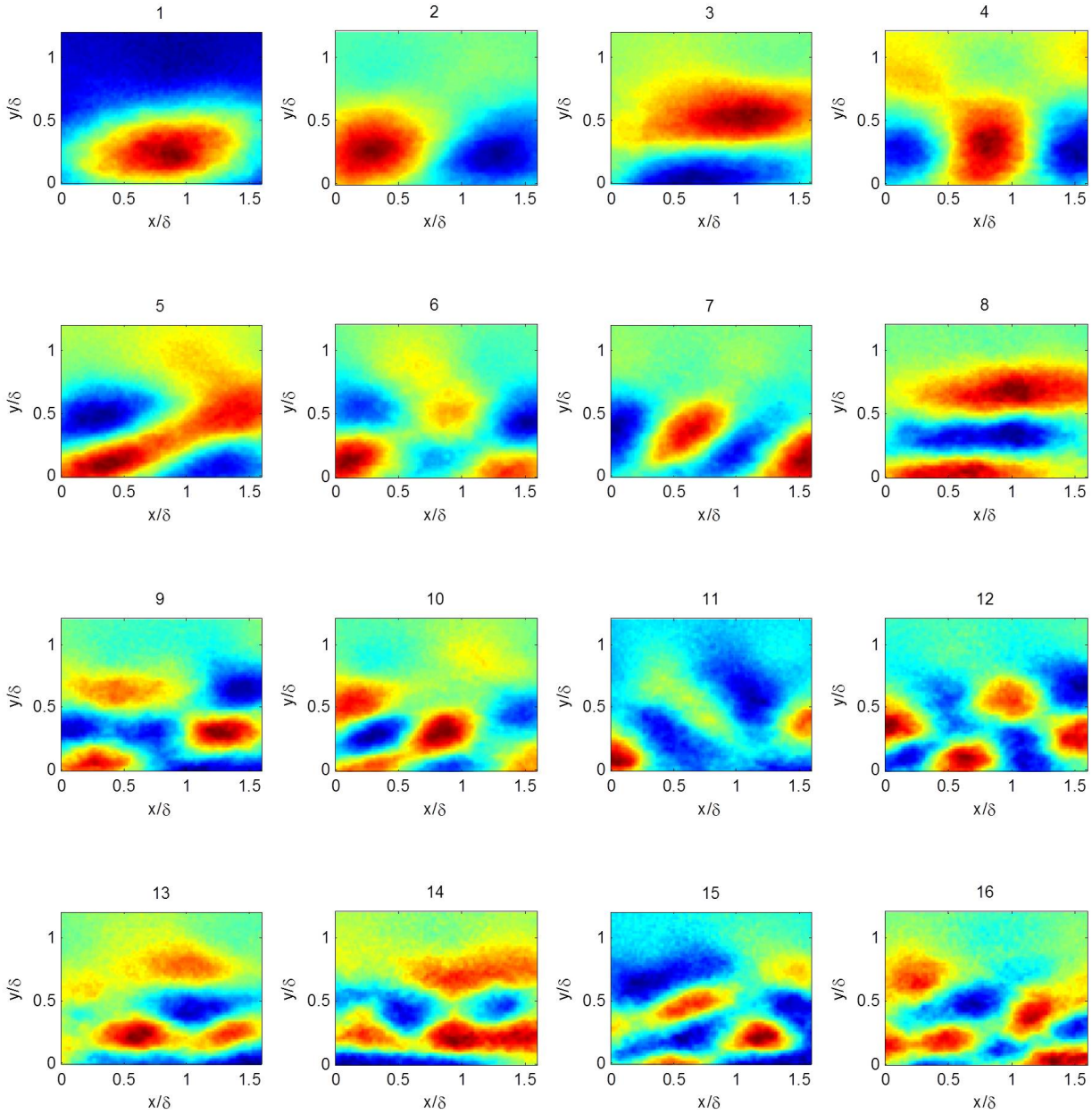

Figure A.3: First 16 velocity modes (streamwise velocity) at Location A with slit uncovered and smoke injected

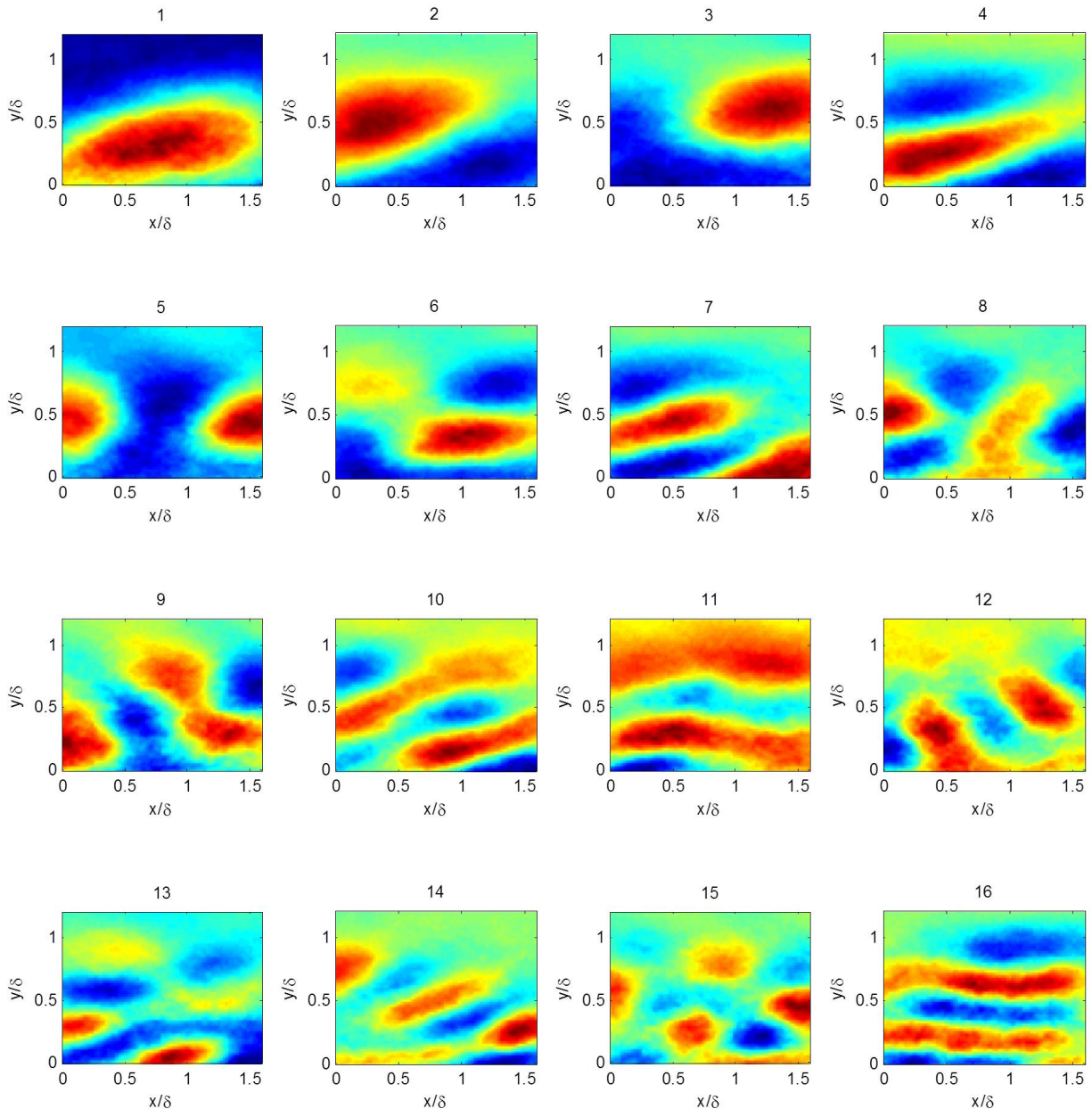

Figure A.4: First 16 velocity modes (streamwise velocity) at Location B with slit covered

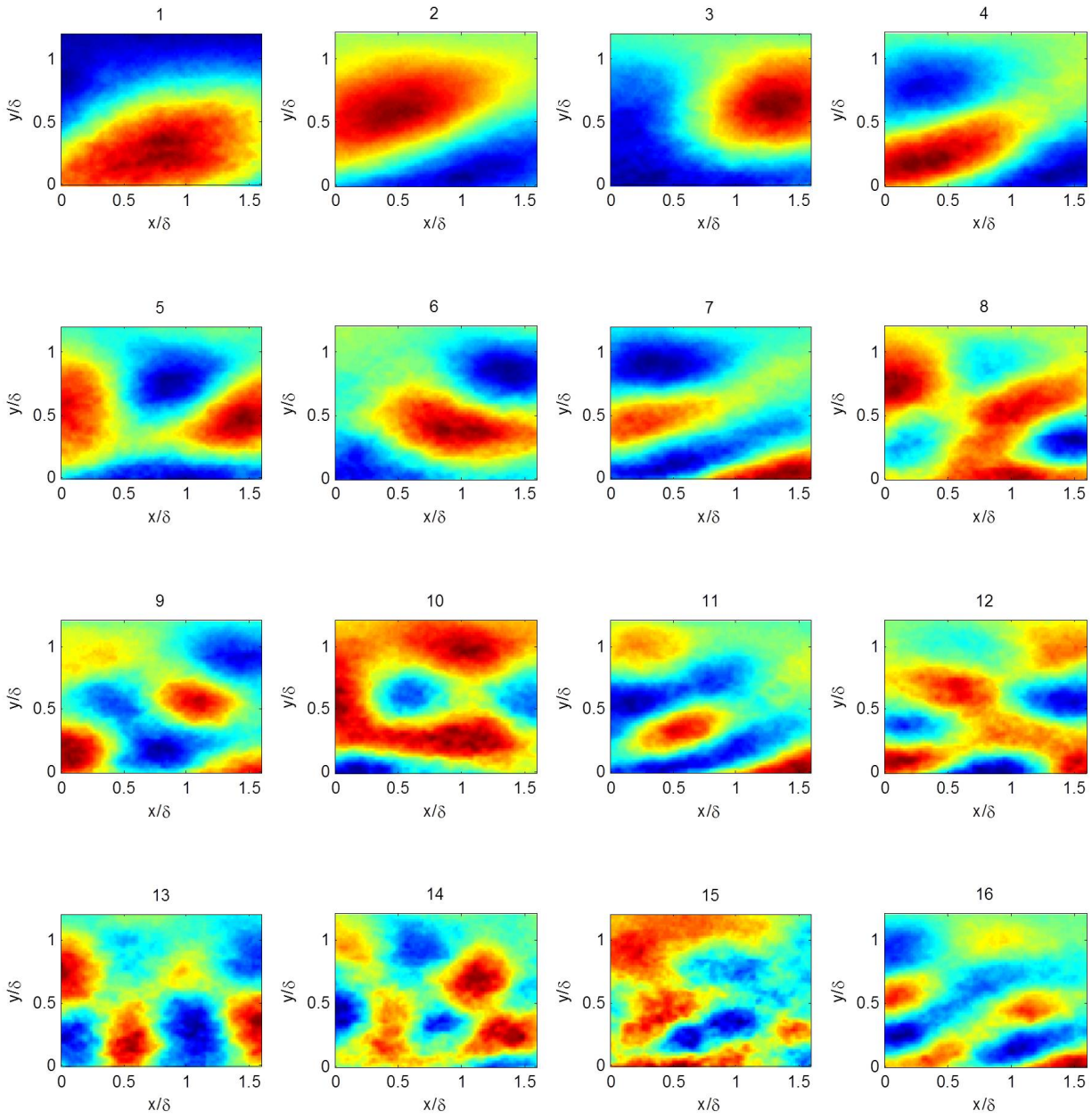

Figure A.5: First 16 velocity modes (streamwise velocity) at Location B with slit uncovered but no smoke

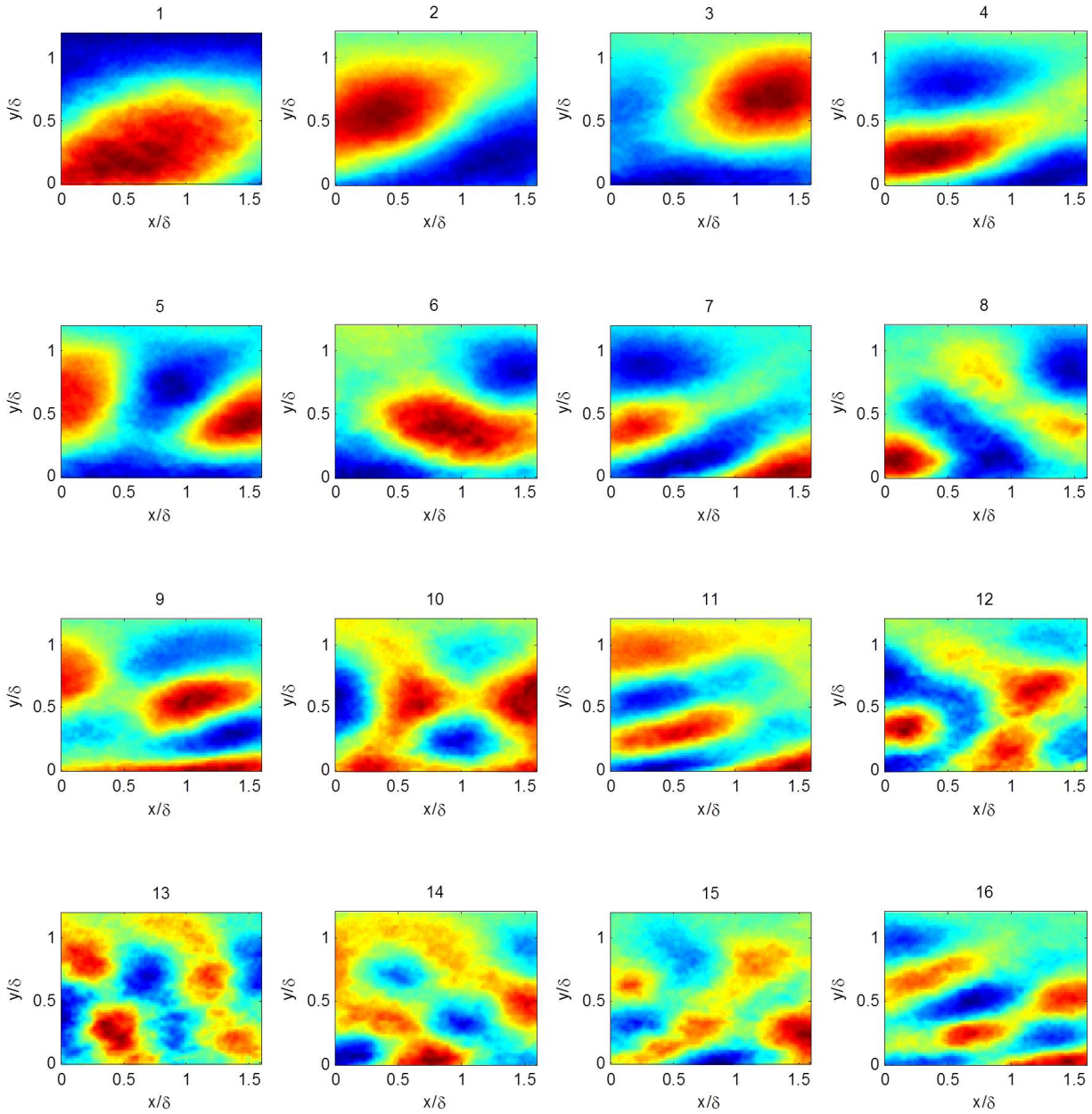

Figure A.6: First 16 velocity modes (streamwise velocity) at Location B with slit uncovered and smoke injected

Appendix B

Correlation Coefficients

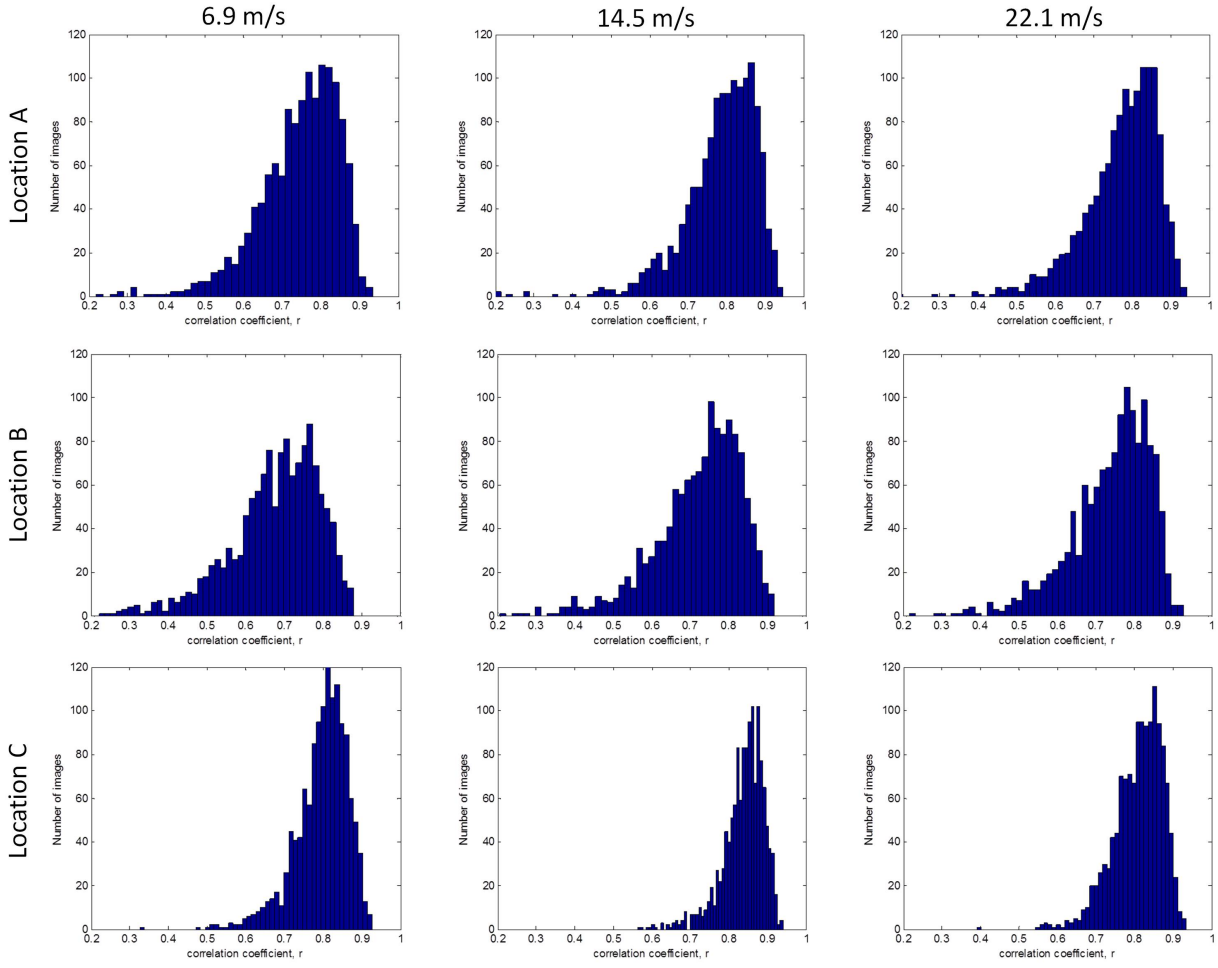

Figure B.1: Histogram of correlation coefficients at Locations A, B, C, at freestream velocities of 6.9m/s, 14.5m/s, and 22.1m/s

Appendix C

Pressure Measurements

Table C.1: Change in pressure (in H_20) between each pressure port on top of wind tunnel for ramp 1, averaged over 7 tests

	ΔP (in H_2O)							
Ports	Test 1	Test 2	Test 3	Test 4	Test 5	Test 6	Test 7	Average
1-2	0.0559	0.0383	0.0401	0.0531	0.0608	0.0531	0.0471	0.0498
2-3	0.0444	0.0448	0.0481	0.0300	0.0400	0.0376	0.0415	0.0409
3-4	0.0360	0.0413	0.0421	0.0528	0.0464	0.0477	0.0480	0.0449
4-5	0.0384	0.0396	0.0297	0.0350	0.0313	0.0344	0.0352	0.0348
5-6	0.0445	0.0366	0.0459	0.0386	0.0397	0.0355	0.0502	0.0416
								0.0424

Table C.2: Change in pressure (in H_20) between each pressure port on top of wind tunnel for ramp 2, averaged over 7 tests

	ΔP (in H_2O)							
Ports	Test 1	Test 2	Test 3	Test 4	Test 5	Test 6	Test 7	Average
1-2	0.0533	0.0521	0.0555	0.0524	0.0559	0.0563	0.0562	0.0545
2-3	0.0614	0.0608	0.0583	0.0597	0.0597	0.0608	0.0553	0.0594
3-4	0.0466	0.0541	0.0552	0.0442	0.0482	0.0500	0.0570	0.0508
4-5	0.0589	0.0536	0.0438	0.0609	0.0615	0.0520	0.0554	0.0552
5-6	0.0433	0.0455	0.0574	0.0418	0.0403	0.0414	0.0387	0.0441
								0.0528

Appendix D

Conditional averaged structures

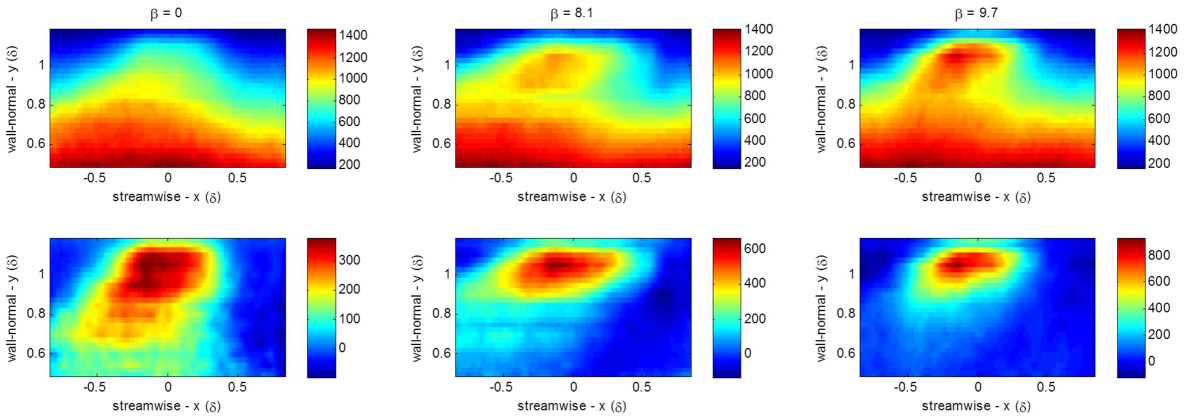

Figure D.1: Conditionally averaged features at y = 1.1δ with a diameter between 0.75δ and 1.0δ a) streamwise/wall-normal slice and b) streamwise/wall-normal slice with mean subtracted.

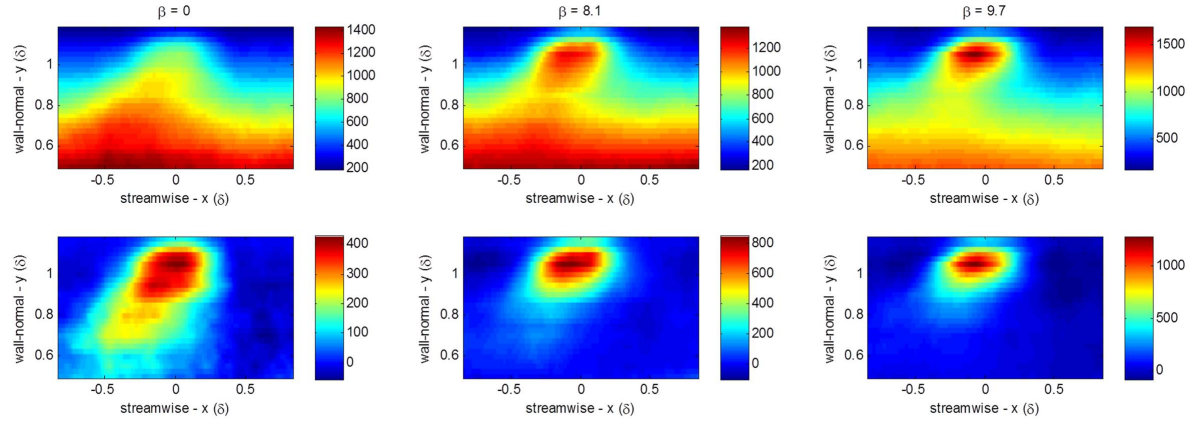

Figure D.2: Conditionally averaged features at y = 1.1δ with a diameter between 0.5δ and 0.75δ a) streamwise/wall-normal slice and b) streamwise/wall-normal slice with mean subtracted.

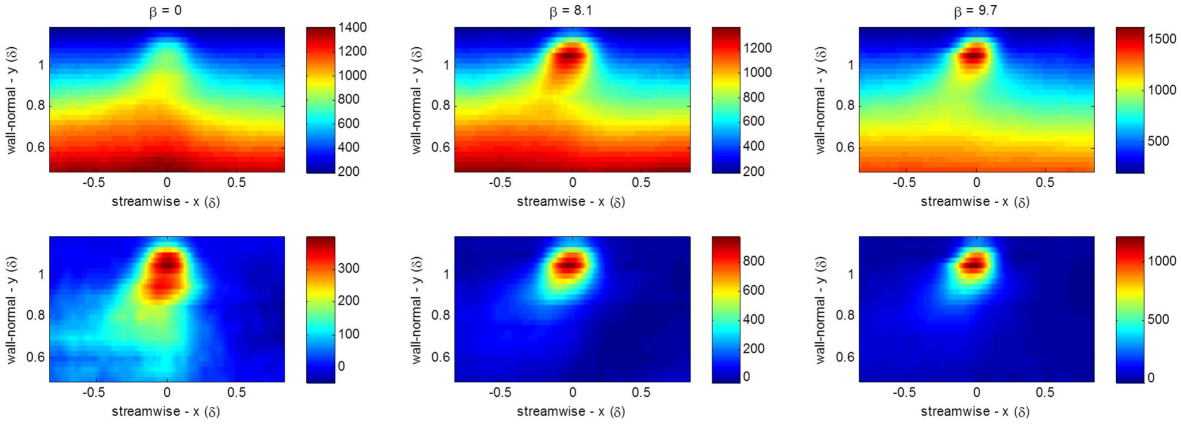

Figure D.3: Conditionally averaged features at y = 1.1δ with a diameter between 0.25δ and 0.5δ a) streamwise/wall-normal slice and b) streamwise/wall-normal slice with mean subtracted.

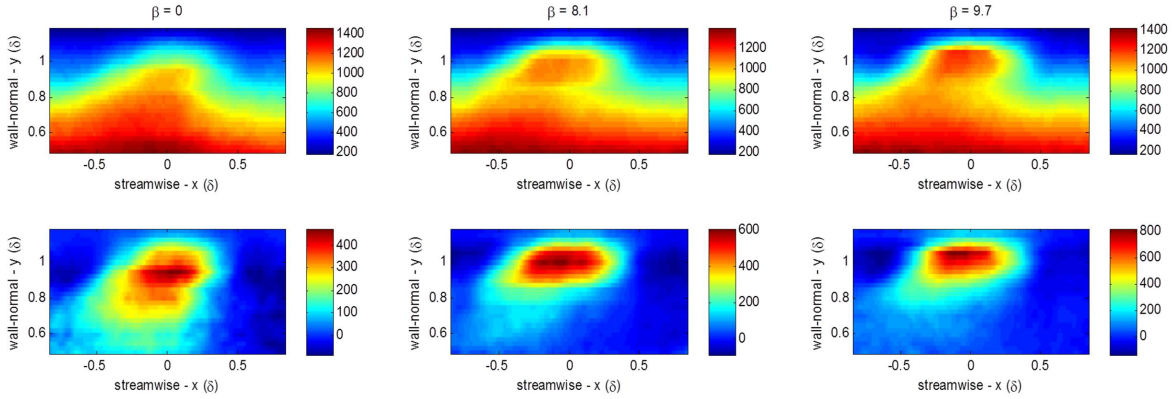

Figure D.4: Conditionally averaged features at y = 1.0δ with a diameter between 0.75δ and 1.0δ a) streamwise/wall-normal slice and b) streamwise/wall-normal slice with mean subtracted.

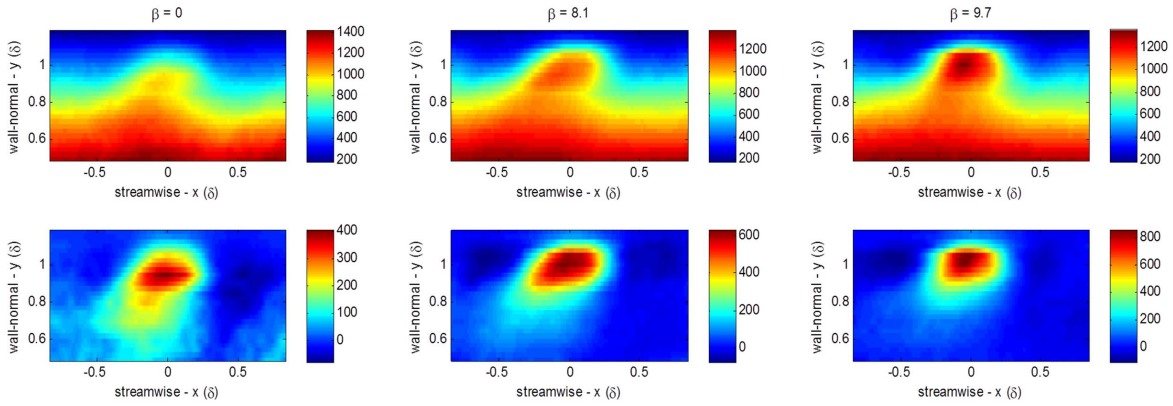

Figure D.5: Conditionally averaged features at y = 1.0δ with a diameter between 0.5δ and 0.75δ a) streamwise/wall-normal slice and b) streamwise/wall-normal slice with mean subtracted.

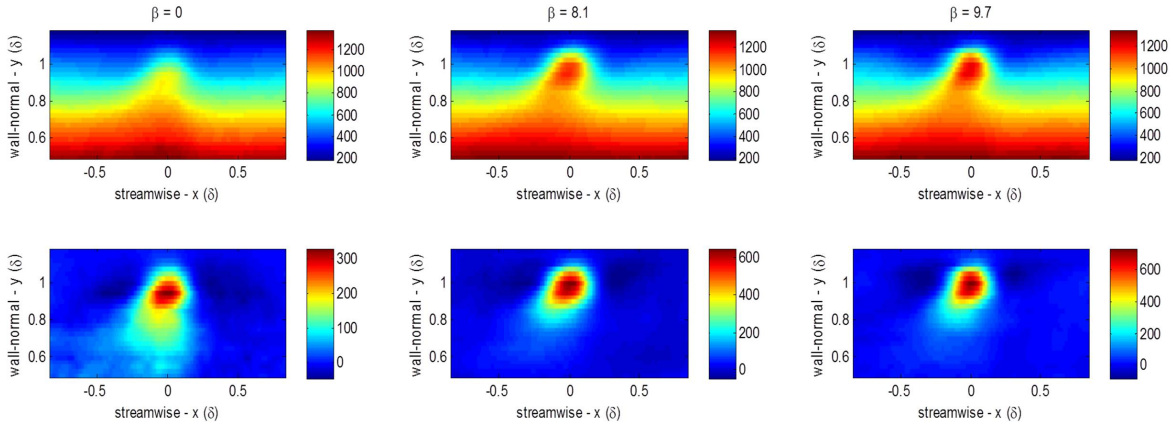

Figure D.6: Conditionally averaged features at y = 1.0δ with a diameter between 0.25δ and 0.5δ a) streamwise/wall-normal slice and b) streamwise/wall-normal slice with mean subtracted.

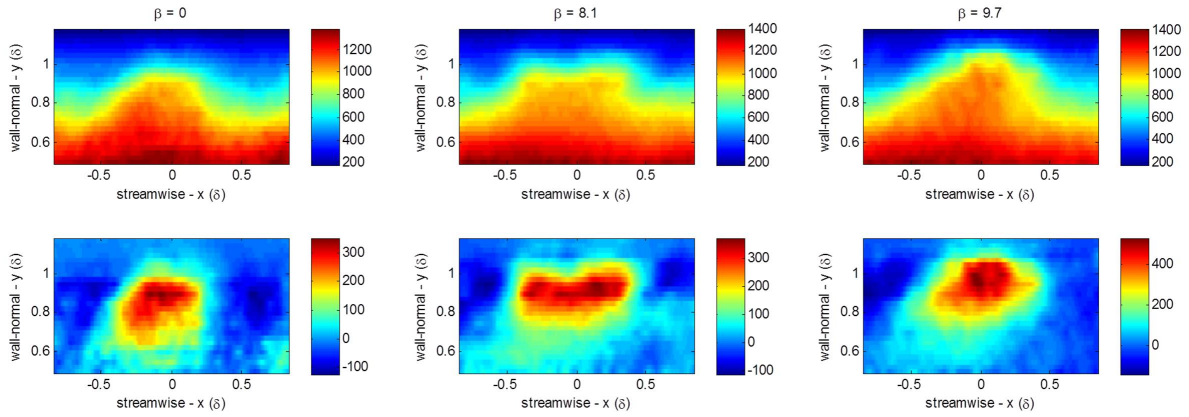

Figure D.7: Conditionally averaged features at y = 0.9δ with a diameter between 0.75δ and 1.0δ a) streamwise/wall-normal slice and b) streamwise/wall-normal slice with mean subtracted.

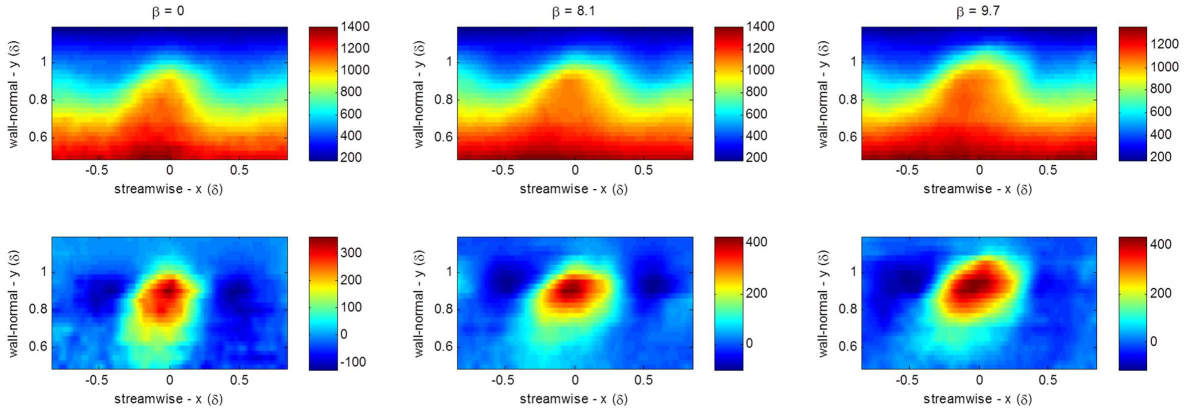

Figure D.8: Conditionally averaged features at y = 0.9δ with a diameter between 0.5δ and 0.75δ a) streamwise/wall-normal slice and b) streamwise/wall-normal slice with mean subtracted.

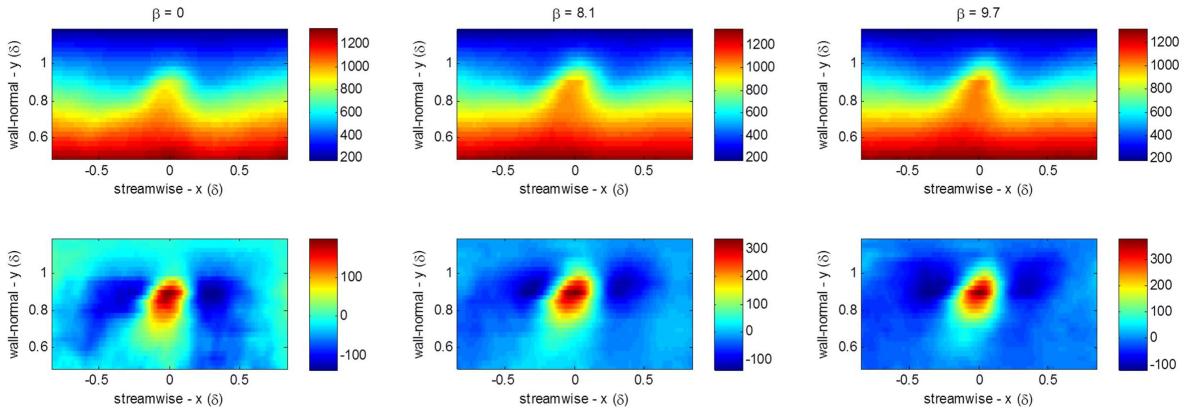

Figure D.9: Conditionally averaged features at y = 0.9δ with a diameter between 0.25δ and 0.5δ a) streamwise/wall-normal slice and b) streamwise/wall-normal slice with mean subtracted.

Appendix E

Conditional averaged valleys

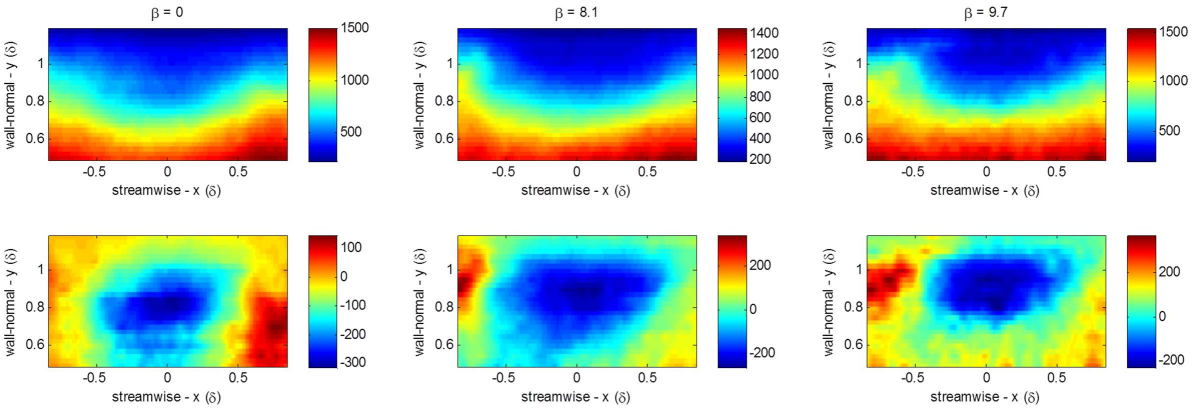

Figure E.1: Conditionally averaged features at y = 0.8δ with a diameter between 0.75δ and 1.0δ a) streamwise/wall-normal slice and b) streamwise/wall-normal slice with mean subtracted.

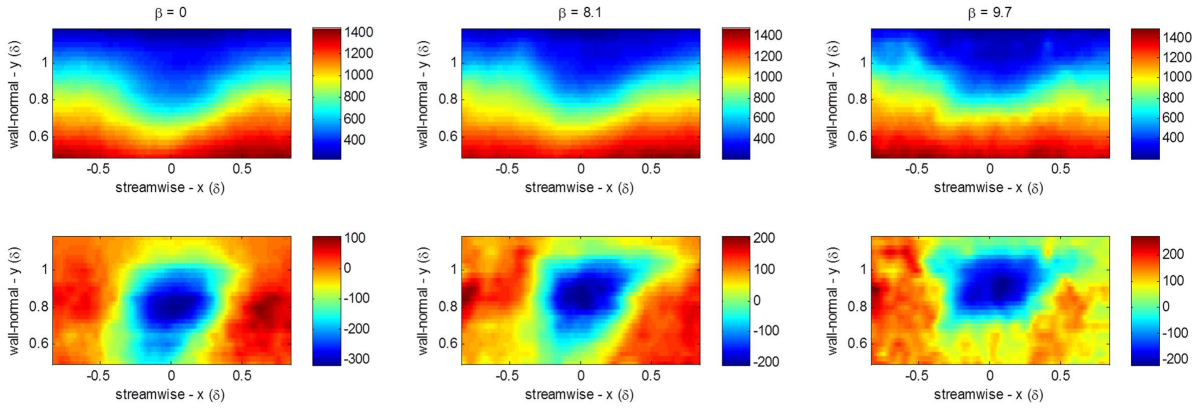

Figure E.2: Conditionally averaged features at y = 0.8δ with a diameter between 0.5δ and 0.75δ a) streamwise/wall-normal slice and b) streamwise/wall-normal slice with mean subtracted.

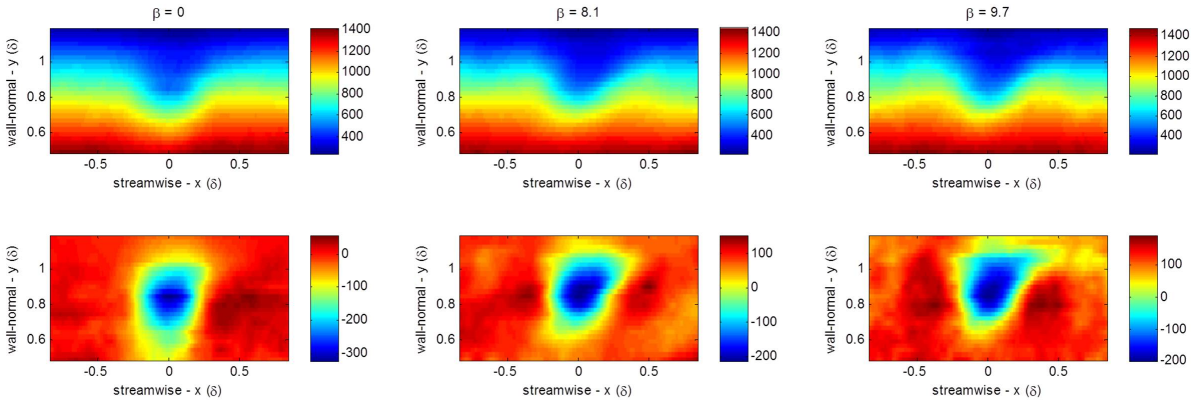

Figure E.3: Conditionally averaged features at y = 0.8δ with a diameter between 0.25δ and 0.25δ a) streamwise/wall-normal slice and b) streamwise/wall-normal slice with mean subtracted.

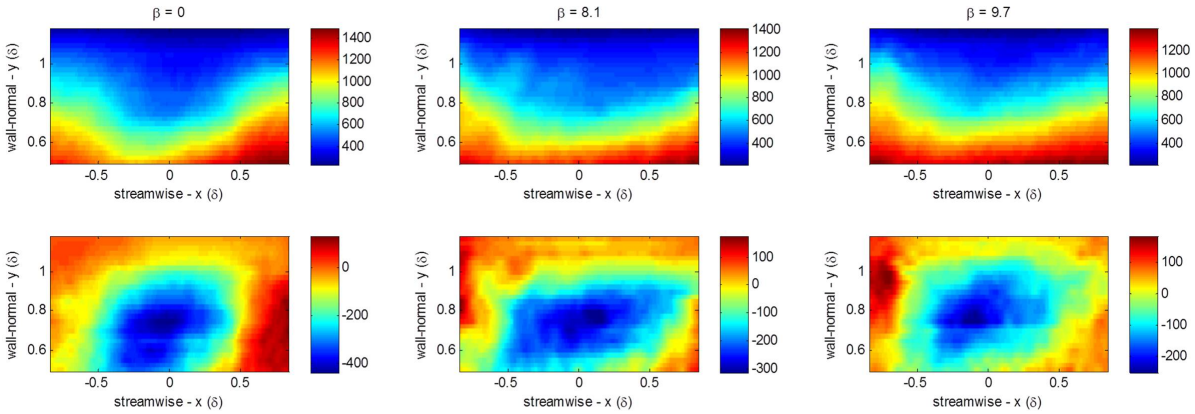

Figure E.4: Conditionally averaged features at y = 0.7δ with a diameter between 0.75δ and 1.0δ a) streamwise/wall-normal slice and b) streamwise/wall-normal slice with mean subtracted.

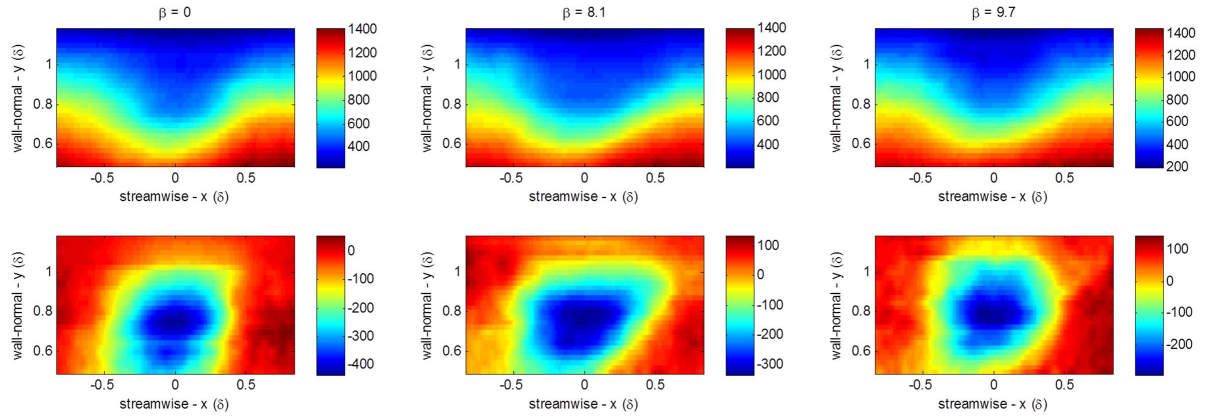

Figure E.5: Conditionally averaged features at y = 0.7δ with a diameter between 0.5δ and 0.75δ a) streamwise/wall-normal slice and b) streamwise/wall-normal slice with mean subtracted.

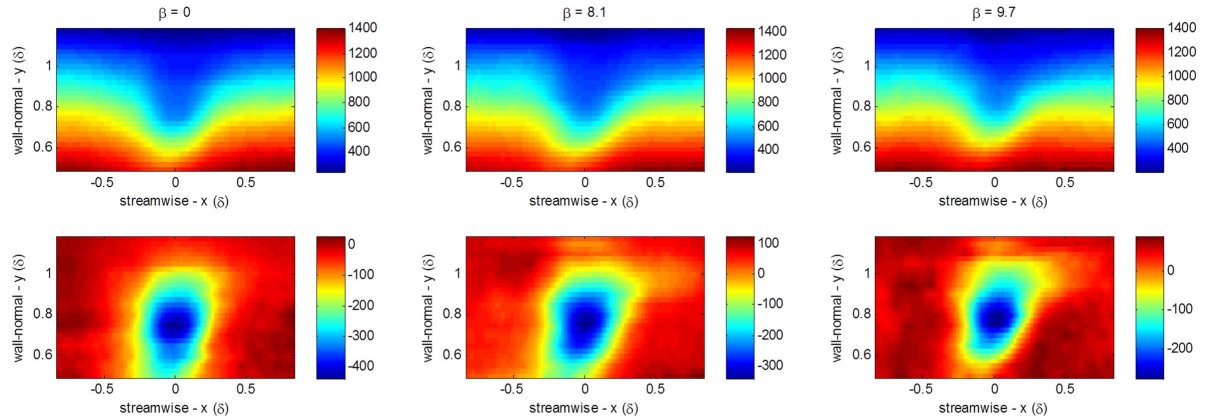

Figure E.6: Conditionally averaged features at y = 0.7δ with a diameter between 0.25δ and 0.25δ a) streamwise/wall-normal slice and b) streamwise/wall-normal slice with mean subtracted.